Indian J. pure appl. Phys., Vol. 18 No. 2 pp. 67-146
February 1980
CODEN : IJOPAU ISSN : 0019-5596
18 (2) 67-146 (1980)

23
7.4.80

INDIAN JOURNAL OF PURE & APPLIED PHYSICS

Published by
THE COUNCIL OF SCIENTIFIC & INDUSTRIAL RESEARCH, NEW DELHI
in association with
THE INDIAN NATIONAL SCIENCE ACADEMY, NEW DELHI

a quantum leap in recorder technology now available to the discriminating research scientist a range of reliable 'state of the art' recording instruments

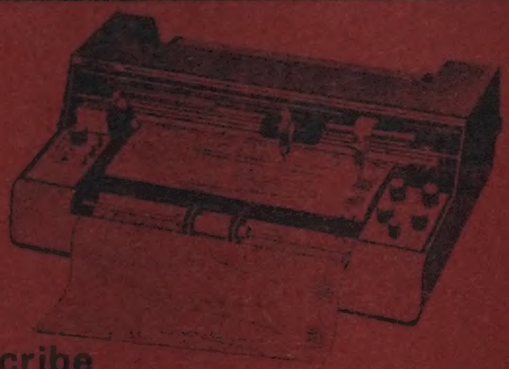

DigiScribe
Strip Chart Recorders One to Four Pens, 0.5 mV full scale and up, 0.5 sec response

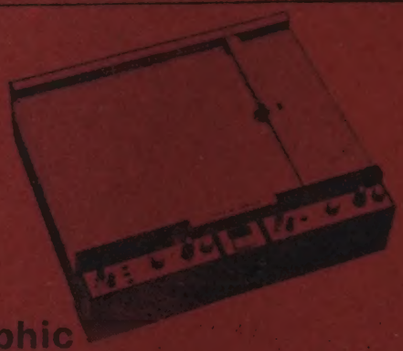

DigiGraphic
XY/t Recorders with plug-in modules to give wide ranges of sensitivity, time base facility and log recording.

HiScribe Oscillographic
Oscillographic Recorders DC to 80 Hz, One to eight channels, Heat or ink writing. Plug in modules to give wide range of sensitivities

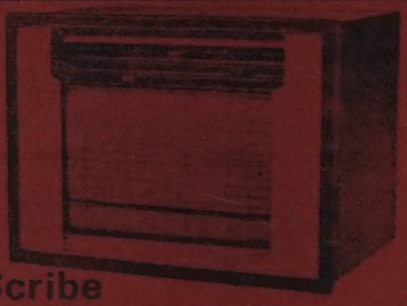

MultiScribe
One to Three Pen and 6, 12 and 24 point Recorders. Rack mounting with alarm contacts, cold junction compensation, and other features.

APPLICATIONS IN THE FIELDS OF

- METEOROLOGY • MATERIAL SCIENCES
- LIFE SCIENCES • PHYSICAL SCIENCES
- CHEMICAL AND ELECTROCHEMICAL SCIENCES
- BIOLOGICAL SCIENCES • PHYSIOLOGICAL AND BEHAVIOURAL SCIENCES • COMPUTER SCIENCES
- ENVIRONMENTAL AND POLLUTION STUDIES
- ENERGY STUDIES • PHARMACOLOGY
- MECHNICAL/ELECTRICAL ENEGINEERING
- METALLURY/METALLURGICAL ENGINEERING
- AERODYANAMICS/AERONAUTICAL ENGINEERING
- BIO-MEDICAL ENGINEERING
- QUALITY CONTROL APPLICATIONS

MANUFACTURED BY:

DIGITAL ELECTRONICS LIMITED

A Company in collaboration with

houston instrument | DIVN OF BAUSCH & LOMB

Office & Factory:

Digilog House, 74/11, C. Cross Road, Marol Industrial Area, MIDC, Andheri (East), Bombay-400 093. Phone: 577670. Gram: 'DIGILOG'

Indian Journal of Pure & Applied Physics

VOLUME 18 No. 2 FEBRUARY 1980

EDITORIAL BOARD

Dr B A Dasannacharya
Bhabha Atomic Research Centre
Bombay

Prof. B M Deb
Indian Institute of Technology
Bombay

Prof. P Krishna
Banaras Hindu University
Varanasi

Prof. Krishnaji
Allahabad University
Allahabad

Prof. K V Ramanathan
Tata Institute of Fundamental Research
Bombay

Dr S Chandrasekhar
Indian National Science Academy
New Delhi/Raman Research
Institute Bangalore

Prof. A K Saha
Saha Institute of Nuclear Physics
Calcutta

Prof. N C Sil
Indian Association for
Cultivation of Science
Calcutta

Prof. R Srinivasan
Indian Institute of Science
Bangalore

Prof. K Venkataramiah
Osmania University
Hyderabad

Dr K L Chopra
Indian National Science Academy
New Delhi/Indian Institute of
Technology New Delhi

Shri Y R Chadha, *Ex-officio* Secretary & Chief Editor

EDITORIAL STAFF

Editors
D S Sastry & K S Rangarajan

Assistant Editors
G N Sarma, J B Dhawan & Tarun Banerjee

Published by the Publications & Information Directorate, CSIR, Hillside Road, New Delhi 110 012

Chief Editor : Y R Chadha

The Indian Journal of Pure & Applied Physics is issued monthly. The Directorate assumes no responsibility for the statements and opinions advanced by contributors. The editorial staff in its work of examining papers received for publication is assisted, in an honorary capacity, by a large number of distinguished scientists, working in various parts of India.

Communications regarding contributions for publication in the journal should be addressed to the Editor, Indian Journal of Pure & Applied Physics, Publications & Information Directorate, Hillside Road, New Delhi 110 012.

Correspondence regarding subscriptions and advertisements should be addressed to the Sales & Distribution Officer, Publications & Information Directorate, New Delhi 110 012.

Annual Subscription
Rs. 100.00 £ 16.50 $ 42.00

Single Copy
Rs. 10.00 £ 1.80 $ 4.50

50% Discount is admissible to research workers and students and 25 % discount to non-research individuals, on annual subscription.

Payments in respect of subscriptions and advertisements may be sent by cheque, bank draft, money order or postal order marked payable *only* to **Publications & Information Directorate, New Delhi 110 012.**

Claims for missing numbers of the journal will be allowed only if received within 3 months of the date of issue of the journal plus the time normally required for postal delivery of the journal and the claim.

© 1980 The Council of Scientific & Industrial Research, New Delhi.

CSIR SCIENTIFIC PERIODICALS

JOURNAL OF SCIENTIFIC & INDUSTRIAL RESEARCH (monthly)

With a fine record of over 35 years' service to the scientific community, this Journal has grown into India's leading general science periodical. Intended to fulfil the responsibility of helping the research workers to keep themselves abreast of current developments in various fields of science and technology, the Journal carries editorial features highlighting important scientific events in India and abroad; articles on science policy and management of science; review articles on topics of current research interest; technical reports on international and national conferences; reviews of scientific and technical publications; and notes on major advances in various fields.

Annual subscription	**Rs 60.00**	**£ 10.00**	**$ 25.00**
Single copy	**6.00**	**1.00**	**2.50**

INDIAN JOURNAL OF CHEMISTRY (monthly)

This Journal which is running the 18th year of publication, was split up into two sections with effect from January 1976.

Section A: This section is devoted to papers in Inorganic, Physical, Theoretical and Analytical Chemistry.

Annual subscription	**Rs 70.00**	**£ 12.00**	**$ 30.00**
Single copy	**7.00**	**1.20**	**3.00**

Section B: This section is devoted to papers in Organic Chemistry including Medicinal Chemistry.

Annual subscription	**Rs 70.00**	**£ 12.00**	**$ 30.00**
Single copy	**7.00**	**1.20**	**3.00**

INDIAN JOURNAL OF PURE & APPLIED PHYSICS (monthly)

This Journal, which is running the 18th year of its publication, is devoted to original research communications (full papers and short communications) in all conventional branches of physics (except radio and space physics).

Annual subscription	**Rs 100.00**	**£ 16.50**	**$ 42.00**
Single copy	**10.00**	**1.80**	**4.50**

INDIAN JOURNAL OF RADIO & SPACE PHYSICS (bimonthly)

This Journal is intended to serve as a medium for the publication of the growing research output in various areas of radio and space physics.

Annual subscription	**Rs 60.00**	**£ 10.00**	**$ 25.00**
Single copy	**12.00**	**2.00**	**5.00**

INDIAN JOURNAL OF TECHNOLOGY (INCLUDING ENGINEERING) (monthly)

This Journal publishes papers reporting results of original research of applied nature pertaining to unit operations, heat and mass transfer, products, processes, instruments and appliances, etc. The Journal is of special interest to research workers in the departments of applied sciences in universities, institutes of higher technology, commodity research laboratories, industrial cooperative research institutes, and industrial research laboratories.

Annual subscription	**Rs 60.00**	**£ 10.00**	**$ 25.00**
Single copy	**6.00**	**1.00**	**2.50**

INDIAN JOURNAL OF EXPERIMENTAL BIOLOGY (monthly)

This Journal, devoted to the publication of research communications in the fields of experimental botany, zoology, microbiology, pharmacology, endocrinology, nutrition, etc., is the only one in India with such a wide coverage and scope.

Annual subscription	**Rs 120.00**	**£ 20.00**	**$ 50.00**
Single copy	**12.00**	**2.00**	**5.00**

INDIAN JOURNAL OF BIOCHEMISTRY & BIOPHYSICS (bimonthly)

This Journal, published in association with the Society of Biological Chemists (India), Bangalore, is the only research Journal in India devoted exclusively to original research communications in biochemistry and biophysics.

Annual subscription	**Rs 40.00**	**£ 7.00**	**$ 17.00**
Single copy	**8.00**	**1.40**	**3.50**

INDIAN JOURNAL OF MARINE SCIENCES (quarterly)

Commencing publication from June 1972, this Journal is devoted to research communications (full papers and short communications) pertaining to various facets of marine research, viz. biological, physical, geological and chemical oceanography.

Annual subscription	**Rs 40.00**	**£ 7.00**	**$ 17.00**
Single copy	**12.00**	**2.00**	**5.00**

RESEARCH & INDUSTRY (quarterly)

Intended to serve as a link between science and industry, this Journal is addressed primarily to technologists, engineers, executives and others in industry and trade. It publishes informative original articles containing practical details of processes and products developed in India, which show promise of ready utilization, and technical digests on new processes, products, instruments and testing methods which are of interest to industry. Developments in Indian industry are regularly reported.

Annual subscription	**Rs 24.00**	**£ 4.00**	**$ 10.00**
Single copy	**7.25**	**1.30**	**3.50**

INDIAN JOURNAL OF TEXTILE RESEARCH (quarterly)

Commencing publication from March 1976, this Journal is devoted to the publication of papers reporting results of fundamental and applied researches in the field of textiles.

Annual subscription	**Rs 36.00**	**£ 6.00**	**$ 15.00**
Single copy	**12.00**	**2.00**	**5.00**

Please contact

THE SALES & DISTRIBUTION OFFICER
PUBLICATIONS & INFORMATION DIRECTORATE, CSIR
HILLSIDE ROAD, NEW DELHI 110 012

Indian Journal of Pure & Applied Physics

VOLUME 18 No. 2 FEBRUARY 1980

CONTENTS

Solid State Physics

A Computer Study of the Composition of Some Amorphous Alloys: Metallic Glasses 67
RAHUL BASU

High Temperature Phase Transition in V_3O_5 71
N Y VASANTHACHARYA & S VASUDEVAN

Study of Blisters Formed due to Helium Ion Bombardment on Stainless Steel ... 74
B M PANDE, M S ANAND & R P AGARWALA

Origin of Growth Hillocks on the (001) Surface of Lead Molybdate Crystals ... 78
K SREEDHARAN PILLAI & M A ITTYACHEN

Effect of *p*H on the Liesegang Ring Formation of Lead Carbonate Crystals ... 81
K MOHANAN PILLAI, M A ITTYACHEN & V K VAIDYAN

Dependence of the *C-V* Index of a Hyperabrupt Junction on Junction Parameters ... 84
A K DATTA, K GHOSH, S B ROY, T B BISWAS & N K D CHOUDHURY

Chemical Physics

Measurements of Self-Diffusion Coefficients in Hg & Ga by a Radioactive Tracer Technique 87
A BASU, S N CHANGDAR & A M GHOSE

Averaged Potential for Complex Polar Fluids 91
OM SINGH & JAWAHAR LAL GAINDHAR

Force Field Studies of α, β-Unsaturated Amides I : N, N-Dimethyl Acrylamide ... 94
G RAMANA RAO & K VENKATA RAMIAH

Nuclear Physics

Effect of Etching Conditions on Track Registration Characteristics of Soda Lime Glass Detector 107
M M AHMAD, A KHAN & D S SRIVASTAVA

Dielectrics & Microwaves

Dielectric Relaxation Time & Dipole Moment of Some Substituted Anilines in Benzene Solutions 110
S M KHAMESHARA & M L SISODIA

Spectroscopy

Isotope Shift in Unclassified & Some New Lines of Neodymium Spectra in the Region 3930-6450 Å 114
S A AHMAD & G D SAKSENA

Electronics

Simulated Inductance Using Operational Amplifiers 121
R S SHARMA & N A SHAH

CONTENTS

COMMUNICATIONS

Low Angle X-Ray Diffraction Study of Liquid Crystal : Cholesteryl Methyl Carbonate 127
J Shashidhara Prasad & L Siddarame Gowda

NOTES

Lattice Vibration Modes in CdS 129
Hitoshi Kanamori, Masao Matsumoto, Kei Urabe & Nobuyuki Nakamori

Estimation of Sodium Content of Cotton for Use in Neutron Activation Dosimetry 130
P K Marathe, H K Kundu & G Venkataraman

Effect of High Pressures on the Hydrogen Bond Systems of Some Alcohols ... 132
A Srinivasa Rao

Molecular Constants of Acetylenes : Part II—Centrifugal Distortion Constants & Thermodynamic Functions of Silylacetylene 134
K Sabapathy, R Ramasamy & K Venkateswarlu

Dielectric Behaviour of Ferroelectric Ammonium Bisulphate Powders 135
K Sambasiva Rao & A Bhanumathi

Light Absorption & Photoemission of Ag-O-Cs Photocathode 138
R L Verma

Dielectric Transient Response of Some Biomolecules Following Ultraviolet Radiation 139
S B Supekar & T K Bandopadhyaya

Circuit Parameters for a Complex Helical SWS Combining Results for Simpler Configurations 141
A K Sinha & B N Basu

Laser Raman Spectrum of 3,4-Dichlorobromobenzene 143
S R Tripathi & G N R Tripathi

Automatic Trigger Pulse Logic for the Pulse Programmer for Use in Pulsed NMR ... 145
R K Shenoy, J Ramakrishna & R Srinivasan

Indian Journal of Pure & Applied Physics
Vol. 18, February 1980, pp. 67-70

A Computer Study of the Composition of Some Amorphous Alloys: Metallic Glasses

RAHUL BASU*
Department of Mechanical Engineering, Indian Institute of Science, Bangalore 560 012

Received 25 *February* 1978; *revised received* 20 *August* 1979

Metallic glasses have been of interest because of their mechanical properties. They are ductile as well as brittle. This is true of $Pd_{80}Si_{20}$, $Cu_{60}Zr_{40}$ and $Pd_{77\cdot5}Cu_6Si_{16\cdot5}$ alloys, all of which are amorphous. The most stable metallic glasses are those which are alloys of noble or transition metals. A general formula is postulated as $T_{70-80}G_{30-20}$ where T stands for one or several 3d transition metals and G includes the metalloids. A computer simulation is used to calculate the compositional limits over a range of temperatures. The addition of Si on the mechanical properties of $Cu_{60}Zr_{40}$ is also studied.

1. Introduction

In a previous publication,[1] the system Pd-Cu-Si has been simulated on the computer by the author for compositional analysis. This alloy has been the subject of study[2,3] since nearly the beginning of research effort in the field of amorphous alloys. The amorphous alloy is regarded by many as a 'super-cooled' liquid, the liquid structure being maintained by rapidly quenching the liquid alloy by a variety of methods.[2] Waseda *et al.*,[3] have studied the Pd-Si alloy system and analyzed the radial distribution function by X-ray methods, thus comparing the liquid and and amorphous (solid) phases. According to Duwez,[2] the position of the first maximum in the atomic distribution function r_1, can be considered as a measure of the average inter-atomic distance in the amorphous structure. The distance r_2 of the second maximum is related to the average distance of any atom from its second nearest neighbours. In most liquid alloys, this ratio of r_2/r_1 is nearly 1·85, and it is also valid for amorphous alloys. The radial distribution function is derivable from the diffraction pattern of the alloy by a Fourier transformation. The curves are easily connected in this way.

Another method is used to describe the structure of glassy alloys in terms of the coordination numbers and 'packing' of hard spheres, valid also for liquids. Other concepts include the Bernal packing and Voronoi polyhedra. Since the metalloid atoms, P, C, B and Si have different volumes and sizes, and so also the noble metal atoms, the combination of metalloid and noble or transition elements can often form the glassy phases. Hence, the dense random packing of hard spheres, (DRPHS) which can be done on the computer, gives another estimate for the parameters r_1 and r_2, as also r_2/r_1.

In the present analysis, the thermodynamic approach has been used. Although this theory of amorphous alloys is in a rather underdeveloped state in terms of the quantitative concepts, this method has been applied on the computer since it yields the best quantitative results as compared to the others which to date have not yielded any valid estimates.

2. Analysis

In order to provide the input to the computer in the Kaufman approach,[4] the interaction parameters (Tables 1 and 2) in terms of the Van Laars numbers are calculated. These are a set of fundamental parameters at the atomic and molecular level that describe the interactions between the atoms (and molecules). The method of Kaufman involves the minimization of the free-energies of two or more phases to obtain the equilibrium by a common tangent construction. The interaction parameters for the liquid and amorphous phases are taken to be the same since they are very similar in structure.[3] The interaction parameters for the secondary phases such as bcc, fcc or hcp are taken to be the same as the bcc phase, since the subsequent parameters are obtained by addition of negligible quantities to it. The numbers e_0, e_p and e_1 are calculated for the alloys of interest in this study from the following expressions given in the book by Kaufman[4]:

$$e_0 = -23050 \times 5 \times (x_i - x_j)^2$$

$$e_1 = 0{\cdot}5\,(H_1+H_2)\,(V_1-V_2)^2/(V_1+V_2)^2$$

$$e_p = 0{\cdot}3\,\{(H/V)_1^{1/2}-(H/V)_2^{1/2}\}\,(V_1-V_2)$$

*Present Address : Gas Turbine Research Establishment, P O B 1777, Bangalore 560 075.

where the quantities H and V are the enthalpies of vapourization and specific volumes of the components respectively; x_i is the electronegativity (Pauling's) given in the atomic tables for component i. The data are given in Tables 1 and 2.

It is instructive to mention here that the free-energy for the compound phase in the regular solution approximation is $G = H + TS = \phi\, x(1-x) - RT\{x \ln x + (1-x) \ln (1-x)\}$ = excess free-energy + configurational free-energy

For equilibrium :

$$(dG/dx)_1 = (dG/dx)_2 = \text{chemical potential}$$

This is true even if the two phases (1) and (2) have different structures or G is not completely continuous, provided G is continuous at the point of differentiation.

Here,

$$dG/dx = \phi\,(1-2x) + RT\{\ln (1-1/x)\},$$

which depends only on the structure and the undercooling, in the case of a liquid cooled to a temperature T below the melting point T_m; in amorphous or liquid form. Hence the quenching and formation of amorphous phase can be regarded as solidification with undercooling. The transformation from amorphous to crystalline is clearly defined with a definite enthalpy of crystallization associated with it. Values exist in the literature for Pd-Si (Ref. 5) and for Cu-Zr (Ref. 6) systems. Chen[5] gives a value of 1130 cal for $Pd_{80}Si_{20}$, and Grant *et al.*[6] gave 1260 cal for systems $Cu_{60}Zr_{40}$ in the same transformation.

2.1 Thermodynamic Analysis

The method used is the LCRSE of Kaufman,[4] to describe the quasi-static equilibrium between the amorphous and crystalline phases. Assuming L and B are known, then the LCRSE is derivable from the following set of equations:

For compound ψ

$$F^{\psi} = (1-x_*)\, F_i^{\theta} + x_* F_j^{\theta} + x_*(1-x)\,(L-C) \qquad ...(1)$$

For liquid fraction i

$$F_i^L = F_i^L + RT \ln (1-x) + x^2 L \qquad ...(2)$$

For liquid fraction j

$$F_j^L = F_j^L + RT \ln x + (1-x^2)\, L \qquad ...(3)$$

Multiplication of Eq. (2) by $(1-x_*)$ and Eq. (3) by x_* and adding and using the equation $\Delta F = \Delta H - T\Delta S$ gives the LCRSE :

$$T(x) = [(C-L)x_*(1-x_*) + \Delta H_1 (1-x_*) + \Delta H_2 x_* + \phi\{x_*(1-2x) + x^2\}]/[\Delta S_1 (1-x_*) + \Delta S_2 (1-x_*) - R\{(1-x_*) \ln (1-x) + x_* \ln x\}]$$

Table 1—Values of Enthalpies of Vaporization and Specific Volumes and Electronegativity of Different Elements

	H, cal/g-atom	V, cc	X
Pd	90000	8·86	2·2
Cu	81800	7·09	1·9
Si	40600	12·05	1·8
Zr	120000	14·04	1·4

Table 2 - Values of Liquid Phase Parameter and bcc Phase Parameter for Different Alloys

	e_0	e_p	e_1	L	B, cal/g-atom
Pd-Si	−18448	11600	1520	− 6989	− 5469
Pd-Cu	−10377	172	880	−10205	− 9328
Cu-Si	− 1153	13800	3820	12647	16467
Cu-Zr	- 28825	1305	10794	−27520	−16726

Note: The liquid phase parameter $L = e_0 + e_p$, and bcc phase parameter $B = L + e_1 + e_2$ where e_2 is neglected in this analysis.

where x_* = the fraction of component i in the binary compound, C = a constant varying between 0 and 18000 cal/g-atom, depending on the stability of the ψ phase. Variation of T with x is reported in Table 3.

According to Chen,[7] the values of T_g for $Pd_{83}Si_{17}$ ~ 632 K, and for $Pd_{80}Si_{20}$ ~ 653 K. These compare well with the computer simulation (Table 3). Further tabulations obtained for Pd-Si are given in Ref. 1. In all these calculations, the enthalpy and entropy changes were assumed to occur at the melting point by splat cooling or other means. A correction was made for the heat transfer losses and undercooling, which according to Chen[7] assume the following typical values for amorphous alloy formation:

$$\Delta S_m \sim R, \quad x_* \sim 0{\cdot}2, \quad \Delta T \text{ (undercooling)} \sim 0{\cdot}2 T_m + (0{\cdot}2 \text{ to } 0{\cdot}4)\, T_m$$

In the Pd-Si system, the values $\Delta H = 11\,0$ for Pd and $\Delta H = 5550$ for Si together with the corresponding entropy changes give good simulation using LCRSE, which is probably a good theoretical approximation to the processes occurring in such alloy solidification.

However, in the $Cu_{60}Zr_{40}$ simulation, the values used were the actual latent heats of the component elements, and were found to give a good simulation. This difference might be due to some heat transfer properties, as also the fact that ΔS for the components is nearly equal to R (2 cal/K/g-atom). Hence it might appear feasible that such values could be used without any modification for undercooling or heat transfer (which would be negligible in the short

Table 3—Variation of T with Concentration for Pd-Si Systems [$L = -5469$, $\phi = -6989$ and $C = 4500$]

x	T
0·0399	601
0·0797	657
0·1196	690
0·1594	707
0·1993	713

Values of ΔH and ΔS are 1130 and 2·30 for Pd; and 5550 and 3·30 for Si (all in cal/g-atom)

time and extremely high quenching rates used for such alloy formation). The values used here have been taken from Ref. 9, and are:

	ΔH, cal/g-atom	ΔS, cal/K/g-atom
Cu	3120	2·30
Zr	4900	2·30

These values were used in both LCRSE and TRSE programs listed by Kaufman.[4] The TRSE routine constructs the common tangent to the liquid phase and bcc phase free-energy curves to obtain the $T-x$ equilibrium for bcc-liquid (amorphous) (Table 4). Hence it gives the equilibrium between the amorphous and crystalline phases (taken as bcc in this approximate method). The interaction parameters used were:

e_0	e_p	e_1	L	B, cal/g-atom
−28825	1305	10794	−27520	−16726

In both these simulations, i.e. LCRSE and TRSE, the transformation temperature of 450°C or 723 K is included, where the Cu-Zr amorphous alloy transforms to crystalline phase.[6] The TRSE indicates that the glassy-crystalline equilibrium is feasible at this temperature for $Cu_{15}Zr_{85}$ and also $Cu_{71}Zr_{29}$, i.e. the stoichiometry of Cu varies from 0·15 to 0·71. However, according to the LCRSE listing, the stoichiometry at $T = 723$K is approximately 0·26 at one end and 0·55 at the other end of the range of of variation with T. Thus the LCRSE formula is $Cu_{26}Zr_{74}$ to $Cu_{55}Zr_{45}$. These are contained in the TRSE values and clearly consistent. Also, from Table 4 we find that for $x = 0{\cdot}40$, $T = 935$ K as compared to experimental value which is 723 K. This is quite a good comparison.

Table 4—Values of T and x Used in LCRSE and TRSE in the Cu_{60} Zr_{40} Simulation

x	LCRSE	T, K
0·1187		295
0·1539		435
0·1891		562
0·2242		673
0·2594		766
0·2945		839
0·3297		892
0·3649		924
0·4000		935
0·4352		925
0·5406		769
	TRSE	
x_1	x_2	T, K
0·1419	0·7200	545
0·1432	0·7181	580
0·1444	0·7160	615
0·1456	0·7139	650
0·1475	0·7096	720
0·1484	0·7073	755
0·1491	0·7049	790
0·1496	0·7024	825
0·1500	0·6998	860

3. Mechanical Properties

Duwez[2] has remarked on the very outstanding and promising mechanical properties of such amorphous alloys, and their potential uses as composite materials and electronic materials are mentioned by many. A general formula for these alloys may be written as $T_{70-80}G_{30-20}$ where T stands for one or more 3d transition or noble metals and G includes the glass forming metalloids. B, C, Si and P are G elements, and Cr, Mn, Fe, Co and Ni are T elements. Turnbull,[11] has also stated a formula A_3B to A_5B, where A is a noble metal or transition metal and B is a metalloid. According to him, the heats of formation of these alloys from their pure metallic liquid state have rather large negative values. Most of them exhibit rather deep eutectics at compositions near A_4B. This corresponds to $Pd_{80}Si_{20}$. Eutectics are good for *in situ* composite fabrication using controlled solidification. The very low eutectic temperature of such alloys brings them much closer to the region of glass formation while still in liquid state. The same applies to Cu-Zr.

It is instructive to examine the properties of the ternary alloys formed by the addition of Si to Cu-Zr. According to Sprenger *et al.*,[10] it is an unknown system.

The ternary diagram is illustrated[10] for 800°C. At room temperature, the ultimate tensile strength (UTS fracture stress) is 38 kg/mm^2, or about 54,000 psi. The system Cu/CuZrSi was found to

have a rod-like morphology and can be used as a reinforced material, or as an *in situ* composite. The determination of the unknown system ZrCuSi revealed that pseudobinary sections exist between copper and the E phase of ZrCuSi. The pseudobinary section (E phase) Cu-ZrCuSi has a eutectic temperature of 1045°C, and 9·5 volume per cent of E phase in the Cu matrix. The solubility of Zr and Si in the Cu matrix is extremely low (< 0·01% for Zr and 0·1% for Si). The strength at 500°C is 24,300 psi. The value of 54000 psi for UTS at room temperature is an increase over that of pure Cu by more than 200%.

This might be compared with the Pd-Si/PdCuSi system. Duwez[2] mentions some properties of the $Pd_{80}Si_{20}$ alloy. It is brittle below a temperature (glass) of 653 K with a total strain at rupture of less than 0·5%, and a fracture stress of 136·4 kg/mm². The stress varies with strain up to a stress of 87·3 kg/mm², the value of E being $6{\cdot}8 \times 10^3$ kg/mm². The addition of Cu to the PdSi alloy to form $Pd_{77.5}Cu_6Si_{16.5}$ raises the mechanical strength by a disproportionate amount. For the ternary alloy, the stress is linear with strain up to 1·8% strain and the stress limit is 150 kg/mm². The increase is at least 150% if not 200%.

It is interesting to compare the two ternary alloys. For Pd-Cu-Si, a small amount of Cu of 6 % has produced a marked increase in the elastic properties and stress limit. In the Cu-Zr combination also marked increase in mechanical properties occurs with negligible amounts of Si and Zr added to Cu. The effect is the same, and is an interesting topic for further research, as the usual theory of composite modulus, etc. cannot explain such marked increases in the ternary alloys. The concepts of solution hardening and dislocation precipitate interaction might prove a better answer. However, the Burgers vector is difficult to define in the amorphous phase.

4. Conclusion

It appears from this preliminary study that the thermodynamic approach can give suitable quantitative answers to the formation of amorphous and two-phase materials based on these. The notions of Chen[5,7,8] are a good starting point for such analysis using programs such as TRSE and LCRSE.[4] The increase in strengths of PdCuSi and CuZrSi over the matrix of Cu have potential for advanced high temperature composite fabrication. It is probable that other such alloys can be engineered and designed. With the potential application to ribbons and wires with strength over 300,000 psi, it is likely that research could probably expand rapidly in this direction in the future.

Nomenclature

x	= concentration
x_*	= the fraction of component i in the binary compound
H	= enthalpy of vaporization
S	= entropy of vaporization
e_0, e_p, e_1	Van Laar parameters
L, B	interaction parameters for liquid and bcc phases
F^L	= free-energy of liquid phase
F^ψ	= free-energy of phase ψ
T_m	= melting point
ΔS_m	= entropy of melting
R	= universal gas constant=1·987 cal/g-atom
ϕ	= interaction parameter for phase ϕ (=B)
ΔF	= free-energy change
ΔH	= enthalpy change
ΔS	= entropy change
TRSE	= Two Regular Solution Equilibrium (Computer program)
LCRSE	= Line Compound Regular Solution Equilibrium (Computer program)

References

1. Basu R, *Computer coupling of phase diagrams and thermochemistry* (Pergamon Press, London), **2** (1978), 285.
2. Duwez P, *Annual review of materials science*, **V6** (No. 8583) (1976), 83.
3. Waseda Y & Masumoto T, *Phys. Status Solidi*, (*a*), **31** (1975), 477.
4. Kaufman L & Bernstein H, *Computer calculations of phase diagrams* (Academic Press, New York), 1970.
5. Chen H S & Turnbull D, *Acta Met.*, **17** (1969), 1021.
6. Vitek G M, Van der Sande J B & Grant N J, *Acta Met.*, **23** (1975), 165.
7. Chen H S, *Acta Met.*, **22** (1974), 1504.
8. Chen H S, *Acta Met.*, **22** (1974), 897.
9. Hultgren R *et al.*, *Selected values of the thermodynamic properties of metals and alloys* (John Wiley, New York), 1973.
10. Sprenger H & Nickl J J, *Proc. Conference on in situ Composites*, Lakeville Conn., (National Academy of Sciences, Washington D C), 1973.
11. Turnbull D, *Acta Met.*, **19** (1971), 1295.

Indian Journal of Pure & Applied Physics
Vol. 18, February 1980, pp. 71-73

High Temperature Phase Transition in V_3O_5*

N Y Vasanthacharya & S Vasudevan
Solid State & Structural Chemistry Unit, Indian Institute of Science, Bangalore 560 012

Received 9 *November* 1978; *revised received* 16 *January* 1979

V_3O_5 shows a single first-order phase transition (in the 80-500 K range) around 425 K accompanied by a small change in unit cell dimensions and an order of magnitude change in electrical resistivity. Magnetic susceptibility shows a break at the transition temperature, but the material remains paramagnetic in the range 80-500 K. PES shows minor changes in the valence band through the transition.

1. Introduction

V_3O_5 has been investigated repeatedly by different groups of workers in order to find out whether it undergoes any phase transition. The interest arises from the fact that other vanadium oxides belonging to the V_nO_{2n-1} homologous series exhibit interesting electrical and magnetic transitions.[1,2] Kosuge *et al.*[3] reported a magnetic transition around 235 K, but the same group of workers[4-6] did not find any anomaly in the electrical resistivity. Magnetic ordering or transition temperatures have been reported to be at 69 K by Kachi *et al.*,[7] at 130 K by Kosuge,[8] Nagasawa *et al.*[9] and Nagasawa[10] and at 430 K by Bruckner *et al.*[11] It is interesting that three magnetic ordering transition temperatures are reported by the same group of workers. While some of these workers reported no electrical resistivity anomalies in the range 120-300 K, electrical transitions have been reported at 175 K by Tekai and Koide[12] and in 420-433 K range by Bruckner *et al.*,[11] Terukov and Chudnovski[13] as well as Khoi *et al.*[14] Kosuge[8] reported no transition in the range 120-1070 K from DTA studies while Khoi *et al.*[14] found a DTA transition around 430 K. Khoi *et al.* also reported X-ray data for the two phases and observed only a small change in cell volume with no change in crystal symmetry. Similar observations have been made by Bruckner *et al.*[15] as well as Karmenko *et al.*[16] During the last year, Keer and Honig[17] have reported the 430 K transition by DSC measurements while Terukov *et al.*[18,19] have reported electrical and other properties through this high temperature transition. It now appears as though the transition around 69 K is a definite one, the transition being associated with anti-ferromagnetic ordering as evidenced from spin-flip inelastic neutron scattering,[20] Mössbauer[7] and NMR[21] studies. The question then arises about the transition reported between 70 K and 430 K as well as the one at 430 K. Hence we considered it worthwhile to investigate V_3O_5 from 80 K to 500 K for possible phase transitions.

2. Experimental Details

V_3O_5 was prepared by the arc method[22] starting from V_2O_3 and VO_2 or vanadium metal and V_2O_5 all of 99·99% purity. Differential scanning calorimetry (DSC) was carried out employing Perkin-Elmer DSC-II, employing a scanning rate of 20 deg min^{-1} and indium standard. X-ray diffraction data were obtained by using a GE X-ray diffractometer fitted with a high temperature attachment. Magnetic susceptibility was measured by the Gouy method employing a locally fabricated apparatus. Four-probe electrical resistivity measurements were also carried out employing a locally fabricated apparatus. X-ray photoelectron spectra (XPES) of V_3O_5 were recorded as a function of temperature employing an ESCA III Mark 2 spectrometer of VG Scientific Ltd, UK. Al$K\alpha$ (1486·6 eV) radiation was used.

3. Results and Discussion

V_3O_5 has a monoclinic structure at room temperature with cell parameters a = 9·86 Å, b = 5·05 Å, c = 7·01 Å and β = 109·5°. The room temperature phase extends from 80 K upto 425 K. At 425 K, DSC shows (Fig. 1) a first-order phase transition with a ΔH value of 346 cal/mole. This ΔH value is between the two recent literature values.[17,19] Thermal hysteresis in the transition is negligible. The crystal structure of V_3O_5 after the transition at 425 K remains the same and the lattice parameters are only slightly different (a = 9·84 Å, b = 5·04 Å, c = 7·02 Å, β = 109·2°). The volume decrease in the transition is hardly about 0·3%. Our

* Communication No. 28 from the Solid State & Structural Chemistry Unit

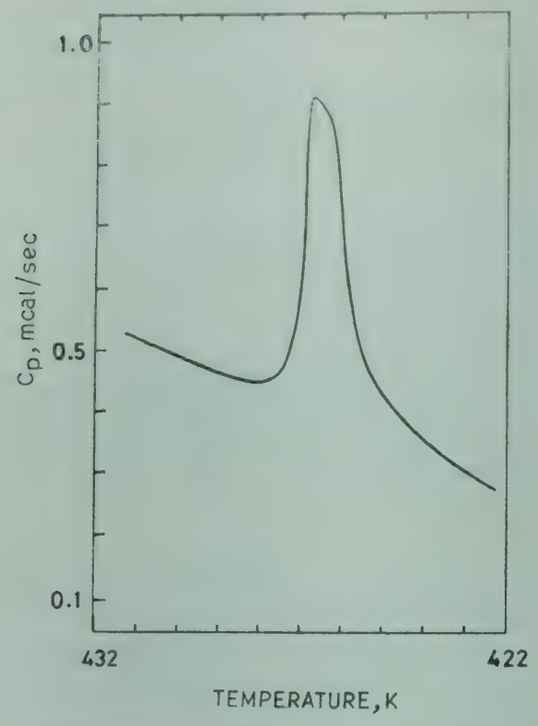

Fig. 1—Differential scanning calorimetric curve of V_3O_5

X-ray and DSC data clearly establish that in the temperature range 80-500 K there is only one phase transition (at 425 K) in V_3O_5.

Magnetic susceptibility data of V_3O_5 are shown in Fig. 2. At the 425 K transition, the inverse magnetic susceptibility shows a sharp break. The material remains paramagnetic through the transition and the effective moment per vanadium atom also roughly remains the same, the actual values being 2·6 μ_B and 2·5 μ_B before and after the transition; the Curie constants before and after the transition are 0·82 and 0·79 respectively. It is interesting that both these moments are close to the localized moment value. The inverse magnetic susceptibility of V_3O_5 also shows a smooth change in slope around 220 K, the observed change being much higher than the experimental uncertainty. This cannot be due to the presence of V_4O_7 as impurity. V_4O_7 undergoes an anti-ferromagnetic-paramagnetic transition around 250 K around which temperature the inverse susceptibility shows a sharp decrease. From Fig. 2 we can see an increase in the inverse susceptibility in this temperature range.

Electrical resistivity data of V_3O_5 are shown in Fig. 3. The resistivity shows a sharp drop at 425 K with an order of magnitude jump in resistivity, in agreement with the results of Terukov *et al.*[18] The material remains a semiconductor before and after this transition. The activation energies for conduction before and after the transition are 0·16 and 0·15 eV respectively. Resistivity data also show a gradual change of slope in the 200-300 K range, in which range we noticed a smooth change in the slope of the inverse magnetic susceptibility-temperature plot (Fig. 2). An examination of the recent resistivity data[18] seems to indicate a similar behaviour in this temperature region although magnetic susceptibility data of the same workers were not available to us in the temperature region below 300 K.

XPES of V_3O_5 were recorded between 80 K and 500 K. No significant changes either in the valence band or the core level spectra were observed between 80 K and 300 K. Above 425 K, however, the valence band shifts slightly to lower binding energy side and becomes more intense (Fig. 4). Such

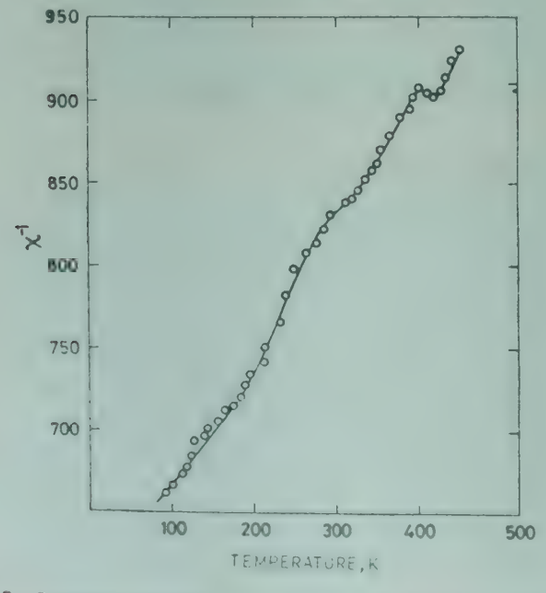

Fig. 2—Inverse magnetic susceptibility of V_3O_5 as a function of temperature

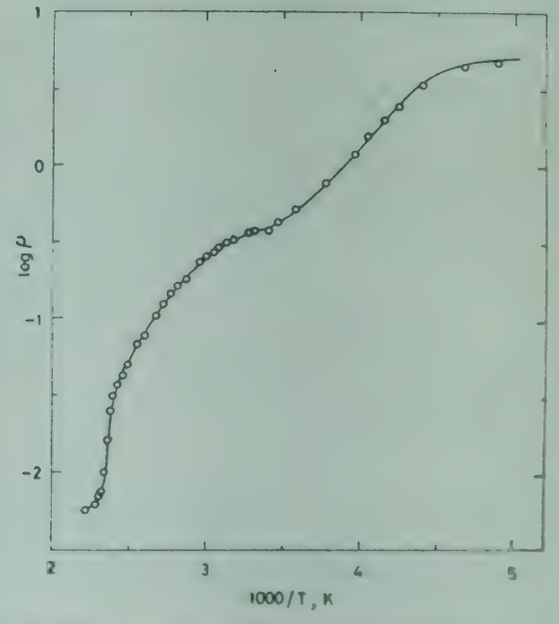

Fig. 3—Plot of logarithm of electrical resistivity against reciprocal of absolute temperature

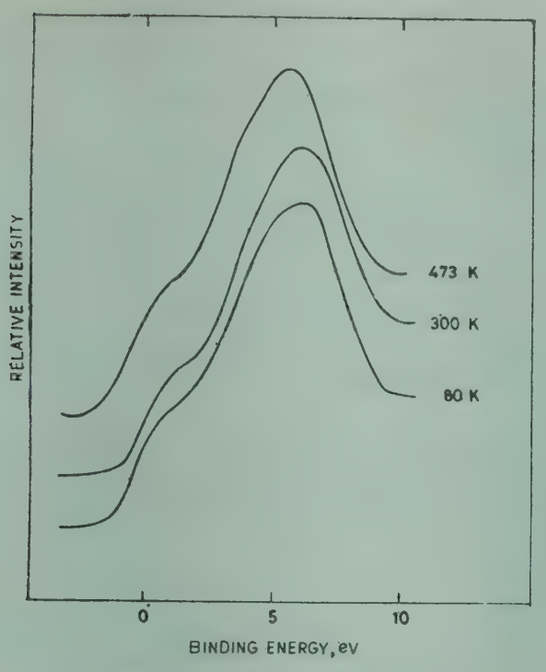

Fig 4—XPES valence band spectra of V_3O_5 above and below the transition temperature [The V (3 *d*) band is around 1·5 eV; the main band around 6·5 eV is due to O (2 *p*)]

changes in the valence band have been observed in the semiconductor-metal transitions of other metal oxides.[23] There is also a shift (~ 0·3 eV) to lower binding energies of the V (3 *s*) and V (3 *p*) bands above 423 K as compared to the spectrum at 300 K. The changes observed in the PES are consistent with the observed lowering of resistivity of V_3O_5 after the 425 K transition.

The present studies suggest that the resistivity jump found in V_3O_5 at 425 K is not due to a change in crystal symmetry or magnetic ordering. The volume change in the transition is smaller than in the transition of Ti_2O_3 where again there is no change in symmetry or magnetic behaviour.[2,24] A likely cause of the large ΔS of the transition at 425 K is that the increase in electronic disorder is related to the presence of two valence states of the metal ion. The slight decrease in the magnetic moment after the 425 K transition is consistent with the delocalization of *d*-electrons, but the persistence of the near-localized moment value in both the phases suggests that the transition may be of Mott-Hubbard type.

Acknowledgement

The authors thank Prof. CNR Rao for suggesting the problem and guidance, and the Department of Science and Technology, Government of India, New Delhi, for financial support of this research.

References

1. Mott N F, *Metal-insulator transitions*, (Taylor-Francis, London), 1974.
2. Rao C N R & Subba Rao G V, *Transition metal Oxides : crystal chemistry, phase transitions and related aspects*, NSRDS-NBS Monograph 49, (National bureau of standards, Washington, DC) 1974.
3. Kosuge K, Takada T & Kachi S, *J. phys. Soc. Japan*, **18** (1963), 318.
4. Kachi S, Takada T & Kosuge K, *J. phys. Soc. Japan*, **18** (1963), 1839.
5. Okinaka H, Nagasawa K, Kosuge K, Bando Y, Takada T & Kachi S, *J. phys. Soc. Japan*, **27** (1969), 1366.
6. Nagasawa K, Bando Y & Takada T, *J. crystal Growth*, **17** (1972), 143.
7. Kachi S, Kosuge K & Okinaka H, *J. Solid St. Chem.*, **6** (1973), 258.
8. Kosuge K, *J. Phys. Chem. Solids*, **28** (1967), 1613.
9. Nagasawa K, Bando Y & Takada T, *Japan J. Appl. Phys.*, **8** (1969), 1267.
10. Nagasawa K, *Mater Res. Bull.*, **6** (1971), 853.
11. Bruckner V, Wich G, Terukov E I & Chudnovskii F A, *Soviet Phys. Solid St.*, **17** (1976), 1452.
12. Takei H & Koide S, *J. phys. Soc. Japan*, **21** (1966), 1010.
13. Terukov E I & Chudnovskii F A, *Fiz. Tekh. Poluprov*, **8** (1974), 1226.
14. Khoi N N, Simon T R & Eastwood H K, *Mater Res. Bull.*, **11** (1976), 873.
15. Bruckner W, Moldenhauer W, Thuss B & Forsterling G, *Phys. Status Solidi*, **A35** (1976), K49.
16. Karmenko N F, Terukov E I & Chudnovskii F A, *Soviet Phys . Solid St.*, **18** (1976), 1874.
17. Keer H V & Honig J M, *Mater Res. Bull.*, **12** (1977), 277.
18. Terukov E I, Khomskii D I & Chudnovskii F A, *Dokl. Akad Nauk SSR, Exp. theor. Phys.*, **73** (1977), 2217.
19. Terukov E I, Khomskii D I & Chudnovskii F A, *Solid St. Commun.*, **25** (1978), 573.
20. Heidemann A, *Phys. Status Solidi*, **A16** (1973), K 129.
21. Gossard A C, Di Salvo F J, Erich L C, Kemeika J P, Yasuoka H, Kosuge K & Kachi S, *Phys. Rev.*, **B10** (1974), 4178.
22. Loehman R E, Rao C N R & Honig J M, *J. scient. ind. Res.*, **28** (1969), 13.
23. Vasudevan S, Hegde M S & Rao C N R, *Solid St. Commun.*, **27** (1978), 131.
24. Shaikh A M, Vishwamitra M A & Rao C N R, *Curr. Sci.*, **56** (1977), 431.

Indian Journal of Pure & Applied Physics
Vol. 18, February 1980, pp. 74-77

Study of Blisters Formed due to Helium Ion Bombardment on Stainless Steel

B M Pande, M S Anand & R P Agarwala

Chemistry Division, Bhabha Atomic Research Centre, Bombay 400 085

Received 16 *July* 1979; *revised received* 3 *October* 1979

Sheets of stainless steel were bombarded by helium ions using 2MeV $^4He^+$ ion beam in a van-de-Graaff machine. Dose of irradiation varied between $1{\cdot}0\times10^{18}$ and $5{\cdot}6\times10^{18}$ ions/cm^2. Helium gas blisters and exfoliations thus formed were examined by a scanning electron microscope. The results of annealing studies on these blisters and exfoliations are reported.

1. Introduction

The study of the behaviour of material surfaces under ion bombardment[1-3] has lately come into prominence due to its potential application in the future fusion reactors. During the operation of a fusion reactor, the surfaces of the first wall material and other components will be exposed to ions of different energies[4] (ranges, 1-10 keV and a few MeV). Due to the bombardment by helium ions, the surfaces of the materials get damaged giving rise to phenomena like blistering, erosion, etc. The gas ions get implanted near the surface region of the material and form blisters on the surface. When these blisters on the surface grow to bigger sizes, the pressure inside them becomes more than critical[3] and blisters exfoliate. The peeling of the blister skin will cause erosion thereby damaging the material. The blisters formed on 304-stainless steel after helium ion bombardment are reported and discussed in this paper.

2. Experimental Procedure

304-Stainless steel specimens (1 × 1 cm^2) were prepared from a commercial grade steel sheet of 0·6 mm thickness. The specimens were sealed in a quartz tube to a vacuum of $\sim 10^{-5}$ torr and were annealed in the pre-calibrated electrical furnace at 1373 K for $1{\cdot}08 \times 10^4$ sec. Later on, the specimens were mechanically polished using upto 600 grade carborundum papers and then electro-polished using perchloric acid (10 cc) and acetic anhydride (20 cc).

A specimen was then mounted on a special stage cooled by chilled water during irradiation and was fitted on a port hole of a van-de-Graaff machine. The specimens were irradiated by helium ions to different doses at normal incidence of the beam. The energy of helium ions was 2 MeV having a current of 4 μ A. The irradiation of different specimens was carried out to different doses ranging from 1×10^{18} to $5{\cdot}6 \times 10^{18}$ ions/cm^2. The irradiated samples were examined in a scanning electron microscope (SEM). The irradiated specimens were further annealed at 723 and 1273 K under vacuum ($\sim 10^{-5}$ torr) for $7{\cdot}2 \times 10^3$ sec and examined in SEM.

3. Results and Discussion

The formation of blisters and exfoliations depends on a number of factors[5-7]: Energy of gaseous ions; diffusivity of these ions; their solubility in the matrix; yield strength of the material; temperature of the target; dose rate, total dose, etc. In the present study, only the effect of total dose, at normal incidence for helium ions for a fixed energy of 2 MeV was undertaken.

Several stages of surface structures were seen due to blistering and exfoliation depending upon the bombardment dose (Figs. 1, 2 and 3). It was seen that as the dose increased, blisters started exfoliating as seen in Fig. 3, till a clear exfoliated area was formed on the surface. It was interesting to know that in the present case, the dose for blistering was already above critical dose. Behrisch *et al.*[4] have shown that the critical dose depends on energy and for 2 MeV, it is 1×10^{18} ions/cm^2. As such, it is expected that even at the lowest irradiation dose, blisters should be observed, which is the case in the present experiment. In Fig. 2, blisters along with a small exfoliated area, could be seen and they have arisen due to non-alignment of the beam in certain areas further resulting in a lower dose at that point. The exfoliated area observed in Fig. 2, has been further enlarged (Fig. 3) to clearly show the start of the rupture at the periphery and not at the centre. On increasing the dose of irradiation further to

Fig. 1—Blisters (× 40) after bombardment by a dose, of 1 × 10^{18} ions/cm^2

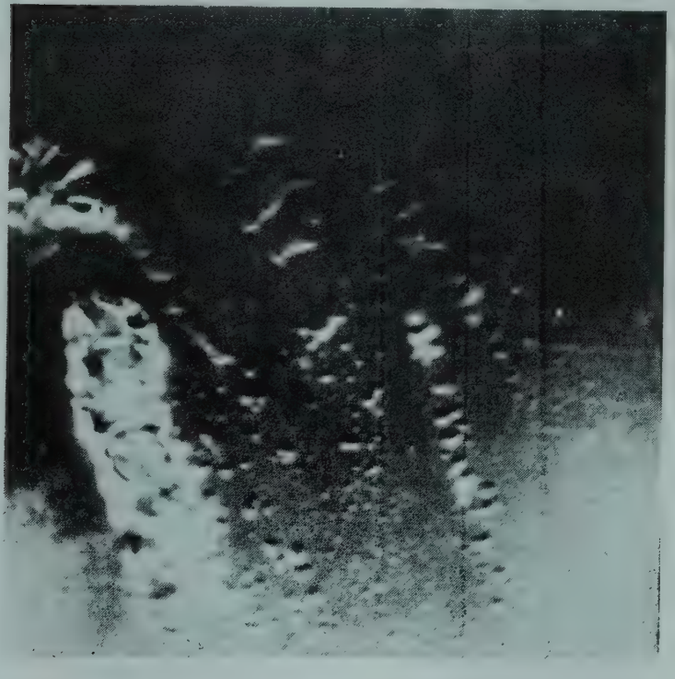

Fig. 2—Blisters (× 40) along with exfoliated area (Dose, 2 × 10^{18} ions/cm^2)

Fig. 3—Exfoliated area (× 200) (Dose, 2 × 10^{18} ions/cm^2)

Fig. 4—Exfoliated area (× 200) (Dose, 5 × 10^{18} ions/cm^2)

5·6 × 10^{18} ions/cm^2, the blisters disappeared and large exfoliation appeared on the surface (Fig. 4). The exfoliated area had ruptured skin on the periphery and there was another rupture at the middle of exfoliation. This was due to an increased dose impinging on it. In Fig. 4, small blister-like areas (point A in Fig. 4) could also be seen. These may be due to the ruptured metal pieces. On examining the exfoliated area at higher magnification, some spherical structures were observed (Fig. 5). This was unlike the spongy surface reported by Behrisch *et al.*,[1] at high doses (6 × 10^{20} ions/cm^2) in niobium. In the present study, the dose of irradiation was much below the dose used by earlier workers. Kaminsky and Das[3] showed recently that even at much higher doses above the critical value for blistering, blisters and exfoliations continued to exist together. The observation of spongy surface in niobium[4] was suspected by them to be arising due to the rise in target temperature. However, Bauer

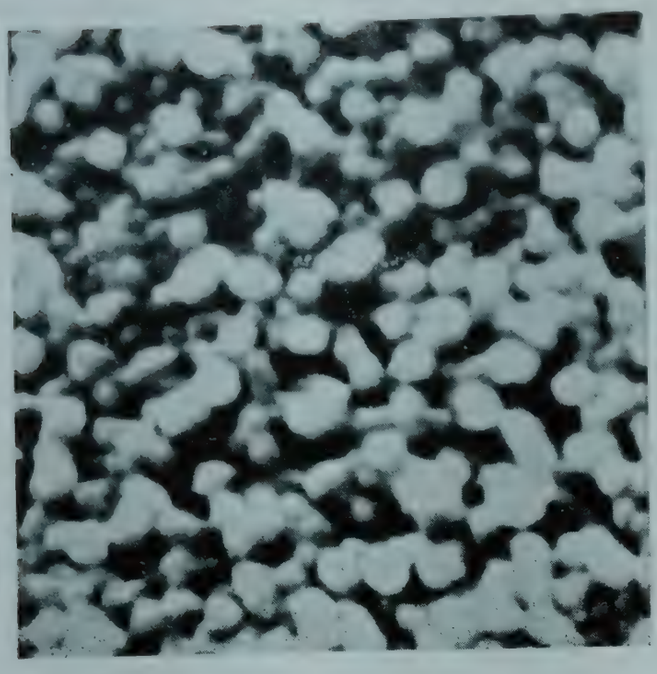

Fig. 5—Inside of exfoliated area at higher magnification (× 8000)

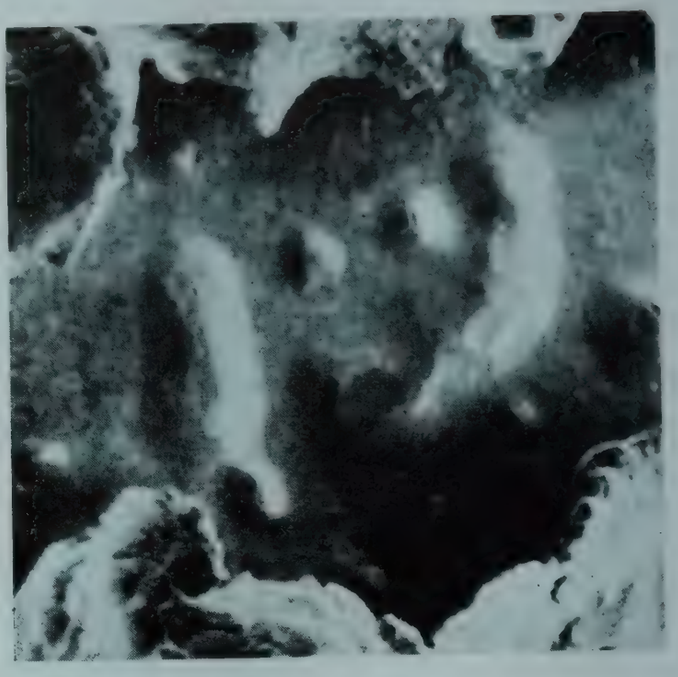

Fig. 7—Opening in exfoliated area (× 200) after annealing at 1273 K

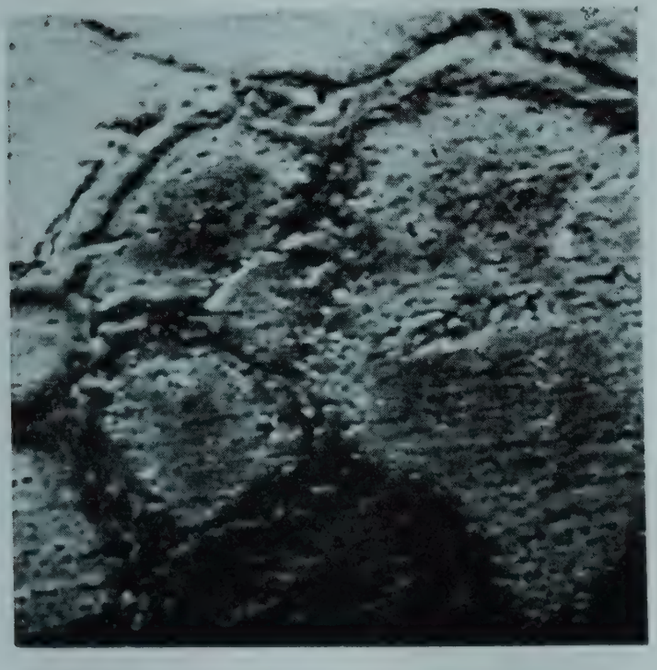

Fig. 6—Specimen surface after annealing at 1273 K, showing grain boundary opening (× 2000)

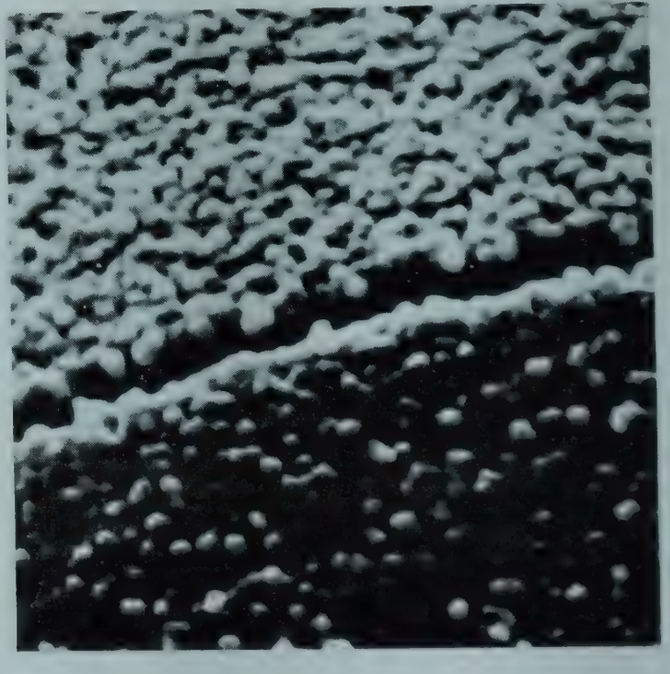

Fig. 8—Inside of exfoliated area (× 4000), after annealing at 1273 K

and Thomas[9] also observed a spongy surface but at low doses and a higher target temperature. In the present case, the target was cooled with chilled water and as such the temperature of the specimen should not be high and this perhaps could explain the absence of a spongy surface.

Annealing studies of the blisters and exfoliations at temperatures of 773 and 1273 K for $7{\cdot}2 \times 10^3$ sec, were carried out for the specimens irradiated to a dose of 5×10^{18} ions/cm^2. No change was observed after annealing at 773 K. Figs. 6, 7 and 8 show the irradiated specimen surfaces, annealed at 1273 K. In Fig. 6, it is seen that some of the grain boundaries have opened up. This could be due to the escape of some helium gas through them. Fig. 7 shows the exfoliated area from different regions of the same specimen after annealing. It is seen that some blister-like things have appeared inside the exfoliated area. Some openings were also seen in some of these blisters from where helium

gas could have escaped. These blisters probably have originated due to the increased mobility of helium gas at a higher annealing temperature. The inside structure of the exfoliated area of Fig. 7 could be seen in Fig. 8. On comparing Figs. 5 and 8, it is seen that the surface structure of the irradiated specimen before and after annealing remains practically identical.

But a major portion of the implanted gas continued to exist inthe specimen. Saturation limit for helium in steel is nearly 50%; however, it has already been reported that nearly 60% of the implanted helium[10] in the blisters continued to exist even on annealing near the melting point. The spherical rough surface (Fig. 8) existing after annealing at 1273 K indicated the presence of helium.

Acknowledgement

The facility of using Van-de-Graaff machine and scanning electron microscope of the Centre is gratefully acknowledged.

References

1. Barnes R S & Mazey D J, *Proc. R. Soc.*, **275** (1963), 47.
2. Primak W & Luthra J M, *J. appl. Phys.*, **37** (1966), 2287.
3. Kaminsky M, *Atomic and ionic impact phenomenon in the metal surfaces* (Springer-Verlag, Heidelberg), 1965.
4. Behrisch R, Risch M, Roth J & Scherzer B M U, *Proc. 9th Symp. fusion technology* (Pergamon Press, New York), 1976, 531.
5. Kulcinski G L & Emmert G A, *J. Nucl. Mater.*, **53** (1974), 31.
6. Agarwala R P, *Proc. Group meeting on ion implantation*, (Department of Physics, University of Bombay, Bombay), Dec. 1976.
7. Das S K & Kaminsky M, *J. Nucl. Mater.*, **53** (1974), 115.
8. Kaminsky M & Das S K, *J. Nucl. Mater.*, **76 & 77** (1978), 256.
9. Bauer W & Thomas G J, *Nucl. Metallurgy*, **18** (1973), 255.
10. Remark J F, Johnson A B, Fasrar H & Atteridge D G, *Nuclear Technol.*, **29** (1976), 369.

Indian Journal of Pure & Applied Physics
Vol. 18, February 1980, pp. 78-80

Origin of Growth Hillocks On the (001) Surface of Lead Molybdate Crystals

K Sreedharan Pillai
Physics Department, M G College, Trivandrum
&
M A Ittyachen
Physics Department, University of Kerala, Trivandrum

Received 26 *December* 1978; *revised received* 9 *July* 1979

Growth hillocks of different shapes and orientations are observed on the (001) surface of lead molybdate crystals. On the basis of surface observations and etching experiments, it is established that these hillocks are formed due to the presence of strained region at the centre, during the early stages of growth. When the thickness of the platelet increases, this strained region gradually disappears from the crystal. During this process, hillocks of different shapes and orientations are formed.

1. Introduction

Surface features of crystal faces can give a lot of information about the history of growth and internal structure of crystals. The existence of internal imperfections of crystals will affect the surface patterns to a great extent by growth process. Hillocks on crystal surfaces are produced due to growth process,[1] natural etching[2] surface nucleation,[3] screw dislocation,[4] etc. The natural hillocks produced by growth, generally show a degree of symmetry corresponding to the face on which they appear, while those produced by other mechanisms do not show any symmetry of the face. The present study reports the origin of different types of growth hillocks observed on the (001) surface of gel-grown lead molybdate crystals.

2. Experimental Procedure

Recently some workers[5] have grown lead molybdate crystals by the gel method. This crystal belongs to the tetragonal system and, in nature, it occurs as wulfenite. The habits of the gel-grown crystals are almost the same as those found in nature. The surface features of these crystals were examined under a metallurgical microscope. During the course of our observations, it was noticed that a large number of platelet crystals were found to have oriented growth hillocks on (001) face. This face was identified by optical goniometric measurements. The platelets were etched in a 1:4 solution of HNO_3 and H_2O and also in one normal sodium hydroxide solution for a period of 2 min at room temperature. The surfaces were coated with thin layers of silver before being optically examined.

3. Observations

Typical platelet crystals on which these investigations were made, are shown in Fig. 1. Measurements showed that these platelets are having bounding edges oriented in <110>, <210> and <100> directions. The thickness of these platelets along the *C*-axis varies from 0·01 to 0·2 mm. The common surface features found on the (001) face are shown in Figs. 2-4. Very thin platelets within the thickness range 0·01 to 0·05 mm were having very smooth plane surfaces. Platelets having thickness between 0·05 to 0·1 mm were having a very small growth hill at the centre (Fig. 2). The shape of the

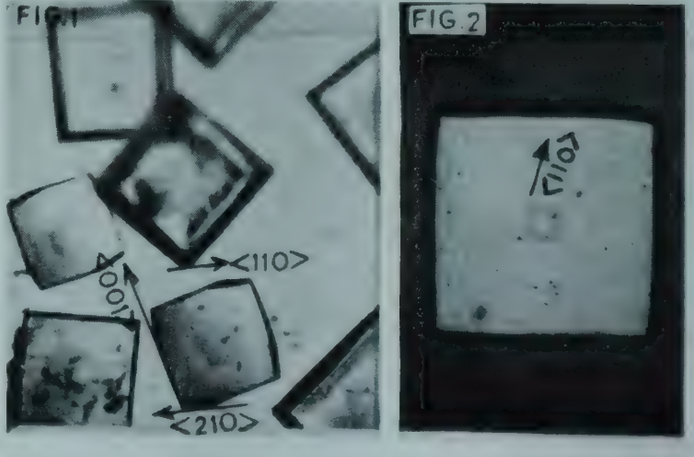

Fig. 1—Typical platelet crystals (× 75)
Fig. 2—Platelets (× 120) having thickness between 0·05 and 0·1 mm with a very small hillock at the centre

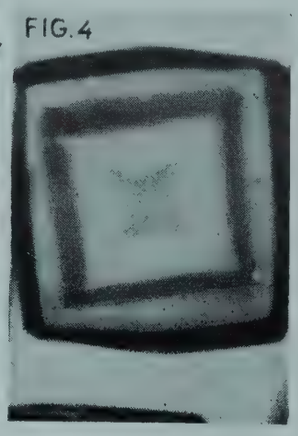

Fig. 3—Platelets (×120) having thickness ranges from 0·10 to 0·15 mm with an irregular hillock [The line indicates the <010> direction]

Fig. 4—Platelets (× 120) having thickness between 0·15 and 0·2 mm with a large hillock at the centre

hillock was square and the sides were oriented in <110> direction. These orientations can easily be identified since the directions of the boundary of the platelet were already measured. The hillocks observed as in Fig. 3 were found on platelets having thickness between 0·1 to 0·15 mm. These hillocks have got two-fold symmetry with four arms denoted by arrows. The direction of the arms were <010>. A very large square hillock having <110> orientation of the sides was found on platelets of thickness between 0·15 and 0·2 mm (Fig. 4). Thick platelets were having practically smooth and plane surfaces. The surface area of these platelets was found to decrease as the thickness increased. The opposite sides of the platelets also showed the same features. Light profile measurements showed that the height of these hillocks vary from 5,000 to 10,000 Å.

These growth features suggest that growth hillocks were originated at the centre of the platelets during the early stages of growth and were undergoing different morphological changes, before disappearing finally, from the fully grown platelets. To study the actual nature of the surface at the centre of the platelet, thin platelet crystals were etched in a solution containing 1:4 nitric acid for 2 min. Etch pit distribution as shown in Fig. 5 was obtained. The following points are noteworthy.

1. Square point-bottomed pits are obtained with their edges parallel to <110> direction. 2. At the centre of the platelet, pits are crowded and from there four branches consisting of rows of pits are formed. 3. The four branches are found to be parallel to <010> direction. 4. On successive etching of the same flake, the size of the pits increases both in extension, and in depth, showing that they are dislocation pits. 5. The same etch patterns could be seen on the opposite side also.

A similar etch pattern was obtained when the platelet (Fig. 2) having a minute hillock at the centre, was etched in the same condition. When the platelet shown in Fig. 3 was etched, the distribution of the pits was more or less the same. It is interesting to note that the direction of the arms of the hillocks are the same as those of the etch pit branches starting from the centre. But the etch pit distribution gets changed when the platelets (Fig. 4) having big square hillock are etched. Here, etch pits are arranged along the straight edges and the four branches are absent (Fig. 6). The density of the pits at the centre is considerably reduced. The orientation of the etch pits inside and outside the hillock are the same. The surface of the thick platelet

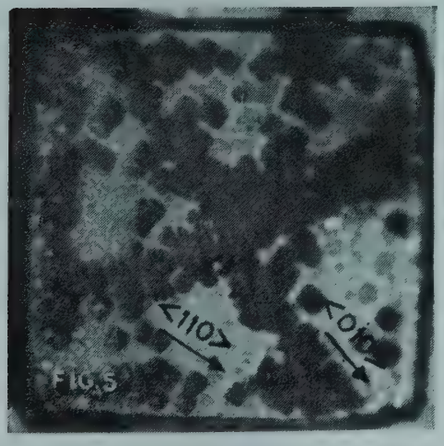

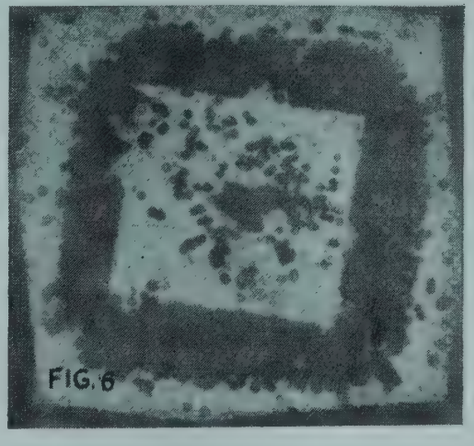

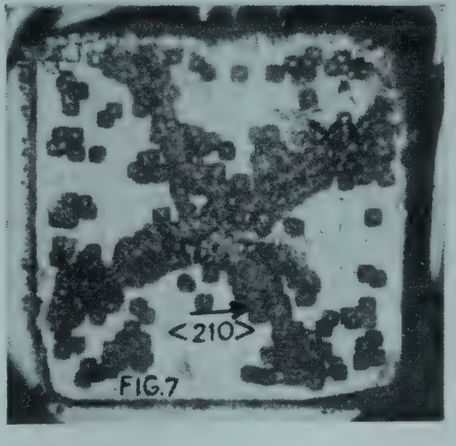

Fig. 5—Etch pit distribution obtained when very thin platelet crystals (× 240) were etched in a 1:4 solution of HNO_3 and H_2O

Fig. 6—Etch pit distribution obtained when platelets (× 120) having a large hillock at the centre were etched

Fig. 7—Etch pit distribution obtained when very thin platelet crystals (× 240) were etched in one normal NaOH solution

when etched, give randomly distributed etch pits of still lower density. A similar distribution of etch pits was observed on the opposite sides of all the platelets.

In order to confirm further that the etch pit distribution is actually due to the nature of the crystal surface, the whole etching experiment was done with one normal sodium hydroxide solution for the same time. In all the cases, the distribution of the pits were the same as before. But here the orientations of the sides of the square pits were in <210> direction (Fig. 7).

4. Discussion

The etch pit distribution on thin platelet crystals resembles the indentation rosettees produced on many crystals.[6,7] The arms of the rosettees will show the direction along which the strain is distributed from the central region of maximum strain. The crowding of the pits at the centre and the appearance of small growth hill at the centre of thin platelets, suggest that some strain might have been introduced at the centre during the early stages of growth. This strained region may cause slip and the resulting movement and introduction of new dislocations could assist the nucleation process. The hillocks shown in Fig. 3 show how the growth layers spread to form the square-shaped hillock, showing the symmetry of the face as in Fig. 4. The density of etch pits on these platelets shows that the strain at the centre disappears as the thickness of the crystal increases, and finally pits were distributed along the edges of the square hillocks. This means that the final tendency of this strain is to move out of the surface when the thickness increases. The absence of both the hillocks and the crowding of of pits at the centre on thick platelets supports this argument.

The oriented square-shaped hillocks sometimes may indicate the twinned region on the (001) face of the crystal. This possibility can be ruled out, because the orientations of the etch pits inside and outside of the hillock are the same.

The change of orientation of etch pits when the etchants are changed, can be due to many factors.[8-12] Here, the change of orientation of the sides of the pits from <110> to <210> direction is considered as due to the configuration of lead and molybdate atoms at the lattice sites of the (001) face and also due to the composition of the etchant. The nitric acid etchant removes the lead atoms from the lattice sites to form lead nitrate, whereas sodium hydroxide solution removes molybdate atoms to form sodium molybdate. The understanding of the mode of attack of these etchants on the lead and molybdate atoms at the lattice sites, to produce change of orientation of the pits, needs further investigations on the actual configuration of these atoms on the (001) face of the crystal.

5. Conclusions

(a) It is established that during the early stages of growth there exists a strained region at the centre of the (001) surface of all the platelet crystals of lead molybdate grown in gels.

(b) During the later part of the growth, this strained region may cause slip and introduction of new dislocations, which could assist the nucleation of differently shaped growth hillocks.

(c) It is also established that the etchants reported, can produce change of orientation on the (001) surface of lead molybdate crystals.

Acknowledgement

One of the authors (KSP) would like to express his gratitude to the University Grants Commission, New Delhi, for financial assistance.

References

1. Batterman B W, *J. appl. Phys.*, **28** (1957), 1236.
2. Buckely H E, *Crystal growth*, (John Wiley, New York), 1951.
3. Joshi M S & Vagh A S, *Br. J. appl. Phys.*, 17 (1966), 529.
4. Verma A R, *Nature, Lond.*, 168 (1951), 783.
5. Sreedharan Pillai K & Ittyachen M A, *J. Crystal Growth*, **39** (1977), 287.
6. Patel A R & Bhat H L, *J. Phys.*, 4 (1971), 1998.
7. Chen C C & Hendrickson A A, *J. appl. Phys.*, 42 (1971), 2208.
8. Haribabu V & Bansigar K G, *J. Crystal Growth*, 2 (1968), 9.
9. Ives M B, *J. Phys. Chem. Solids*, 24 (1963), 275.
10. Joshi M S & Ittyachen M A, *J. Crystal Growth*, 2 (1968), 47.
11. Katsushiro Kawabuchi, *J. Crystal Growth*, 11 (1971), 92.
12. Patel A R & Singh R P, *J. Crystal Growth*, **2** (1968), 373.

Indian Journal of Pure & Applied Physics
Vol. 18, February 1980, pp. 81-83

Effect of *p*H on the Liesegang Ring Formation of lead Carbonate Crystals

K Mohanan Pillai, M A Ittyachan & V K Vaidyan
Department of Physics, University of Kerala, Kariavattom, Trivandrum 695 581

Received 6 *December* 1978; *revised received* 14 *May* 1979

Liesegang ring formation of lead carbonate crystals were studied from a *p*H range of 6-8 at room temperature. Below a *p*H value of 7, discrete rings are formed while above *p*H=7, interconnected rings are formed. Long crystals are formed at low *p*H values and small ones at high *p*H. Also, the time of formation of the rings decreases and the number of rings increases with *p*H. These are attributed to the differences in solubility of the crystals formed and structure of the gel, at different *p*H values.

1. Introduction

The study of Liesegang rings[1] were considered interesting partly because their origin was obscure and partly because they were reminiscent of certain structures found in nature, e.g. the striations of agate. The Liesegang ring phenomenon itself is even now only imperfectly understood. Periodic ring and layer formations found in nature offer only the most limited opportunities for research into their origin. Indeed, many are due to different mechanisms.[2]

Compounds which can form periodic precipitation are listed in a review by Stern[3] in which lead carbonate is included. Liesegang ring formation of lead carbonate was reported by Mohanan Pillai and Ittyachan.[4] The formation of these rings were found to be influenced by different factors like *p*H of the medium, concentration of the electrolyte, density of the gel medium and type of the gel. The application of external electric and magnetic fields were also found to affect the periodic precipitation. A preliminary work on the effect of *p*H on the formation of Liesegang rings is reported in this paper.

2. Experimental Details

Equal volumes (10cc) of sodium silicate solution of density 1·03 g/cc and 0·1 *M* ammonium carbonate solution were mixed together and the *p*H value is adjusted using acetic acid. This solution was kept in test tubes of length 15 cm and diameter 2·75 cm for the required time to gel. Experiments were conducted in gels having *p*H range 6-8 at room temperature (about 28°C).

3. Results and Discussion

After the gel had set, 20 cc of 0·2 *M* lead nitrate was poured over the gel. Rings were observed to form only from an initial *p*H of 6·35. In all cases, a white band is formed at the top of the gel column below which periodic precipitation occurs. The white band and one or two rings near the band were found to disappear within 10 days of its formation. As the *p*H increases, it took a longer time for the disappearance of the band and above 7·4 *p*H, this phenomenon was not found to occur. When the concentration of the outer electrolyte was increased from 0·2 *M* to 1 *M*, the disappearance was found to be quick and more rings were found to disappear. The observations can be grouped into two sections :

(1) *p*H range 6-7 and (2) *p*H range 7-8.

3.1 *p*H range 6-7

Discrete rings were formed from a *p*H of 6·35-7. Up to a *p*H value of 6·75, the ring system consists of long interpenetrated needle-like crystals of almost the same size in each ring as shown in Fig. 1. From a *p*H of 6·8-7, two types of crystals were found to form in each ring. The crystals formed at the top region of each ring were found to be long, while those below were short. Fig. 2 shows this type of ring formation. When the *p*H of the medium is increased, more number of crystals are formed. Also the number of rings is found to increase with *p*H. Table 1 gives the number of rings formed and the description of the crystals observed at different *p*H values. As the *p*H is increased, the formation of the rings were found to be quick. Also the width of the rings and spacings between them decreased.

3.2 *p*H range 7-8

Separate rings were not found to form above a *p*H value of 7. Here, each ring consists of a large number of small interpenetrated crystals. Also, the

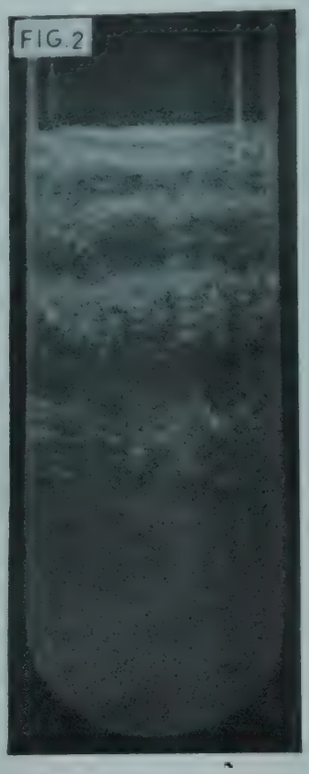

Fig. 1—Ring system showing long interpenetrated needle-like crystals of almost the same size in each ring (*p*H 6·35-6·75)

Fig. 2—The system showing two types of crystals in each ring: long crystals at the top and small crystals at the bottom (*p*H 6·8-7·0)

rings were found to be interconnected. The nature of ring systems formed at different *p*H values are described below. At a *p*H value of 7-7·2, instead of flat discs, concave shaped discs were formed. These discs were connected by a spiral going around each disc. The spiral starts from the rim of one disc, going around the space between the discs for some distance and joins with the neighbouring disc. The positions at which the spiral leaves each disc are along a straight line and so are the positions at which the spiral joins each disc. Actually, the ring systems are in the form of a spiral stair case with a circular platform at each turn of the spiral. Fig. 3 shows the ring patterns observed. The complete spiral pattern is visible only when we rotate the growth apparatus.

When the *p*H was in the range of 7·25-7·35, each ring consisted of two concave-shaped discs which were separated at the rim, and were joined together at the centre where there is a depression. The two discs in each ring were connected to the two discs in the neighbouring ring by two joints starting from the edges of the discs. It is interesting to note that the top discs were connected by one joint and bottom discs by another joint. Fig. 4 illustrates the ring systems observed. In all these cases, the gel took one day to set completely. The gel took 8 to 12 days to set in the *p*H range 7·4-8. The Liesegang patterns observed at a *p*H of 7·40-7·60 is shown in Fig. 5. Here each disc was not completely filled by the crystals but was divided into 4 parts. The two parts were connected to the two parts of the top disc and the other two parts were connected to the lower disc in the same fashion. A large number of microscopically small crystals were found in the spaces between the discs.

Convex-shaped rings were observed at a *p*H value of 7·70-8. Each ring was connected to the top through the centre and also through the sides by

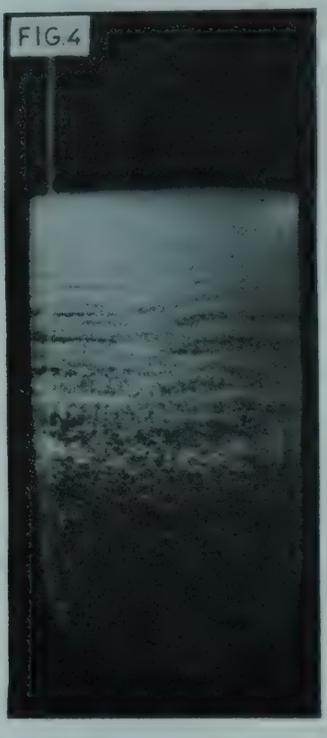

Fig. 3—Staircase formation of Liesegang rings (*p*H 7·0-7·2)

Fig. 4—Double ring formation of Liesegang phenomena (*p*H 7·25-7·35)

Table 1—Effect of *p*H on the Number of L-rings and the Nature of the Crystals Formed

*p*H value	Number of rings	Description of crystals formed
6·30	Nil	
6·35	1	Interpenetrated long needle-like crystals in each ring
6·40	2	
6·50	3	
6·75	5	
6·90	8	Interpenetrated long crystals at the top and small ones at the bottom
7·00	9	
7-8	Inter-connected rings	Small interpenetrated crystals

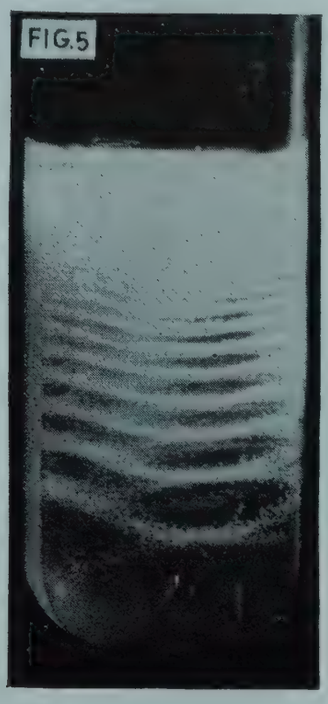

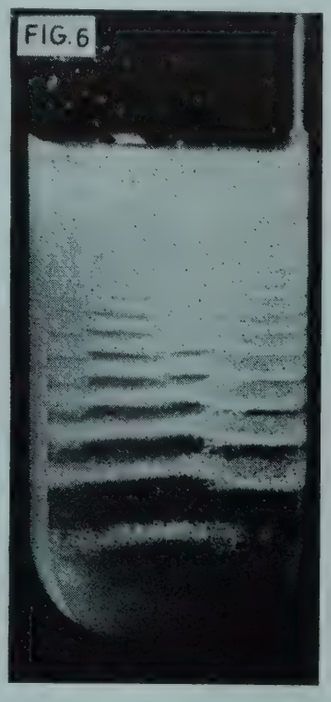

Fig. 5—Partially filled interconnected Liesegang rings (*p*H 7·4-7·6)

Fig. 6—Liesegang rings observed in the *p*H range 7·7-8·0

two arms. Both these connections gradually disappeared towards the bottom of the diffusion column as can be seen in Fig. 6.

It is generally accepted that the crystal shape can be modified by changing crystallization conditions such as concentration, *p*H, solvent used, temperature, etc.[5-7] The different sizes of crystals formed in our experiment at various *p*H values can be explained as due to the effect of *p*H. As the solubility of crystals formed is more at low *p*H, nucleation is relatively difficult at low *p*H compared to that at high *p*H. Hence at high *p*H, large number of smaller crystals and at low *p*H, less number of larger crystals are formed. The range of *p*H 6·8-7 can be considered to be an intermediate stage for change of crystal size from long needle-shaped to small ones. At this stage, each ring itself consists of two types of crystals, large crystals at the top and small ones at the bottom. This may be due to slight variations in *p*H and concentration of ions at the starting and finishing of each precipitation zone.

Solubility of lead carbonate is more at low *p*H values. The *p*H value of the outer electrolyte is in the range of 3 to 4. At first, precipitation forms in the gel near the outer electrolyte and a band is formed at the top. As time increases, more outer electrolyte diffuses into the gel, which decreases the *p*H value thereby increasing the solubility of the crystal in the medium from the top. Hence the precipitate starts disappearing from the top. To form a precipitate from two electrolytes in a gel medium or solution, a critical concentration of both of them is required.[8] At low *p*H values, the solubility of lead carbonate is more. Hence, the critical concentration of ions required for nucleation may be more than that required at high *p*H. This explains for the slow formation and less number of rings at low *p*H. The structure of the gel has great influence on the formation of periodic precipitation.[9,10] As *p*H increases, the gel structure changes from a distinctly box-like network to a structure consisting of loosely bound platelets which appear to lack cross linkages.[11] The structure of the gel at the walls and centre of the growth apparatus are different due to unequal settings.[3] The different ring patterns observed at *p*H values above 7 can be attributed to these effects. Hence, the size of the crystals formed and the nature of the rings are considerably influenced by the *p*H of the gel medium.

Acknowledgement

One of the authors (K M P) is grateful to the University Grants Commission, New Delhi, for financial assistance.

References

1. Liesegang R E, *Naturw. Wochschr*, **11** (1896), 353.
2. Herisch H K, *Crystal growth in gel*, (The Pennsylvania State University Press, London), 1973, 14.
3. Stern K H, *Chem. Rev.*, **54** (1954), 79.
4. Mohanan Pillai K & Ittyachan M A, *Pramana*, **10** (1978), 613.
5. Mullins J W, *Crystallization* (C R C Press, Clevaland, USA), 1972, 207.
6. Garrett D E, *Br. Chem. Engng.*, **4** (1959), 673.
7. Shternberg A A, in *Growth of Crystals*, Vol. 9, Ed. N N Sheftal and E I Givargizov (Consultants Bureau, New York), 1975, 34.
8. Kirov G K, *J. Crystal Growth*, **15** (1972), 102.
9. Matalon R & Packter A, *J. Colloid Sci.*, **10** (1955), 46.
10. Stern K H, *J. Colloid Sci.*, **9** (1954), 329.
11. Halberstadt E S, Henisch H K, Nickl J & White E W, *J. Colloid Interface Sci.*, **29** (1969), 469.

Indian Journal of Pure & Applied Physics
Vol. 18, February 1980, pp. 84-86

Dependence of The C-V Index of a Hyperabrupt Junction on Junction Parameters

A K Datta, K Ghosh, S B Roy, T B Biswas & N K D Choudhury

Institute of Radio Physics & Electronics, University College of Technology, Calcutta 700 009

Received 22 *April* 1979

Dependence of the C-V index n on junction parameters has been studied assuming a practical diffusion profile, viz. a complementary error function or a Gaussian type of distribution in the retrograded side of a hyperabrupt junction. The maximum value of n (n_{max}) for both the distributions is found to vary with the ratio of the background doping concentration to the cross-over concentration (R_0) in the retrograded region. A comparison with that of an exponential distribution shows that for a given value of R_0, n_{max} is highest for the Gaussian and lowest for the exponential. The results are in good agreement with the experimental data available in literature.

1. Introduction

In various practical applications of varactor diodes, the C-V index n, defined by $n = -\,\mathrm{d}(\log C)/\mathrm{d}(\log V)$ where C and V represent the junction capacitance and junction voltage respectively, is a parameter of considerable significance. While it is desirable that its value should remain constant as the junction voltage is varied, it is known[1-3] that this requirement is not satisfied in practice and both the value of n and its dependence on the junction voltage are governed by the nature of the impurity distribution on the two sides of the junction. For hyperabrupt Schottky diodes, these parameters are governed by the nature of the impurity profile in the semi-conductor.

Now practical hyperabrupt p-n junctions or Schottky diodes are fabricated by the process of diffusion or ion-implantation and the impurity distribution on the retrograded side may either be Gaussian, complementary error function or exponential in nature. For the exponential distribution, the effect of the junction voltage on the parameter n has been studied by Gupta *et al.*[4,5] A similar study for the other two types of distributions does not appear to have been made so far. In this paper, a study has been made on the dependence of n on junction parameters assuming a Gaussian and a complementary error function type of distribution in the retrograded region.

2. Theory

Let us assume that the retrograded side of the semiconductor is of n-type and the impurity concentration $N(x)$ for the Gaussian and complementary error-function distribution at any point x in this region is given by,

$$\text{Gaussian } N(x) = (N_0 - N_B)\exp(-x^2/L^2) + N_B \quad \ldots(1a)$$

Complementary Error Function (erfc)

$$N(x) = (N_0 - N_B)\,\mathrm{erfc}\,(x/L) + N_B \quad \ldots(1b)$$

where N_0 is the concentration at the junction ($x=0$), N_B the background concentration and L the characteristic length whose value is governed by the nature of the impurity profile and the temperature and time of diffusion. It is also assumed that the space-charge region is restricted entirely to the n-side. Substituting Eq. (1) in Poisson's equation and integrating twice, one can obtain the expression for potential distribution in the space-charge region as a function of x on the retrograded side, from which the expression for normalized voltage V_n comes out to be,

$$\text{Gaussian } V_n = \frac{(1 - R_0)}{2}\left[\exp\left(-1/C_N^2\right) - 1\right] - \frac{R_0}{2C_N^2} \quad \ldots(2a)$$

$$\mathrm{erfc}\, V_n = (1 - R_0)\left[-\frac{1}{2C_N^2} - \left(\frac{1}{4} - \frac{1}{2C_N^2}\right)\mathrm{erfc}\left(\frac{1}{C_N}\right) + \frac{1}{2\sqrt{\pi}}\exp\left(-1/C_N^2\right)\right] - \frac{R_0}{2C_N^2} \quad \ldots(2b)$$

where

$$R_0 = \frac{N_B}{N_0}\,,\quad V_n = -\frac{V(W)}{V_0}\,,\quad V_0 = qN_0L^2/\epsilon_s$$

and $C_N = L/W$ is the normalized capacitance, W depletion layer width, ϵ_s the permittivity of silicon and q the electronic charge. From Eqs. (2a) and (2b), the expression for the C-V index n for the two distributions considered, can be obtained using the formula $n = -\dfrac{\mathrm{d}(\log C_N)}{\mathrm{d}(\log V_N)}$ and are given by

$$n_{Gaussian} = \frac{C_N^2\{(1-R_0)/2\}\{1-\exp(-1/C_N^2)\}+R_0/2}{(1-R_0)\exp(-1/C_N^2)+R_0} \quad ...(3a)$$

$$n_{erfc} = \left[C_N^2 \frac{(1-R_0)}{2} \left\{ \frac{1}{C_N^2} + \left(\frac{1}{2} - \frac{1}{C_N^2} \right) \right.\right.$$
$$\left.\left. \text{erf}\left(\frac{1}{C_N}\right) - \frac{1}{\sqrt{\pi} C_N} \exp(-1/C_N^2) \right\} + \frac{R_0}{2} \right] \Big/$$
$$\left[(1-R_0) \left\{ 1 - \text{erf}\left(\frac{1}{C_N}\right) \right\} + R_0 \right] \quad ...(3b)$$

3. Results and Discussion

Fig. 1 shows a plot of n as a function of C_N with R_0 as a parameter for the erfc distribution in the retrograded region. From Fig. 1, it is evident that the nature of the curve is identical to that for an exponential distribution as reported by Gupta and Tyagi.[5] For Gaussian distribution also, the n versus C_N plot is similar in nature. The difference between the curves is that the maximum value of n (n_{max}) for the three distributions are different. Also, values of C_N at which the maximum occurs are different for the three distributions.

Fig. 2 shows a plot of n_{max} versus R_0 obtained from the curves of Fig. 1. Fig. 2 also includes similar curves for the Gaussian and exponential distributions. From Fig. 2, it is evident that in all cases, the value of n_{max} decreases as the value of R_0 is increased. As R_0 tends to unity, n_{max} approaches 0·5, behaving like an abrupt junction. It is obvious that since $R_0 = N_B/N_0$, one can easily determine the value of n_{max} if the exact nature of the profile and the values of N_0 and N_B are known.

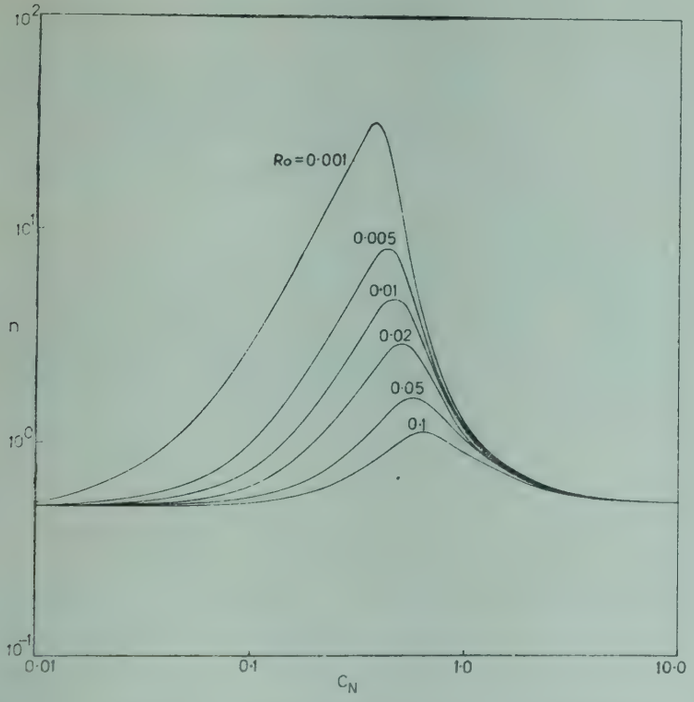

Fig. 1—Variation of n with C_N with R_0 as a parameter for erfc distribution in the retrograded region.

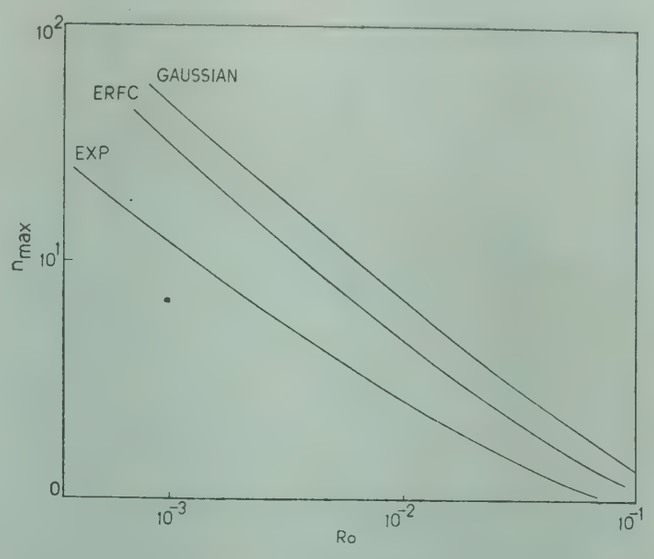

Fig. 2—Variation of n_{max} with respect to R_0 for exp, erfc and Gaussian distributions

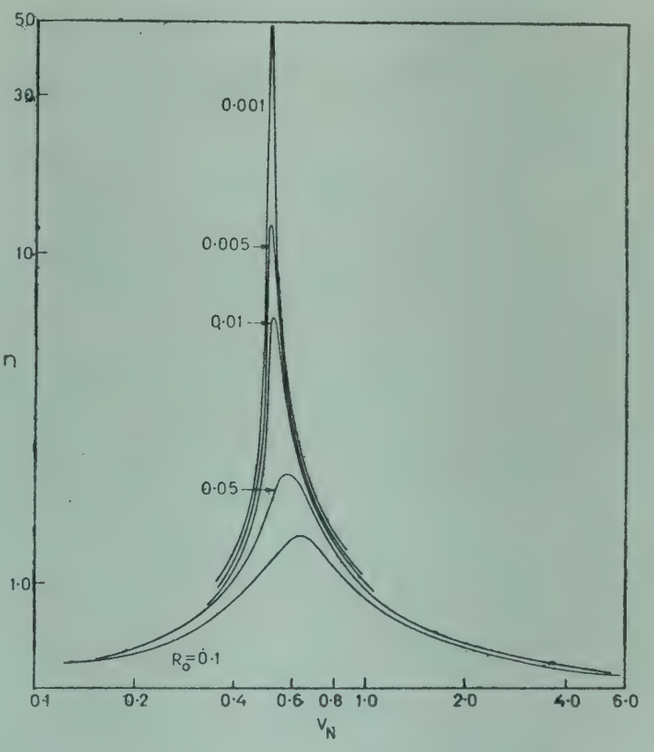

Fig. 3—Variation of n with the normalized voltage V_N for the Gaussian distribution

Figs. 3 and 4 give plots of n as a function of normalized voltage (V_N) for the Gaussian and erfc distributions respectively. It is to be noted that for both the distributions, the curves are sharper than those for an exponential distribution. Accordingly, the exponential distribution is preferable for applications where n is required to remain substantially constant with a small change of voltage. Also, the value of n is maximum when V_N is in the range 0·5-0·62 for a Gaussian profile and in the range 0·25-0·35 for an erfc profile as compared to the range 1 to 1·2 for the exponential profile. Another

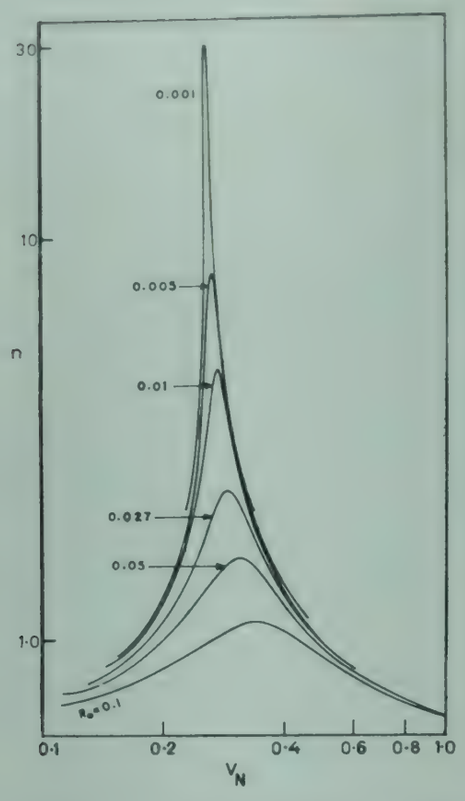

Fig. 4—Variation of n with the normalized voltage V_N for the erfc distribution.

point of interest is that for both the distributions, the peaks shift towards the right as the value of R_0 is increased.

In order to test the validity of the expressions derived, the data reported by Brook and Whitehead[6] were considered. An analysis of the plot of the impurity density versus junction depth given by the authors for their Au-n Si Schottky diodes fabricated by ion implantation technique shows that the said impurity distribution may be described by an erfc profile with $N_0 = 3{\cdot}58 \times 10^{17}$ atom/cm^3 and $N_B = 1 \times 10^{16}$ atom/cm^3. This gives an R_0 value of $2{\cdot}7 \times 10^{-2}$ for which the corresponding n_{max} value from Fig. 2 is 2·34. This value is in fair agreement with the maximum value 2·1 of n as was obtained from point-to-point calculation of the slope of the C-V curve given in the aforesaid work.

Tyagi and Gupta[4] calculated n_{max} values for an assumed exponential profile for their experimental diode and showed it to be equal to 2·4, which they claimed to be very close to the experimental value, viz. 2·1 obtained from C-V measurements. However, as these authors have remarked, practical diffusion profiles are either erfc or Gaussian in nature. If we assume the distribution to be erfc in nature, the measured n_{max} value of 2·1 should correspond to an R_0 value of $3{\cdot}15 \times 10^{-2}$, from which N_0 comes out to be about $0{\cdot}33 \times 10^{17}$ atom/cm^3 for a background doping of 1×10^{15} atom/cm^3. Comparing this value of N_0 with the value given by Tyagi and Gupta, i.e. 1×10^{17} atom/cm^3, and noting the likely inaccuracies involved in the determination of the latter from C-V data, one can conclude that the observed n_{max} value of their diode may be stisfactorily explained on the basis of an erfc distribution and an exponential distribution need not be assumed.

For the second experimental diode of the aforesaid authors, the measured n_{max} value of 2·8 obtained from their C-V data corresponded to an R_0 value (from Fig. 2) of $2{\cdot}1 \times 10^{-2}$ (and hence $N_0 = 0{\cdot}5 \times 10^{17}$ atom/cm^3) for the erfc distribution and a value of 9×10^{-3} (and hence $N_0 = 1{\cdot}11 \times 10^{17}$/cm^3) for an exponential distribution. They also reported an N_0 value of $6{\cdot}5 \times 10^{16}$ atom/cm^3 (measured) which obviously is very close to the N_0 value obtained from erfc distribution, proving that the profile should better be represented by an erfc distribution and not by an exponential one.

Acknowledgement

The authors wish to express their deep gratitude to Prof. A N Daw for his keen interest and constant encouragement during the progress of the work.

References

1. Watson H A, *Microwave semiconductor devices & their applications* (McGraw-Hill, New York), 1967, 194.
2. Nakanuma S, *IEEE Trans.*, **ED13** (1966), 578.
3. Sukegawa T, Sakurai T & Nishizawa J, *IEEE Trans.*, **ED13** (1966), 988.
4. Tyagi M S & Gupta A K, *Indian J. pure appl. Phys.*, **15** (1977), 152.
5. Gupta A K & Tyagi M S, *Solid-st. Electron.*, **21** (1978), 507.
6. Brook P & Whitehead C S, *Electronics Lett.*, **4** (1968), 335.

Indian Journal of Pure & Applied Physics
Vol. 18, February 1980, pp. 87-90

Measurements of Self-Diffusion Coefficients in Hg & Ga by a Radioactive Tracer Technique

A Basu, S N Changdar & A M Ghose
Nuclear Physics Laboratory, Bose Institute, Calcutta 700 009

Received 30 *October* 1978; *revised received* 23 *February* 1979

Measurements of self-diffusion coefficients in Hg and Ga have been made using a method based on radioactive tracer technique. In this method, the solute and the solvent columns are of equal length and the detector is placed in a vertical geometry over the diffusion column. The Stokes-Einstein radius and the Eyring rate constants for these metals have been calculated. The experimental data are compared with the data of other workers and analyzed in the light of existing theories of liquid metals.

1. Introduction

In this paper the results of self-diffusion coefficients of liquid Hg and Ga measured over a range of temperature by a simple and accurate method based on radioactive tracer technique are presented. The experimental geometry consists of solute and solvent columns of equal lengths with the radiation detector placed vertically over the diffusion cell. For the above experimental conditions when $kt > 0{\cdot}5$ where $k = \frac{\pi^2 D}{4L^2}$, D the diffusion coefficient, and $2L$ the total length of the diffusion column, in the Fourier expansion solution of Fick's second law of diffusion

$$\frac{\delta c\,(x,t)}{\delta t} = D\ \frac{\delta^2 c\,(x,t)}{\delta x^2} \qquad \ldots(1)$$

all even order terms vanish and it is adequately represented by the first term,

$$N_0 - N_t = A \exp(-kt) \qquad \ldots(2)$$

where, N_t is the count rate at time t and N_0 is the count rate when the solute and the solvent columns are completely mixed up. A is a constant depending on geometry which is eliminated when the ratios of $(N_0 - N_t)$ at different values of t are taken. Thus, D can be measured by noting the variation of $(N_0 - N_t)$ with time.

2. Experimental Details

The diffusion cell is constructed on the principle of sliding cell technique. It essentially consists of two stainless steel slabs which are placed in a brass vessel. The lower steel slab was kept fixed with respect to the brass vessel whereas the upper slab could be slowly moved with respect to the lower one by means of a sliding screw arrangement. The central cavity L (Fig 1) in the lower slab together with the hole M in the upper slab constituted the diffusion column proper. There was another hole N in the upper slab for filling L with the radioactive solute. The diameter of the diffusion column (0·6 cm) was relatively larger than what is normally used, and it was chosen so as to reduce the curvature of the open liquid surface. The cavity L was accurately machined at the bottom to have as flat a surface as possible, so that the depth at different points did not differ by more than 0·1%. Stainless steel slabs were used to get the diffusion cells accurately machined though it is known that there are other better conductors of heat than stainless steel. Convection effect due to the finite radius of the diffusion cells was studied by using cells of various radii; the effect was found to be negligible. The possibility of temperature gradient was minimized to a great extent by keeping the diffusion cell in a constant temperature bath for several hours before the start of the experiment. Broome and Walls[1,2] reported the diffusion experiments on liquid metals, mercury and gallium by a modified version of sheared boundary

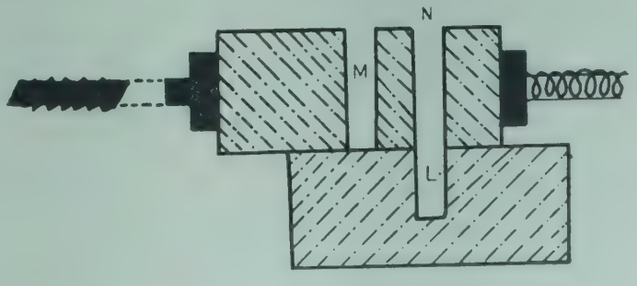

Fig. 1—Schematic diagram of the experimental set-up

method and the temperature range was higher than that used in the present experiment.

Proper precautions were taken to remove mechanical vibrations. The 5819-type photomultiplier tube coupled to an anthracene crystal was placed vertically over the diffusion column. The photomultiplier was connected to a highly stable electronic circuit whose long term stability was checked to within $\pm$ 0·1% for a period of 24 hr.[3] As it will be seen from the working formula, the adjustment of the solute and the solvent columns to equal height presents the principal source of practical difficulty and consequently of the experimental uncertainty of the observed results. However, with the method adopted by us, the lengths could be adjusted within $\pm$ 0·002cm without any difficulty and hence the experimental accuracy has been considerably improved.

For measurements with Hg diffusion cells with diffusion column lengths 2 cm and diameter 0·6 cm were used. The amount of Hg required to fill the lower cavity was weighed by means of a sensitive balance. It was then poured through the hole of the upper slab. The lower cavity was then filled up with radioactive solute having ^{203}Hg as the tracer through the other hole of the upper slab. Then by the sliding screw arrangement, the solvent column was superposed on the solute column. Readings were generally taken after one hour of the start of the diffusion process. The measurements with Hg were made in the temperature range 5-80 °C. The results in the temperature range 5-40°C have been reported earlier.[4]

The diffusion coefficient of Ga was also measured using the above technique. The tracer employed was ^{72}Ga and the temperature range of the measurements was 37-80 °C. Proper precautions were taken to prevent the formation of oxide films on the surface of the gallium column.

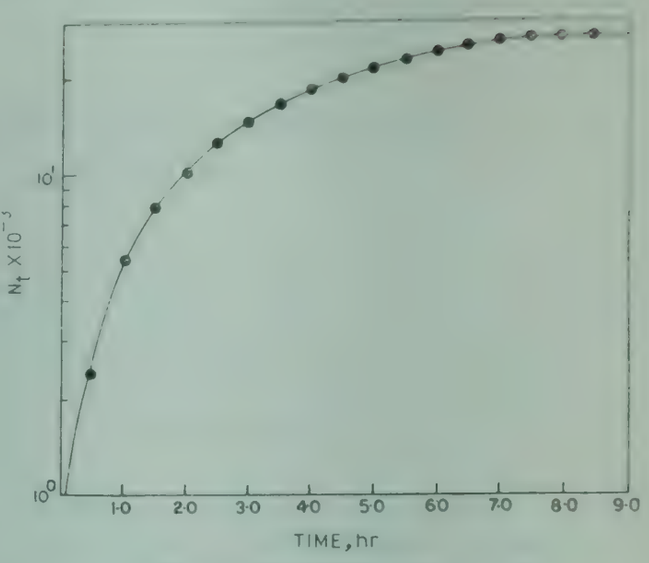

Fig. 2—Plot of N_t versus t

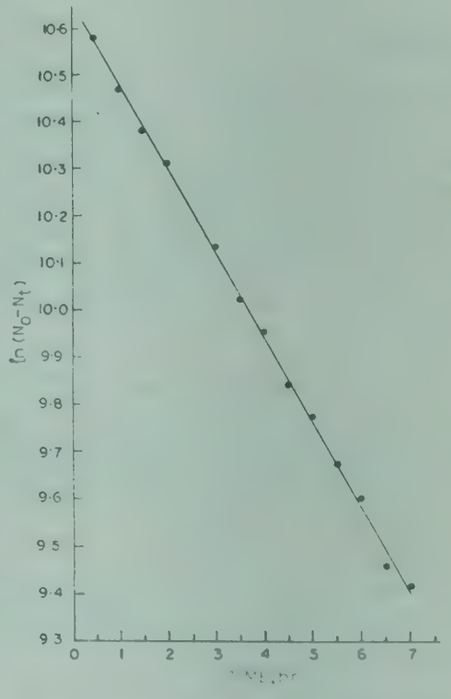

Fig. 3 – Plot of (N_0-N_t) versus t

3. Results and Discussion

Fig. 2 represents a typical N_t versus t curve for Ga. Fig. 3 gives a $\log_e (N_0 - N_t)$ plot against t. Fig. 4 gives the log D versus $1/T$ curve for both the metals. The data compare well with those obtained by other workers.[5–8] It was seen that the results obtained by Hoffman[5] with his capillary technique are somewhat higher than ours. A possible reason may be that the 250 rpm of the stirrer somewhat disturbed the diffusion process and there is a convective loss of ^{203}Hg from the capillary. The results obtained by Nachtrieb and Petit[7] are lower than those of ours. This may be due to the fact that the values of D obtained by shearing cell technique used by these authors are neither differential nor integral diffusion coefficients in the true sense. Larsson *et al.*[6] used modified capillary method for diffusion measurements in Ga over a wide range of temperature (20-283 °C). The reproducibility of the measured diffusion coefficients by this method is $\pm$ 2·5%, whereas in our method the reproducibility can be achieved within $\pm$ 1% and hence in that sense the method employed by us is more consistent. It is also to be noted that our method is free from the major trouble of diffusion experiments, viz. zero-time correction.

The transport properties, viscosity and diffusion are closely linked. One relationship which connects the viscosity and diffusion is due to Stokes-Einstein

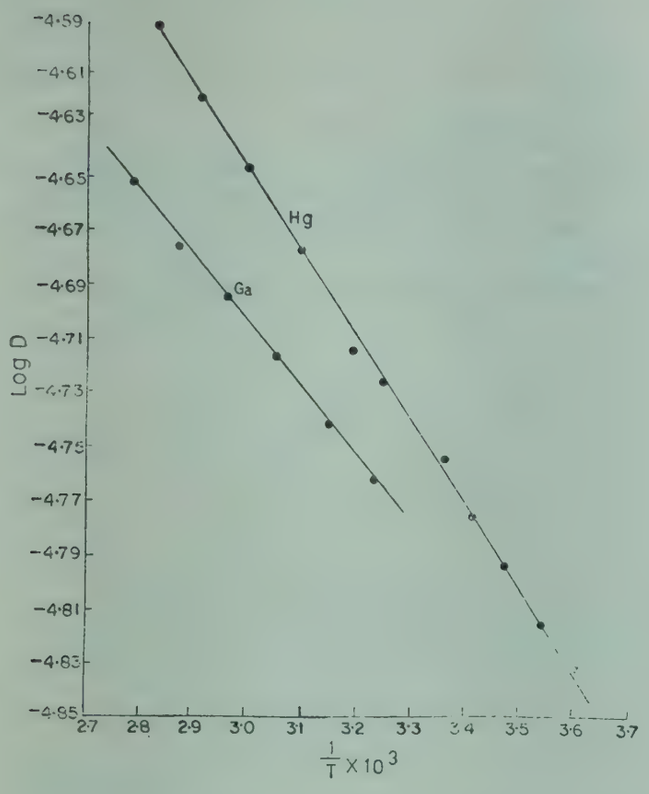

Fig. 4—Plot of D versus T

viz. $r = kT/6\pi\eta D$. In the derivation of this equation, the liquid is treated as a continuous medium. Hence there is some theoretical restriction on the validity of using this equation in the case of Hg and Ga. However, by substituting the observed data into the above equation we obtain the Stokes-Einstein radius, for Hg as 0·81 Å, which is in close agreement with the theoretical prediction. This situation can be explained if conduction electrons are assumed to effectively screen the diffusion ions to provide a kind of hydrodynamic continuum so far as charge is concerned. In the temperature range 40-80°C, r for Ga varies in the range 0·61-0·69 Å. This variation may be attributed to the inaccurate viscosity data of gallium.[9]

Eyring[10] explained the transport properties like viscosity and diffusion by means of the hole and jump theory. We consider two layers of molecules in a liquid at a distance λ_1 apart and we suppose one slips past the other under the influence of an applied force. Let the distance between two neighbouring molecules over a plane of liquid be λ_2 and λ_3. Then, $\lambda_1\ \lambda_2\ \lambda_3$ is the volume available to a single diffusing molecule. The coefficient of diffusion in terms of λ_1, λ_2 and λ_3 and the absolute temperature can be expressed as

$$D = \frac{\lambda_1\, kT}{\lambda_2\, \lambda_3 \eta} \qquad \ldots(3)$$

Table 1—Values of η, ρ and D Calculated for Hg, Ga and Pb at Different Temperatures

Temp., K	η, P	$D \times 10^5$ cm^2 sec^{-1}	ρ, gm cm^{-3}	λ_1, Å	$(\lambda_2\lambda_3)^{1/2}$ Å
		Mercury			
278·2	0·01649	1·48	13·5831	1·253	4·424
293·7	0·01560	1·68	13·5438	1·266	4·408
308·2	0·01482	1.88	13·5095	1·275	4·397
323·1	0·01402	2·10	13·4729	1·282	4·391
343·2	0·01267	2·40	13·4243	1·296	4·425
353·1	0·01242	2·55	13·4001	1·305	4·441
		Gallium			
310·0	0·02054	1·73	6·0913	1·263	3·885
328·0	0·01897	1·92	6·0775	1·244	3·918
348·0	0·01752	2·11	6·0613	1·218	3·964
358·0	0·01690	2·23	6·0525	1·214	3·975
		Lead			
613·0	0·0189	2·427	10·673	1·327	4·929
649·0	0·0167	2·698	10·629	1·343	4·909
692·0	0·0160	3·673	10·579	1·420	4·786
743·0	0·0144	4·580	10·520	1·456	4·740

By assuming $(\lambda_1\ \lambda_2\ \lambda_3)$ to give the effective volume of a single molecule, this quantity can be calculated from the molar volume. Combining the values for $\lambda_1/(\lambda_2\ \lambda_3)^{1/2}$ and $(\lambda_1\ \lambda_2\ \lambda_3)$, the results obtained for Ga, Hg and Pb (the viscosity and diffusion data of lead were taken from literature[11]) are reported in Table 1.

It is seen from Table 1 that λ_1 for Hg and Pb increases with temperature and $(\lambda_2\ \lambda_3)^{1/2}$ decreases, whereas the reverse is the case for Ga. This discrepancy is probably due to the anomalous behaviour of gallium near the melting point. Most of the solids increase in volume on melting but Ga shows the opposite trend. The values of λ_1 and $(\lambda_2\ \lambda_3)^{1/2}$ show this fact.

According to Swalin,[12] diffusion in liquid metals results from the movement of atoms as a result of local density fluctuations. His method reveals an absence of any activation energy for the process but a plot of log D versus T^{-1} yields an apparent straight line over a small temperature interval. Our observed data for Hg and Ga also show the same trend.

References

1. Broome E F & Walls H A, *Trans. metall. Soc. A.I.M.E.*, 242 (1968), 2177.
2. Broome E F & Walls H A, *Trans. metall. Soc. A.I.M.E.*, 245 (1969), 739.

3. Changdar S N, *Measurement of self-diffusion coefficients in liquids by radioactive tracer techniques*, Ph D thesis, Calcutta University, Calcutta, 1970.

4. Changdar S N, *Proc. Nucl. Phys. and Solid State Phys. Symp., Madurai*, (Department of Atomic Energy, Govt. of India, Bombay) Vol. 3, (1970), 347.

5. Hoffman R E, *J. chem. Phys.*, **20** (1952), 1567.

6. Larsson S, Broman L, Roxbergh C & Lodding A, *Z. Naturf.*, **25a** (1970), 1472.

7. Nachtrieb N H & Petit J, *J. chem. Phys.*, **24** (1956), 746.

8. Nachtrieb N H & Petit J, *J. chem. Phys.*, **24** (1956), 1056.

9. Spells K E, *Proc. phys. Soc.*, **48** (1936), 299.

10. Eyring H, Glasstone S & Laidler K, Theory of rate processes (McGraw-Hill, New York), 1941, Chap. 9.

11. Vadovic C J & Colver C P, *Phil. Mag.*, **24** (1971), 509.

12. Swalin R A, *Acta Metall.*, 7 (1959), 736.

Indian Journal of Pure & Applied Physics
Vol. 18, February 1980, pp. 91-93

Averaged Potential for Complex Polar Fluids

OM SINGH
Department of Physics, University of Roorkee, Roorkee
&
JAWAHAR LAL GAINDHAR
Department of Mechanical & Industrial Engineering, University of Roorkee, Roorkee

Received 14 *September* 1978; *revised received* 13 *August* 1979

The free-energy averaged potential commonly used for low density simple polar fluids has been modified for use in complex polar fluids by introducing terms for dipole-quadrupole and quadrupole-quadrupole interactions. The resulting temperature-dependent effective pair potential is used for the calculation of the second virial coefficient and viscosity of water vapour.

1. Introduction

The interaction between two complex polar molecules is quite involved and hence we may consider the total intermolecular potential as being the sum of several contributions : (i) the valence contribution associated with the short-range repulsion proportional to r^{-12} [ϕ (val)]; (ii) the London dispersion contributions which vary as r^{-6}, r^{-8}, etc. and depend only slightly on the orientations of the molecules, [$\phi^{(\text{dis})}$]; and (iii) the angle dependent electrostatic contributions due to the interactions of the molecules, [$\phi^{(\text{elect})}$]. If we assume that the valence and dispersion contributions to the intermolecular potential $\phi(r)$ are given by the *L-J* (6:12) potential,[1] and the angle dependent electrostatic contribution is due to dipole-dipole interaction, then the interaction may be represented well by the Stockmayer potential[2] which describes well the interaction only between those polar molecules which have a simple charge distribution.

2. Interaction Potential

For molecules which have complex charge distribution and have a tendency to form hydrogen bonds, it is necessary to include in the potential function, terms accounting for the interaction of higher multipoles. The most important contributions due to higher multipole interaction are the terms due to dipole-quadrupole and quadrupole-quadrupole. We may represent the interaction potential by:

$$\phi(r, w) = \phi_{L\text{-}J} - \frac{\mu^2}{r^3} g_{11}(w) + \frac{3\mu Q}{4r^4} g_{12}(w) + \frac{3Q^2}{16r^5} g_{13}(w) \quad \ldots(1)$$

where,

$$\phi_{L\text{-}J} = 4\epsilon_0 \left[\left(\frac{\sigma_0}{r} \right)^{12} - \left(\frac{\sigma_0}{r} \right)^{6} \right] \quad \ldots(2)$$

and $g_{11}(w)$, $g_{12}(w)$ and $g_{13}(w)$ are the functions of of three angles which describe the mutual orientation of two water molecules given in Eqs. (1·3-8), (1·3-9) and (1·3-10) respectively of Ref. 7, μ is the dipole moment and Q the quadrupole moment. As $Q \to 0$, Eq. (1) reduces to the familiar Stockmayer[2] potential. The term ϕ_{L-J} is the well known Lennard-Jones (6:12) potential. The parameters in *L-J* (6:12) potential σ_0 and ϵ_0 are constants characteristic of the chemical species of the colliding molecules and have dimensions of length and energy respectively.

Bae and Reed[3] take the effective potential as the canonical average, over the angular variables of the anisotropic pair potential $\phi(r, w)$. This average is given by

$$\left\langle \phi(r, T) \right\rangle = \frac{\int_w \phi(r, w) \exp\left(-\frac{(\phi\, r, w)}{k\,T} \right) dw}{\int_w \exp\left(-\frac{\phi(r, w)}{k\,T} \right) dw} \quad \ldots(3)$$

and the free-energy average is defined as

$$\left\langle\left\langle \phi(r, T) \right\rangle\right\rangle = -k\,T \ln \left[\int_w \exp\left(-\frac{\phi(r, w)}{kT} \right) dw / \int_w dw \right] \quad \ldots(4)$$

Danon and Amdur[4] made a comparative study of both the averaged potentials and used the free-energy averaged potential for calculating the properties of dilute polar gases. In both the averaging

procedures, the effective potential is spherically symmetric but temperature dependent. In discussing interactions such as $\phi(r, w)$, Onsagar[5] and Rushbrooke[6] point out that the averages of such functions over all orientations at fixed r may be regarded as energy levels which depend upon temperature. In the case of a thermodynamic property for which the density correction is limited to the first power of the density and to which a temperature-dependent pair potential is applicable, they[5,6] showed that the partition function should not be written in terms of $\langle \phi(r,T) \rangle$ but in terms of $\langle\langle \phi(r,T) \rangle\rangle$. Also $\langle\langle \phi(r,T) \rangle\rangle$ is more convergent than $\langle \phi(r,T) \rangle$. Therefore, we take the effective potential as the free-energy average over the angular variables of the anisotropic pair potential $\phi(r, w)$. If r is the internuclear separation and w is a function of three angles θ_1, θ_2 and ϕ, which specify the orientations of the multipoles, the free-energy average is given by Eq. (4).

To obtain the free-energy average of modified Stockmayer potential, Eq. (1) is introduced into Eq. (4) and the exponential term is expanded in powers of $1/kT$. If the first five terms are retained, the final result is

$$\langle\langle \phi(r,T) \rangle\rangle = 4\epsilon_0 \left[\left(\frac{\sigma_0}{r}\right)^{12} \left(1 + \frac{14\,\delta^4_{max}}{25\,T^{*3}}\right) - \left(\frac{\sigma_0}{r}\right)^6 \left(1 + \frac{\delta^2_{max}}{3\,T^*}\right) - \left(\frac{\sigma_0}{r}\right)^8 \frac{\alpha^2_{max}}{8\,T^*} + \left(\frac{\sigma_0}{r}\right)^{10} \frac{7\,\lambda^2_{max}}{80\,T^*} \right] \quad ...(5)$$

in which $\delta_{max} = \dfrac{\mu^2}{2\,\epsilon_0\,\sigma_0^3}$ (reduced dipole moment)

$\alpha_{max} = \dfrac{\mu Q}{2\,\epsilon_0\,\sigma_0^4}$ (reduced dipole-quadrupole moment)

$\lambda_{max} = \dfrac{Q^2}{2\,\epsilon_0\,\sigma_0^5}$ (reduced quadrupole moment)

and $T^* = \dfrac{kT}{\epsilon_0}$ (reduced temperature)

We can define a function applicable to complex polar molecules, which has the form of the Lennard-Jones potential

$$\phi_T = 4\,\epsilon_T \left[\left(\frac{\sigma_T}{r}\right)^{12} - \left(\frac{\sigma_T}{r}\right)^6 \right] \quad ...(6)$$

where ϵ_T and σ_T are new parameters to be related to ϵ_0 and σ_0. By equating the coefficients of r^{-12} and r^{-6} in Eqs. (5) and (6), we obtain the following relations between the two sets of parameters:

$$\sigma_T = \sigma_0 \left(\frac{\epsilon_0}{\epsilon_T}\right)^{1/12} \left(1 + \frac{14\,\delta^4_{max}}{225\,T^{*3}}\right)^{1/12} \quad ...(7)$$

$$\epsilon_T = \epsilon_0 \left(1 + \frac{14\,\delta^4_{max}}{225\,T^{*3}}\right)^{-1} \left[1 + \frac{\delta^2_{max}}{3\,T^*} + \frac{\alpha^2_{max}}{8\,T^*}\left(\frac{\sigma_0}{r}\right)^2 + \frac{7\,\lambda^2_{max}}{80\,T^*}\left(\frac{\sigma_0}{r}\right)^4 \right]^2 \quad ...(8)$$

Where ϵ_0 is the maximum energy of attraction in L-J potential, which occurs at $r = 2^{1/6}\,\sigma_0$. Therefore, Eq. (8) can be written in a more attractive way as shown below :

$$\epsilon_T = \epsilon_0 \left(1 + \frac{14\,\delta^4_{max}}{225\,T^{*3}}\right)^{-1} \left[1 + \frac{\delta^2_{max}}{3\,T^*} + \frac{\alpha^2_{max}}{10\,T^*} + \frac{7\,\lambda^2_{max}}{127\,T^*} \right]^2 \quad ...(9)$$

Now let us study the effect of the dipole-quadrupole and quadrupole-quadrupole interactions on the second virial coefficient. The expression for the second virial coefficient, obtained from the virial theorem is given by :

$$B(T) = -\frac{2\pi N}{3kT} \int_0^\infty r^3 \frac{d}{dr} \langle\langle \phi(r,T) \rangle\rangle \exp - \left(\frac{\langle\langle \phi(r,T) \rangle\rangle}{kT} \right) dr \quad ...(10)$$

Substitution of the free-energy averaged potential $\langle\langle \phi(r,T) \rangle\rangle$ [Eq. (4)] into Eq. (10) finally gives

$$B^*(T^*) = \sum_{i=0}^{\infty} \sum_{j=0}^{\infty} \sum_{k=0}^{\infty} A^{\{i+j+k-(s/n)+1\}} \times \Omega_1^{-s/n}\,\Omega_2^i\,\Omega_3^j\,\Omega_4^k \times \left[A^{-3/4}\,\Omega_1^{1/4}\,\Gamma\left(\frac{s+9}{n}\right) - \frac{6}{n} A^{-1/4}\,\Omega_1^{-1/4}\,\Omega_2\,\Gamma\left(\frac{s+3}{n}\right) - \frac{8}{n} A^{-5/n}\,\Omega_1^{-5/n}\,\Omega_3\,\Gamma\left(\frac{s+5}{n}\right) - \frac{10}{n} A^{-7/n}\,\Omega_1^{-7/n}\,\Omega_4\,\Gamma\left(\frac{s+7}{n}\right) \right] \quad ...(11)$$

Table 1—Comparison of the Values of Coefficient of Viscosity (η) for Water Vapour

T (K)	Exptl	η, 10^7 cgs units	Calc.
423·2	1440[8]	1450[8]	1516
473·2	1650	1610	1690
523·2	1860	1800	1868
573·2	2060	1990	2059
673·2	2480	2390	2419
773·2	2890	2790	2790
873.2	3310	3190	3144
973·2	3720	3580	3507
1073·2	4110	3960	3843

Table 2—Comparison of Values of Second Virial Coefficient $B(T)$ (in cc per mole) for Water Vapour

T (K)	Bae and Reed[3]	Danon and Amdur[4]	Present work	Exptl[10]
432·2	−534	−223	−283	−284
573·2	−154	−107	−114	−112
673·2	−92	−74	−75	−72

where the following reduced quantities, are used

$$r = \frac{r}{\sigma_0},\ T^* = \frac{k\,T}{\epsilon_0},\ B^*(T^*) = \frac{B(T)}{b_0},$$

$$b_0 = \frac{2\,\pi\,N\,\sigma_0^3}{3}$$

$$A = \frac{4}{T^*},\ s = 6\,i + 8\,j + 10\,k,\ n = 12,$$

$$\mu = 1{\cdot}85 \times 10^{-26}\ \text{esu}$$

$$Q = 0{\cdot}125 \times 10^{-26}\ \text{esu},\ \Omega_1 = 1 + \frac{14\,\delta^{\,4}_{\max}}{225\,T^{*3}}$$

$$\Omega_2 = 1 + \frac{\delta^2_{\max}}{3\,T^*},\ \Omega_3 = \frac{\alpha^2_{\max}}{8\,T^*},\ \Omega_4 = \frac{7\,\lambda^2_{\max}}{80\,T^*}$$

3. Results and Discussion

The force parameters of the free-energy averaged pair potential are obtained from experimental values of viscosities of polar gases. The procedure is essentially that given by Hirschfelder *et al.*[7] We find for water vapour, $\sigma_0 = 2{\cdot}727$ Å and $\epsilon_0/k = 510$K for the potential in Eq. (5).

Now it is important to see if these force parameters adequately reproduce the experimental values over full ranges of temperatures. Accordingly these force parameters have been used to recalculate the experimental viscosities and it is found that calculated and the experimental values are in good agreement as shown in Table 1.

The parameters, determined from the viscosity data have been used to calculate the second virial coefficient for water vapour. From the results, shown in Table 2, it is clear that our results show an improvement over Danon and Amdur[4] results and are at the same time in very good agreement with the experimental data. It should also be emphasized here that the derived parameters are certainly more reliable than those of others because the dipole-quadrupole and quadrupole-quadrupole interactions are added in the Stockmayer potential.

This potential is yet to be tested for other complex polar gases because experimental data on quadrupole moments are not available at present for these gases.

Acknowledgement

The authors express their sincere thanks to Dr N C Varshneya, Dr Narsingh Dass for helpful and stimulating discussions and Dr Bani Singh in computing the results. One of them (OS) is also highly thankful to the CSIR, New Delhi, for financial assistance in form of an assignment in the CSIR scientist pool.

References

1. Lennard-Jones J E & Devonshire A F, *Proc. R. Soc. Lond.*, A106 (1924), 463.
2. Stockmayer W H, *J. chem. Phys.*, 9 (1941), 398.
3. Bae J H & Reed T M, *Ind. Eng. Chem. Fundamentals*, 6 (1967), 67.
4. Danon F & Amdur I J, *J. chem. Phys.*, 50 (1969), 4718.
5. Onsagar L, *Chem. Rev.*, 13 (1933), 73.
6. Rushbrooke G S, *Trans. Faraday Soc.*, 36 (1940), 1055.
7. Hirschfelder J O, Curtiss C F & Bird R B, *Molecular theory of gases and liquids* (John Wiley, New York), 1954.
8. Shifrin A S, *Teploenergetika*, 6 (1959), 22.
9. Bonilla C F, Wangand S J & Weiner H, *Trans. Amer. Soc. Mech. Engrs*, 78 (1956), 1285.
10. Rowlinson J S, *Trnas. Faraday Soc.*, 45 (1949), 974.

Indian Journal of Pure & Applied Physics
Vol. 18, February 1980, pp. 94-106

Force Field Studies on α, β-Unsaturated Amides I : N, N-Dimethyl Acrylamide

G Ramana Rao & K Venkata Ramiah*

Department of Physics, Kakatiya University, Warangal 506 009

Received 5 *December* 1978; *revised received* 16 *April* 1979

The infrared spectrum in the range 4000-600 cm^{-1} and the laser Raman spectrum in the range 3300-150 cm^{-1} of N, N-dimethyl acrylamide have been recorded. The vibrational frequencies are used to obtain reasonable sets of force constants of valence type, of modified Urey-Bradley type and of Urey-Bradley type by damped least squares technique. The potential energy distributions in both internal force constants and symmetry coordinates are computed. A zero-order calculation is made for some of the deuterated species of N, N-dimethyl acrylamide. The vibrational assignment of the frequencies of N, N-dimethyl acrylamide and its deuterated species is attempted. The nature of the absorption bands is discussed in relation to the mixing of vibrational modes. A quantitative method of classifying vibrational frequencies is proposed.

1. Introduction

The spectral investigation of tertiary amides and related systems has been the subject matter of several research papers in the recent times. Venkata Ramiah and coworkers recorded the infrared and Raman spectra of N, N-dimethyl formamide (DMF),[1] N, N-dimethyl acetamide (DMA),[1] N, N-dimethyl propionamide (DPA),[2] N, N-dimethyl butyramide (DBA),[3] N, N-dimethyl thioformamide (DMTF)[4] and N, N-dimethyl thioacetamide (DMTA)[4] and obtained a general valence force field (GVFF) in the case of each of the above systems, except for DBA, by treating the methyl and ethyl groups as point masses. Durgaprasad *et al.*[5] recorded the infrared spectra of DMF, DMF-^{15}N, DMF-d_7 and DMTF and explained their normal vibrations by using Urey-Bradley force field (UBFF), modified Urey-Bradley force field (MUBFF), and symmetrized valence force field (SVFF). They made an approximate calculation in the case of N, N-dimethyl selenoformamide (DMSF) by using the force fields of DMTF. Rao and collaborators studied the normal vibrations of DMA using UBFF and MUBFF,[6] whereas Lagrange and coworkers explained the normal vibrations of DMA, DMA-d_3, DMA-d_6 and DMA-d_9 by using GVFF.[7,8] Anthoni *et al.*[9] assigned the fundamental vibrations of DMSF, DMSF-d_6, and DMSF-d_7 using GVFF. In this paper, we choose to report the results of our study on N, N-dimethyl acrylamide (DMAC) which is a continuation of our work on acrylamide[10] and N-methyl acrylamide.[11] The objectives of the normal coordinate treatment of this molecule are as follows.

(i) To record the infrared and laser Raman spectra of DMAC and to make initial assignments,
(ii) To get a reasonable set of force constants of (a) GVFF (b) MUBFF and (c) UBFF,
(iii) To make a zero-order calculation for some deuterated species of the molecule,
(iv) To estimate the amount of mixing of vibrational modes in order to clarify the nature of the absorption bands and classify them, and
(v) To check the initial assignments leading to the vibrational assignments.

2. Experimental Procedure

The infrared spectrum of DMAC was recorded with Perkin-Elmer double beam spectrophotometers (Models 21 and 337) using a thin film of unknown thickness in the region 4000-600 cm^{-1} and using NaCl optics. The Raman spectrum was measured with spex Ramalog and argon ion laser source using 4880 Å as the exciting radiation in the region 3300-150 cm^{-1}. The spectra are shown in Figs. 1 and 2.

3. Normal Coordinate Treatment

The method of Wilson[12] was used to compute (a) GVFF constants, (b) MUBFF constants of the type used by Jakes and Schneider for N-methyl acetamide[13] and (c) UBFF constants as improved by Shimanouchi and his group.[14] It was assumed that (i) the molecular symmetry of DMAC is C_s with C—C_α bond trans to the C—N bond, and (ii) two of the hydrogens of each CH_3 group are lying out of the plane of molecular symmetry, one above and the other below the plane. The assumption of the C_s structure may be justified from the crystallographic data for a number of long chain *n*-fatty acid amides.[15-18] It was shown that the N.

*Present address : Department of Physics, Osmania University, Hyderabad-7

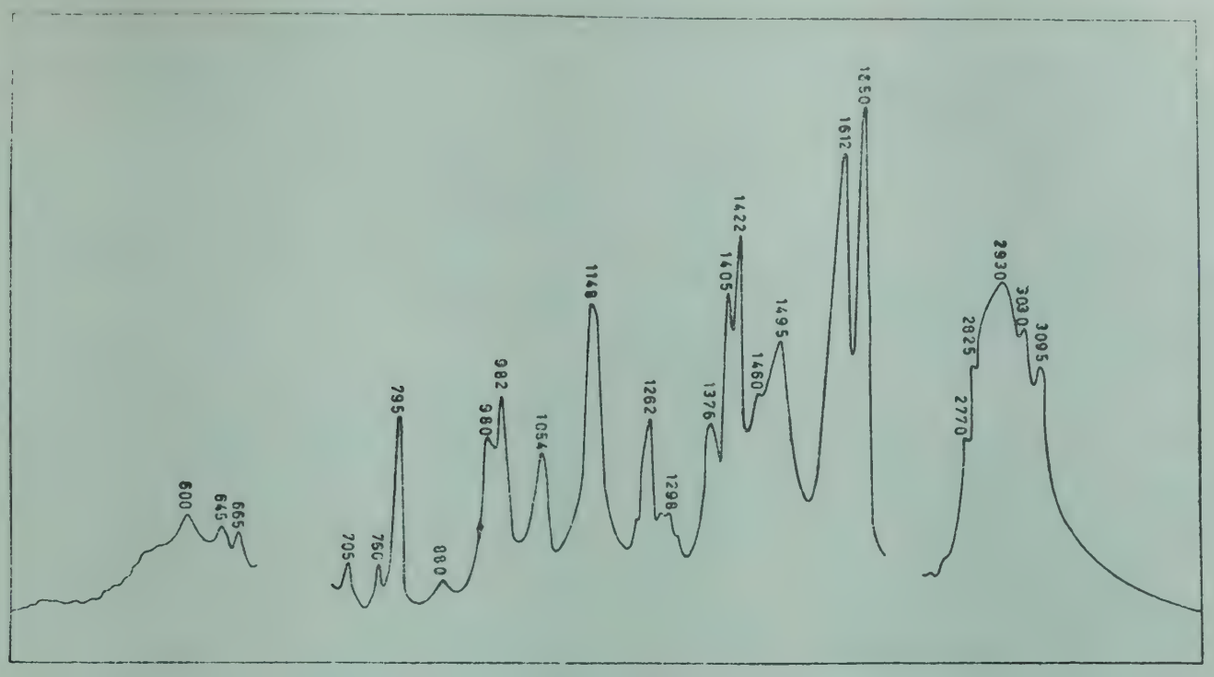

Fig. 1—Infrared spectrum of N, N-dimethyl acrylamide

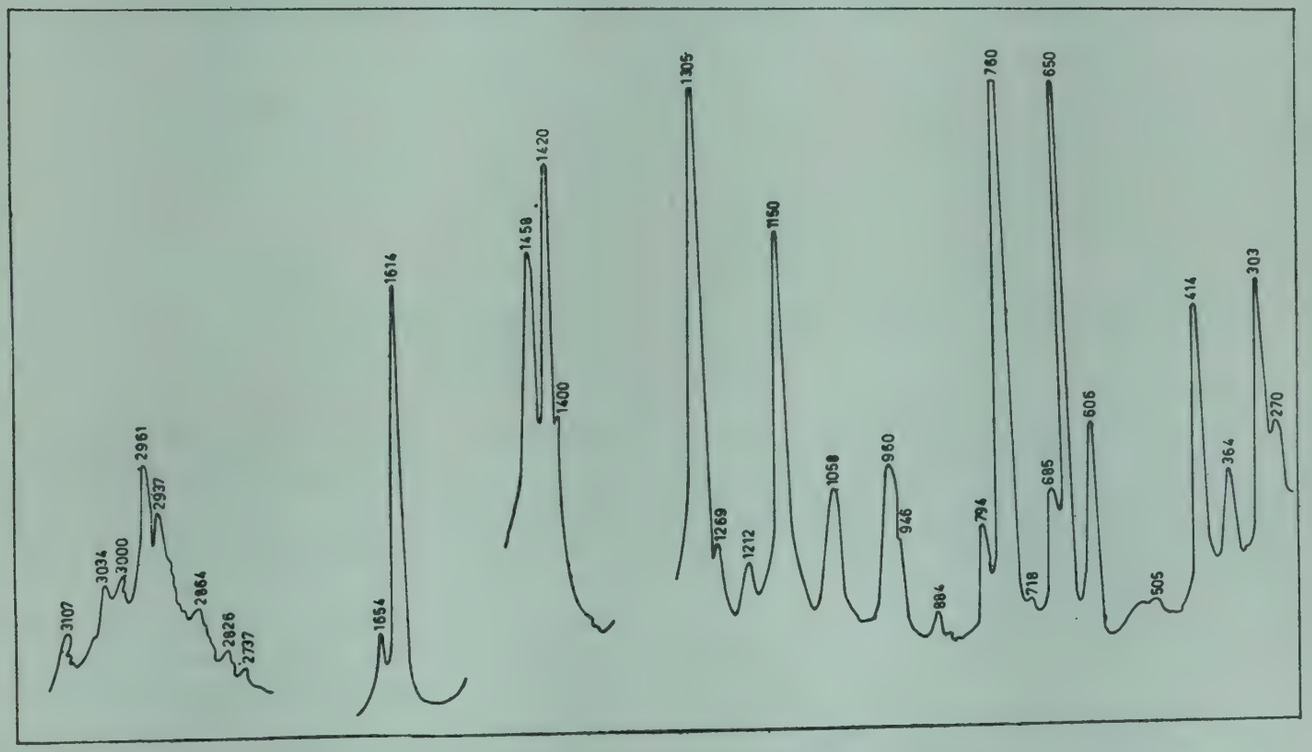

Fig. 2—Laser Raman spectrum of N, N-dimethyl acrylamide

C, C_α and C_β atoms of CH_3 $(CH_2)_n$ $CONH_2$ (n=8 and 12) are nearly coplanar and cell dimension c_0 increases while a_0 and b_0 remain almost constant in going through the series $CH_3(CH_2)_n CONH_2$ (n=2 to 14). The ethelenic double bond also takes part in giving a planar structure to the molecule. In the C_s model, the 42 fundamental vibrations fall into 27 in-plane vibrations of A' species and 15 out-of-plane vibrations of A'' species. In this paper, A' species were treated completely whereas the A'' species were treated only partially. The structure of the molecule is shown in Fig. 3.

The bond lengths used are C—N = 1·315 Å; C=O = 1·243 Å; C—C = 1·47 Å; C=C = 1·137 Å; C—H (ethelene) = 1·07 Å; N—C = 1·47 Å and C—H (methyl) = 1·09 Å. These values were taken from closely related systems. The angles around the methyl carbon atom were assumed to be

Table 1—Symmetry Coordinates for N, N-Dimethyl Acrylamide*

S_n	Internal coordinates involved** A′ species	Description†
S_1	Δi	ν (C—H)
S_2	$\Delta j - \Delta k$	ν_{as} (CH_2)
S_3	$\Delta j + \Delta k$	ν_s (CH_2)
S_4	$2\Delta l - \Delta m - \Delta n + 2\Delta p - \Delta q - \Delta t$	ν_{as} (CH_3)$_2$
S_5	$2\Delta l - \Delta m - \Delta n - 2\Delta p + \Delta q - \Delta t$	ν_{as} (CH_3)$_2$
S_6	$\Delta l + \Delta m + \Delta n + \Delta p + \Delta q + \Delta t$	ν_s (CH_3)$_2$
S_7	$\Delta l + \Delta m + \Delta n - \Delta p - \Delta q - \Delta t$	ν_s (CH_3)$_2$
S_8	$2\Delta mn - \Delta ml - \Delta nl + 2\Delta qt - \Delta pq - \Delta pt$	δ_{as} (CH_3)$_2$
S_9	$2\Delta mn - \Delta ml - \Delta nl - 2\Delta qt + \Delta pq + \Delta pt$	δ_{as} (CH_3)$_2$
S_{10}	$\Delta ml + \Delta mn + \Delta nl - \Delta dl - \Delta dm - \Delta dn + \Delta pt + \Delta qt + \Delta pq - \Delta pe - \Delta te - \Delta qe$	δ_s (CH_3)$_2$
S_{11}	$\Delta ml + \Delta mn + \Delta nl - \Delta dl - \Delta dm - \Delta dn - \Delta pt - \Delta qt - \Delta pq + \Delta pe + \Delta te + \Delta qe$	δ_s (CH_3)$_2$
S_{12}	$2\Delta dl - \Delta dm - \Delta dn + 2\Delta pe - \Delta qe - \Delta te$	γ (CH_3)$_2$
S_{13}	$2\Delta dl - \Delta dm - \Delta dn - 2\Delta pe + \Delta qe + \Delta te$	γ (CH_3)$_2$
S_{14}	$\Delta d - \Delta e$	$\nu_{as}\left(N\begin{smallmatrix}CH_3\\CH_3\end{smallmatrix}\right)$
S_{15}	$\Delta d + \Delta e$	$\nu_s\left(N\begin{smallmatrix}CH_3\\CH_3\end{smallmatrix}\right)$
S_{16}	Δb	ν (C=O)
S_{17}	Δc	ν (C—C)
S_{18}	Δh	ν (C=C)
S_{19}	$2\Delta de - \Delta ad - \Delta ae$	$\delta\left(N\begin{smallmatrix}CH_3\\CH_3\end{smallmatrix}\right)$
S_{20}	$2\Delta jk - \Delta hj - \Delta hk$	δ (CH_2)
S_{21}	$\Delta ci - \Delta hi$	δ (C—H)
S_{22}	Δa	ν (C—N)
S_{23}	$\Delta ad - \Delta ae$	$\gamma\left(N\begin{smallmatrix}CH_3\\CH_3\end{smallmatrix}\right)$
S_{24}	$\Delta hj - \Delta hk$	γ (CH_2)
S_{25}	$2\Delta ab - \Delta bc - \Delta ac$	δ (O=C—N)
S_{26}	$2\Delta ch - \Delta ci - \Delta hi$	δ (C—C=C)
S_{27}	$\Delta bc - \Delta ac$	δ (C—C)
S_{28}	$\Delta hj + \Delta jk + \Delta hk$	Redundant
S_{29}	$\Delta ch + \Delta ci + \Delta hi$	Redundant
S_{30}	$\Delta ab + \Delta bc + \Delta ac$	Redundant
S_{31}	$\Delta ad + \Delta de + \Delta ae$	Redundant
S_{32}	$\Delta dl + \Delta dm + \Delta dn + \Delta lm + \Delta nl + \Delta mn + \Delta ep + \Delta eq + \Delta et + \Delta pq + \Delta pt + \Delta qt$	Redundant
S_{33}	$\Delta dl + \Delta dm + \Delta dn + \Delta lm + \Delta nl + \Delta mn - \Delta ep - \Delta eq - \Delta et - \Delta pq - \Delta pt - \Delta qt$	Redundant
	A″ species††	
S_{34}	$\Delta m - \Delta n + \Delta q - \Delta t$	ν_{as} (CH_3)$_2$
S_{35}	$\Delta m - \Delta n - \Delta q + \Delta t$	ν_{as} (CH_3)$_2$
S_{36}	$\Delta lm - \Delta nl + \Delta pt - \Delta pq$	δ_{as} (CH_3)$_2$
S_{37}	$\Delta lm - \Delta nl - \Delta pt + \Delta pq$	δ_{as} (CH_3)$_2$
S_{38}	$\Delta dm - \Delta dn + \Delta et - eq$	γ (CH_3)$_2$
S_{39}	$\Delta dm - \Delta dn - \Delta et + \Delta eq$	γ (CH_3)$_2$

*Symmetry coordinates are not normalized.

**+ve and −ve signs identify an increase or decrease of the bond length or bond angle during the vibrations.

†ν, δ and γ denote stretch, deformation and rocking respectively; as (anti-symmetric) and s (symmetric) refer to the local site symmetry, not to the symmetry plane of N, N-dimethyl acrylamide.

††The symmetry coordinates of those A'' species which are not included in the calculations are not given.

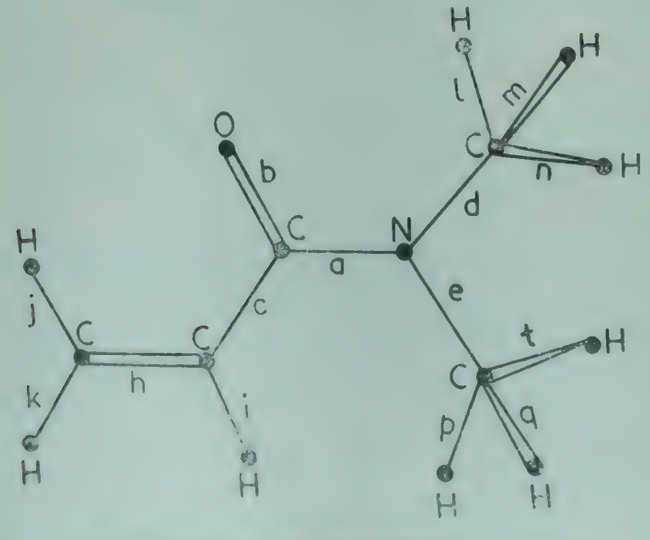

Fig. 3—Structure of N, N-dimethyl acrylamide

tetrahedral, all other angles were taken to be equal to 120° each. The ortho-normal set of symmetry coordinates used in the calculations are given in Table 1.

The computing procedure is the same as that used for acrylamides[10] and N-methyl thiopropionamides.[19] The initial set of GVFF constants were obtained by transferring them from acrylamides,[10] DPA[2] and N-methyl thiopropionamides[19] whereas the initial constants of MUBFF and UBFF were taken from those of acrylamides,[20] DMA,[6] and propionamide.[21] 32 Frequencies of DMAC were used to refine 24 of 31 GVFF constants, 29 of 36 MUBFF constants and 27 of 33 UBFF constants by damped least squares method.[22,23] Several of the interaction constants and non-bonded repulsion constants were

held fixed during the process of refinement. To avoid the difficulties that arise because of correlation of force constants due to the usage of redundant coordinates, one of the bending force constants around the nitrogen atom and one around the α-carbon atom were held fixed during refinement, as suggested by Jones *et al.*[24,25] The final sets of these constants are shown in Table 2.

4. Results and Discussion

The observed and calculated frequencies, potential energy distributions (PED) in internal force constants and symmetry coordinates, using valence force field for N, N-dimethyl acrylamide are shown in Table 3 along with the type of mode and nature of vibration.

PED in internal coordinates is obtained by using the formula $[\Lambda^{-1}(JZ)\phi] \times 100$ and that in symmetry coordinates by using the formula $(F_{kl} L_{ki} L_{li}/\lambda_i) \times 100$. Contributions below 10% are not shown.

The actual assignments of the vibrational frequencies for the molecule are shown in Table 4.

The results of the zero-order calculations on CD_2 CDCON $(CH_3)_2$ (i.e. DMAC-d_3), CH_2 CHCON $(CD_3)_2$ (i.e. DMAC-d_6), and CD_2 CDCON $(CD_3)_2$ (i.e. DMAC-d_9) using GVFF are presented in Table 5.

4.1 Final Sets of Force Constants

The normal coordinate analysis of DMAC was carried out using three force fields namely GVFF, MUBFF and UBFF in order to find the PED's that are characteristic of the force fields so as to avoid misassignment of frequencies due to any possible inadequacy of force constants of any particular type.

The calculated and observed frequencies shown in Table 3 are in good agreement. The force constants shown in Table 2 are comparable with those of the related molecules. These observations indicate that the constants obtained are reasonable. The interaction force constant f_a^b of GVFF is positive and large as in the case of amides[10,21,26] indicating the presence of delocalized electrons[27,28] in the peptide linkage.

The MUBFF consists of GVFF for CH_2—CH— and CH_3 groups and UBFF for the amide skeleton Table 2 shows two bond angle interaction constants f_c^{bc} and f_c^{ac}. This type of interaction is also provided by the corresponding non-bonded repulsions. There is justification for the duplication of these interaction constants because (i) In the zero-order calculation of acrylamides[20] using MUBFF it was found that the introduction of these constants improved the frequency fit enormously and without them ν (C=C) was 150 cm^{-1} away from its observed value and (ii) UBFF non-bonded repulsions are inadequate to represent the actual interaction forces in a molecule.[29-31]

The final sets of force constants were used to calculate the vibrational frequencies of DMAC-d_3, DMAC-d_6, DMAC-d_9. These frequencies are reasonable when compared with their counter parts in related systems.

4.2 Classification of Normal Modes

To classify the normal modes in internal force constants, we have followed the method suggested by Jones *et al.*[24] and extended it to symmetry coordinates. According to this method, a normal mode is said to be a group frequency (GF) if it gets 66% or more of PED from a single force constant. It is said to be a zone frequency (ZF) if the sum of PED contributions from any two of the force constants is 66% or more. It is said to be a delocalized frequency (DF) if the PED contributions from each of the force constants is less than 33%. In the case of DMAC, there are certain frequencies which will not fit into the above scheme. In these cases, the PED contribution from one of the force constants is greater than or equal to 33% and yet the sum of PEDs from any two of the force constants is less than 66%. We have named such frequencies as delocalized zone frequencies (DZF) as their description takes a middle course between ZFs and DFs.

For the classification of normal modes using PED in symmetry coordinates, we have left the above conditions unchanged and altered the nomanclature. The normal modes satisfying the conditions of GF, ZF, DZF and DF in symmetry coordinates are called pure frequency (PF), selectively mixing frequency (SMF), delocalized mixed frequency (DMF) and mixed frequency (MF) respectively.

The classification shown in Tables 3 and 5 are based on the above conditions. From Tables 3 and 5 it is clear that a GF turns out to be a PF; a ZF exhibits selective mixing; a DZF becomes a DMF and a DF shows a mixed nature with a few exceptions. This scheme, eventually, tells about the amount of mixing and clearly shows the nature of the absorption bands.

4.3 Vibrational Assignments

The vibrational assignments are guided by

(i) assignment of corresponding bands in related systems,

Table 2—Force Constants of N, N-Dimethyl Acrylamide

Force constant	Type	Value* GVFF	MUBFF	UBFF
		Direct constant Stretch		
ϕ_1	f_i	4·308	4·309	3·836
ϕ_2	$f_j=f_k$	5·099	5·098	4·695
ϕ_3	$f_l=f_m=f_n=f_p=f_q=f_t$	4·789†	4·790†	4·348‡
ϕ_4	$f_d=f_e$	4·291**	4·045 (UB)	2·710
ϕ_5	f_a	6·278**	4·980 (UB)	5·057
ϕ_6	f_b	8·448	7·109 (UB)	8·078
ϕ_7	f_c	6·540	6·130	4·301
ϕ_8	f_h	7·712	7·611	7·221
		Bend		
ϕ_9	$f_{hj}=f_{hk}$	0·845	0·968	0·222††
ϕ_{10}	f_{jk}	0·170	0·051	0·238††
ϕ_{11}	f_{ch}	1·38	1·38	0·607††
ϕ_{12}	f_{hi}	0·419	0·228	0·294††
ϕ_{13}	f_{ci}	0·348	0·610	0·00177††
ϕ_{14}	f_{bc}	0·334	0·220 (UB)	0·0267
ϕ_{15}	f_{ac}	1·044	0·108 (UB)	0·280
ϕ_{16}	f_{ab}	1·360	0·633 (UB)	0·304
ϕ_{17}	$f_{ad}=f_{ae}$	1·140**	0·954 (UB)	0·536
ϕ_{18}	f_{de}	1·653**	1·512 (UB)	0·626
ϕ_{19}	$f_{dl}=f_{dm}=f_{dn}=f_{ep}=f_{eq}=f_{et}$	0·718†	0·768	0·218
ϕ_{20}	$f_{lm}=f_{ln}=f_{mn}=f_{pq}=f_{pt}=f_{qt}$	0·526†	0·526	0·410

Force constant	Type	Value* GVFF	MUBFF	UBFF
		Interaction constant/Non-bonded repulsion constants		
ϕ_{21}	f_a^b	1·621	1·496 (UB)	1·407
ϕ_{22}	f_b^e	1·434	0·254 (UB)	0·5
ϕ_{23}	f_c^a	0·825	0·825 (UB)	0·5
ϕ_{24}	f_c^h	0·445	0·445	0·497
ϕ_{25}	f_c^{bc}/f_c^i	1·350	1·350	0·290
ϕ_{26}	f_c^{ac}/f_h^i	0·373	0·373	0·594
ϕ_{27}	$f_d^{dl}\ldots=f_e^{ep}/f_d^l\ldots$	0·112†	0·371	0·759
ϕ_{28}	$f_{dl}^{dm}\ldots=f_{ep}^{eq}/f_h^j\ldots$	−0·0776†	−0·324	0·619
ϕ_{29}	f_j^k	0·0875	0·0902	0·086
ϕ_{30}	f_d^e	−0·370	0·0015 (UB)	0·30
ϕ_{31}	$f_l^m=\ldots f_p^q$	0·0752	0·0761	0·0769
ϕ_{32}	$f_a^d=f_a^e$	—	0·2557 (UB)	0·42
ϕ_{33}	$f_{ad}^{dm}\ldots$	—	0·06	$F'=-F/10$
ϕ_{34}	$f_{de}^{dl}\ldots$	—	0·0470	Intramolecular tension
ϕ_{35}	$f_{de}^{lm}\ldots$	—	0 00536	$=-0·0221$ mdyne Å/rad²
ϕ_{36}	$f_{ad}^{dl}\ldots$	—	0·2078 $F'=-F/10$	

f_i The stretching force constant for ith bond.

f_{ij} The bending constant for the angle between ith and jth bonds.

f_{ji} Bond-bond interaction constant between ith and jth bonds in case it is a valence force constant. Non-bonded interaction constant between the atoms at the ends of ith and jth bonds in case it is a Urey-Bradley constant

f_i^{jk} Bond angle interaction constant between ith bond and jkth angle

* Units of the force constants : GVFF and MUBFF are in mdyne/Å, mdyne/rad, and mdyne Å/rad² and all the UBFF constants are in mdyne/Å

** Initial value is taken from N, N-dimethyl propionamide

† Initial value is taken from N-methyl thio propionamide

‡ Initial value is taken from propionamide

†† Initial value is taken from acrylamide
Other GVFF constants are taken from acrylamide and those of UBFF and MUBFF are taken from N, N-dimethyl acetamide

Force constant numbers 11, 21 to 26 of GVFF; 11, 14, 24 to 26, 33, 36 of MUBFF; 15, 22, 23, 28, 30 and 32 of UBFF are fixed throughout the refinement process

Table 3—Observed and Calculated Frequencies (in cm^{-1}) and PED of N, N-Dimethyl Acrylamide

Obs.	Calc.	PED in Internal Force Constants	Type of mode GVFF*	PED in symmetry coordinates	Nature of mode
			A' species		
2825	2825	$98f_i$	GF	98 S_1	PF
3095	3095	$100f_j$	GF	99 S_2	PF
3030	3030	$97f_j$	GF	99 S_3	PE
3000	2986	$100f_l$	GF	99 S_4	PF
3000	2980	$100f_l$	GF	99 S_5	PF
2930	2930	$97f_l$	GF	100 S_6	PF
2930	2931	$97f_l$	GF	100 S_7	PF
1460	1451	$80f_{lm}$	GF	75 S_8	PF
1460	1465	$73f_{lm}$, $16f_{dl}$	GF	68 S_9, 13 S_{13}	PF
1376	1372	$59f_{dl}$, $44f_{lm}$	ZF	85 S_{10}	PF
1405	1404	$16f_b$, $31f_{hj}$, $19f_{dl}$, $15f_{lm}$	DF	17 S_{20}, 22 S_{11}, 16 S_{16}, 19 S_{24}	MF
1495	1514	$12f_d$, $42f_a$, $23f_{dl}$, $12f_{lm}$	DZF	10 S_8, 22 S_{12}, 10 S_{15}, 10 S_{19}, 39 S_{22}	DMF
1054	1053	$23f_{hi}$, $15f_{ci}$, $28f_{dl}$	DF	22 S_{13}, 37 S_{21}	DMF
1148	1118	$13f_b$, $22f_c$, $10f_h$, $14f_{hj}$, $39f_{dl}$	DF	26 S_{12}, 18 S_{17}, 11 S_{18}, 12 S_{22}, 11 S_{24}	MF
606	577	$40f_d$, $17f_{ab}$, $13f_{ad}$, $11f_{de}$	DZF	29 S_{15}, 15 S_{19}, 22 S_{25}	MF
982	981	$10f_b$, $26f_c$, $11f_{hi}$, $13f_{ci}$, $14f_{dl}$	DF	15 S_{12}, 14 S_{16}, 30 S_{17}, 24 S_{21}	MF
303	306	$11f_c$, $17f_{bc}$, $44f_{ab}$, $37f_{ad}$	ZF	36 S_{23}, 42 S_{25}, 10 S_{27}	SMF
1262	1259	$18f_d$, $19f_b$, $28f_{dl}$, $16f_{lm}$	DF	29 S_{11}, 10 S_{13}, 21 S_{14}, 18 S_{16}	MF
760	764	$50f_d$, $12f_{ch}$, $11f_{ab}$	DZF	45 S_{15}, 10 S_{25}, 14 S_{26}	DMF
1298	1298	$14f_h$, $55f_{hj}$, $11f_{ch}$	ZF	14 S_{18}, 38 S_{20}, 27 S_{24}	DMF
1612	1628	$22f_c$, $50f_h$, $18f_{hj}$	ZF	17 S_{17}, 50 S_{18}, 20 S_{20}	SMF
414	395	$12f_a$, $42f_{ch}$, $16f_{de}$, $10f_e$	DZF	22 S_{19}, 13 S_{22}, 47 S_{26}	SMF
505	513	$15f_d$, $11f_{ac}$, $21f_{ad}$, $23f_{de}$	DF	10 S_{14}, 31 S_{19}, 13 S_{23}	MF
1422	1439	$18f_d$, $19f_{hj}$, $21f_{dl}$, $32f_{lm}$	DF	15 S_9, 30 S_{11}, 17 S_{14}. 14 S_{24}	MF
1650	1653	$43f_b$, $11f_c$, $10f_{ac}$, $10f_{ad}$	DZF	37 S_{16}, 10 S_{17}, 10 S_{23}	DMF
0·0	180	$19f_{bc}$, $57f_{ac}$, $20f_{ad}$	ZF	20 S_{22}, 10 S_{26}, 69 S_{27}	PF
1054	1046	$12f_d$, $52f_{dl}$	DZF	11 S_{12}, 46 S_{13}, 13 S_{14}, 11 S_{21}	DMF
			A'' species		
2961	2978	$101f_l$	GF	100 S_{34}	PF
2961	2978	$101f_l$	GF	100 S_{35}	PF
1460	1458	$11f_{dl}$, $88f_{lm}$	GF	85 S_{36}, 12 S_{38}	PF
1460	1464	$14f_{dl}$, $85f_{lm}$	GF	80 S_{37}, 15 S_{39}	PF
1054	1076	$79f_{dl}$, $12f_{lm}$	GF	15 S_{36}, 90 S_{38}	PF
1148	1148	$76f_{dl}$, $15f_{lm}$	GF	10 S_{37}, 85 S_{39}	PF

* Similar results were obtained using MUBFF and UBFF

Table 4—Vibrational Assignments of N, N-Dimethyl Acrylamide

Observed Frequency (cm^{-1})		Vibrational assignment
I R	Raman	
		A' Species
2825	2826	ν (C−H)
3095	3107	ν_{as} (CH_2)
3030	3034	ν_s (CH_2)
—	3000	ν_{as} $(CH_3)_2$
—	3000	ν_{as} $(CH_3)_2$
2930	2937	ν_s $(CH_3)_2$
2930	2937	ν_s $(CH_3)_2$
1460	1458	ν_{as} $(CH_3)_2$
1460	1458	δ_{as} $(CH_3)_2$
1376	—	δ_s $(CH_3)_2$+ν (C—N)*
1405	1400	δ_s $(CH_3)_2$*
1495	—	ν (C−N)+γ $(CH_3)_2$
1054	1058	δ (C—H)+γ $(CH_3)_2$
1148	1150	γ $(CH_3)_2$+ν (C—C)+ν (C=C)
606	600	δ (O=C−N)+ν_s 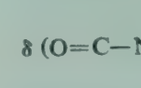
982	960	ν (C—C)+ν (C=O)+ γ $(CH_3)_2$
—	303	γ 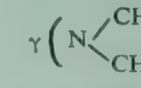 + δ (O=C—N)
1262	1269	ν_{as} 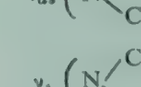 + γ $(CH_3)_2$**
760	760	ν_s 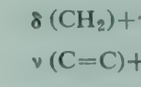 + γ $(CH_3)_2$*
1298	1305	δ (CH_2)+γ(CH_2)
1612	1614	ν (C=C)+δ (CH_2)
Observed Frequancy (cm^{-1})		Vibrational assignment
I R	Raman	
		A' Species
—	414	δ (C—C=C)+δ 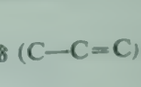
—	505	δ 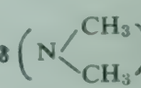 +γ
1422	1420	γ (CH_2)+δ_s $(CH_3)_2$
1650	1654	ν (C=O)+ν (C—C)+γ (CH_2)
180††	180††	δ (C—C)+γ 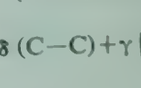
1054	1058	γ $(CH_3)_2$+ν_{as} 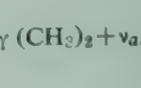
		A" species
—	2961	ν_{as} $(CH_3)_2$
—	2961	ν_{as} $(CH_3)_2$
1460	1458	δ_{as} $(CH_3)_2$
1460	1458	δ_{as} $(CH_3)_2$
1054	1058	γ $(CH_3)_2$
1148	1150	γ $(CH_3)_2$
645	650	π (C=O)†
—	270	τ (C—N)†
—	364	ω 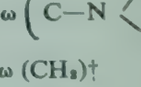
960	960	ω (CH_2)†
1054	1058	τ (CH_2)†
—	—	τ (C−C)†
—	—	τ $(CH_3)_2$†
—	—	τ $(CH_3)_2$†

* Assigned on the basis of MUBFF ** Assigned on the basis of UBFF
† Tentative assignment †† Calculated value
— Not observed

(ii) infrared and Raman intensities (qualitative),
(iii) isotopic shifts (calculated), and
(iv) PED given in Tables 3 and 5.

The assignments of frequencies of DMAC, in addition, are aided by the persistent contributions in different force fields.

4.3.1 *Frequencies of methyl groups*—The number of fundamental stretching vibrations of the methyl groups in the dimethylamino group usually exceeds the number of bands which reasonably can be attributed to this origin.[32] However, according to the results of the normal coordinate analysis on DMAC, two asymmetric modes are calculated to be within a narrow interval of 6 cm^{-1} while the other two are coincident at 2978 cm^{-1} according to GVFF calculations. In the same way, the two fundamentals due to symmetric stretching are almost coincident near 2930 cm^{-1}. The results of MUBFF and UBFF follow the same general pattern as stated above. In DMAC-d_3, the calculated values of corresponding modes are same as that in DMAC. In DMAC-d_6 the four asymmetric modes are displaced to the region 2222-2239 cm^{-1}, while the symmetric modes are calculated at 2111-2116 cm^{-1}, which have the same values in DMAC-d_9.

The assignments given in Tables 4 and 5 follow this pattern. Thus the strong band in both infrared (2930 cm^{-1}) and the Raman (2937 cm^{-1}) spectra of

Table 5—PED and Vibrational Assignment of Deuterated N, N-Dimethyl Acrylamides

Calc. frequency (cm^{-1})	PED in internal force constants	Type of mode	PED in symmetry coordinates	Nature of mode	Vibrational assignment
			CD_2 CD CO N C_2 H_6 *A′* species		
2116	85 f_i	GF	85 S_1	PF	ν (C—H)
2331	97 f_j	GF	95 S_2	PF	ν_{as} (CH_2)
2227	86 f_j	GF	89 S_3	PF	ν_s (CH_2)
2985	101 f_l	GF	99 S_4	PF	ν_{as} $(CH_3)_2$
2980	101 f_l	GF	99 S_5	PF	ν_{as} $(CH_3)_2$
2930	97 f_l	GF	100 S_6	PF	ν_s $(CH_3)_2$
2931	97 f_l	GF	100 S_7	PF	ν_s $(CH_3)_2$
1450	79 f_{lm}	GF	72 S_8	PF	δ_{as} $(CH_3)_2$
1463	14 f_{dl}, 80 f_{lm}	GF	75 S_9, 13 S_{13}	PF	δ_{as} $(CH_3)_2$
1373	61 f_{dl}, 45 f_{lm}	ZF	90 S_{10}	PF	δ_s $(CH_3)_2$
1426	23 f_d, 39 f_{dl}, 38 f_{lm}	ZF	54 S_{11}, 21 S_{14}	SMF	δ_s $(CH_3)_2$+γ (CH_2)
1510	15 f_d, 25 f_a, 22 f_{dl}, 13 f_{lm}	DZF	11 S_8, 22 S_{12}, 34 S_{22}	DMF	γ $(CH_3)_2$=ν (C—N)
760	13 f_{hj}, 38 f_{hi}, 26 f_{ci}	DZF	63 S_{21}, 10 S_{24}	DMF	δ (C—H)
1084	16 f_a, 12 f_{hj}, 46 f_{dl}	DZF	42 S_{12}, 16 S_{22}, 12 S_{24}	DMF	γ $(CH_3)_2$+ν (C—N)+γ (CH_2)
566	34 f_d, 18 f_{ab}, 13 f_{ad}, 15 f_{de}	DZF	25 S_{15}, 20 S_{19}, 24 S_{25}	MF	ν_s +δ 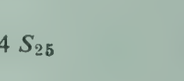 +δ (O=C –N)
890	13 f_d, 19 f_c, 36 f_{hj}	DZF	21 S_{17}, 15 S_{20}, 26 S_{24}	MF	ν (C—C)+ δ (CH_2)+γ (CH_2)
305	15 f_{bc}, 44 f_{ab}, 38 f_{ad}	ZF	47 S_{23}, 43 S_{25}	SMF	γ +δ (O=C—N)
1263	20 f_d, 12 f_b, 33 f_{dl}, 19 f_{lm}	DZF	32 S_{11}, 11 S_{13}, 23 S_{14}, 12 S_{16}	DMF	δ_s $(CH_3)_2$+ν_{as} 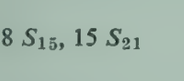
730	41 f_d, 10f_{ci}	DZF	38 S_{15}, 15 S_{21}	DMF	ν_s 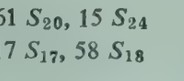 + δ (C—H)
987	59 f_{hj}, 18 f_{jk}	ZF	61 S_{20}, 15 S_{24}	SMF	δ (CH_2)+γ (CH_2)
1543	23 f_c, 58f_h	ZF	17 S_{17}, 58 S_{18}	SMF	ν (C—C)+ ν(C=C)
368	12f_a, 10 f_c, 42 f_{eh}, 13 f_{de}	DZF	10 S_{17}, 17 S_{19}, 13 S_{22}, 48 S_{26}	DMF	ν (C—C)+δ 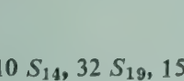 +ν (C—N) + δ (C—C=C)
506	13 f_d, 23 f_{ad}, 23 f_{de}	DF	10 S_{14}, 32 S_{19}, 15 S_{23}	MF	ν_{as} 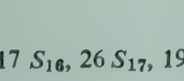 + δ 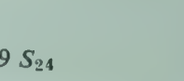 + γ
1234	15 f_b, 24 f_c, 25 f_{hj}	DF	17 S_{16}, 26 S_{17}, 19 S_{24}	MF	ν (C=O)+ν (C—C)+ γ (CH_2)
1631	50 f_b, 16 f_c, 22 f_{ad}	ZF	10 S_{14}, 42 S_{16}, 12 S_{17}, 12 S_{23}	DMF	ν_{as} 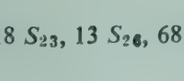 +ν (C=O) +ν (C · C)+γ
170	19 f_{bc}, 56 f_{ac}, 18 f_{ad}	ZF	18 S_{23}, 13 S_{26}, 68 S_{27}	PF	δ (C—C)+δ (C—C=C) +γ
1047	15 f_d, 63 f_{dl}	ZF	64 S_{13}, 16 S_{14}	SMF	γ $(CH_3)_2$+ν_{as}

(Contd.)

Table 5—PED and Vibrational Assignment of Deuterated N, N-Dimethyl Acrylamides (Contd)

Calc. frequency cm^{-1})	PED in internal force constants	Type of mode	PED in symmetry coordinates	Nature of mode	Vibrational assignment
			CD_2 CD CON C_2H_6		
			A″ species		
2978	101 f_l	GF	100 S_{34}	PF	ν_{as} $(CH_3)_2$
2978	101 f_l	GF	100 S_{35}	PF	ν_{as} $(CH_3)_2$
1458	11 f_{dl}, 88 f_{lm}	GF	85 S_{36}, 12 S_{38}	PF	δ_{as} $(CH_3)_2$
1465	14 f_{dl}, 85 f_{lm}	GF	80 S_{37}, 15 S_{39}	PF	δ_{as} $(CH_3)_2$
1076	79 f_{dl}, 12 f_{lm}	GF	90 S_{36}, 15 S_{39}	PF	γ $(CH_3)_2$
1129	76 f_{dl}, 15 f_{lm}	GF	10 S_{37}, 80 S_{39}	PF	γ $(CH_3)_2$
			CH_2 CH CON C_2D_6		
			A′ species		
2825	98 f_i	GF	98 S_1	PF	ν (C—H)
3095	101 f_j	GF	99 S_2	PF	ν_{as} (CH_2)
3030	97 f_j	GF	99 S_3	PF	ν_s (CH_2)
2239	97 f_l	GF	95 S_4	PF	ν_{as} $(CH_3)_2$
2227	99 f_l	GF	98 S_5	PF	ν_{as} $(CH_3)_2$
2111	95 f_l	GF	98 S_6	PF	ν_s $(CH_3)_2$
2116	94 f_l	GF	97 S_7	PF	ν_s $(CH_3)_2$
1052	90 f_{lm}	GF	90 S_8	PE	δ_{as} $(CH_3)_2$
1045	93 f_{lm}	GF	93 S_9	PF	δ_{as} $(CH_3)_2$
1111	15 f_d, 14 f_c, 12 f_{hj}, 20 f_{dl} 20 f_{lm}	DF	35 S_{10}, 11 S_{15}, 13 S_{17}	DMF	$\delta_s(CH_3)_2+\nu_s$(N(CH$_3$)$_2$)$+\nu$ (C—C)
1033	20 f_{hi}, 14 f_{ci}, 29 f_{dl}, 18 f_{lm}	DF	32 S_{11}, 34 S_{17}	SMF	δ_s $(CH_3)_2+\nu$ (C—C)
1472	13 f_d, 61 f_a	ZF	11 S_{15}, 13 S_{19}, 56 S_{22}	SMF	ν (C—N)$+\nu_s$(N(CH$_3$)$_2$) $+\delta$(N(CH$_3$)$_2$)
1076	12 f_{hj}, 31 f_{dl}, 23 f_{lm}	DF	42 S_{10}, 14 S_{21}, 10 S_{24}	DMF	δ_s $(CH_3)_2+\delta$ (C—H)$+\gamma$ (CH_2)
874	12 f_a, 41 f_{dl}	DZF	44 S_{12}, 14 S_{22}	DMF	γ $(CH_3)_2+\nu$ (C—N)
528	34 f_d, 22 f_{ab}, 11 f_{ad}	DZF	12 S_{14}, 22 S_{15}, 11 S_{23}, 28 S_{25}	MF	ν_{as}(N(CH$_3$)$_2$)$+\nu_s$(N(CH$_3$)$_2$) $+\gamma$(N(CH$_3$)$_2$) $+\delta$ (O=C—N)
988	24 f_c, 10 f_{hi}, 10 f_{ci}, 33 f_{dl} 20f_{lm},	DZF	40 S_{11}, 24 S_{17}, 20 S_{21}	DMF	δ_s $(CH_3)_2+\nu$ (C—C)$+\delta$ (C—H)
289	13 f_c, 18 f_{bc}, 39 f_{ab}, 34 f_{ad}	ZF	13 S_{17}, 32 S_{23}, 34 S_{25} 39 S_{27}	SMF	ν (C—C)$+\gamma$(N(CH$_3$)$_2$)$+\gamma$ (CH_2) $+\delta$ (C—C)
1334	46 f_d, 18 f_b, 10 f_{dl}	DZF	45 S_{14}, 19 S_{16}	DMF	ν_{as}(N(CH$_3$)$_2$) $+\nu$ (C=O)
684	40 f_d, 10 f_{ch}, 25 f_{dl}	DZF	12 S_{10}, 20 S_{12}, 37 S_{15}	SMF	δ_s $(CH_3)_2+\gamma$ $(CH_3)_2+\nu$(N(CH$_3$)$_2$)
1292	15 f_h, 56 f_{hj}, 11 f_{ch}	ZF	15 S_{18}, 37 S_{20}, 30 S_{24}	SMF	ν (C=C)$+\delta$ $(CH_2)+\gamma$ (CH_2)

(Contd.)

Table 5—PED and Vibrational Assignment of Deuterated N, N-Dimethyl Acrylamides (Contd)

Calc. frequency (cm^{-1})	PED in internal force constants	Type of mode	PED in symmetry coordinates	Nature of mode	Vibrational assignment
			CH_2 CH CON C_2D_6		
			A′ species		
1627	24 f_c, 48 f_h, 17 f_{hj}	ZF	20 S_{17}, 46 S_{18}, 19 S_{20}	SMF	ν (C—C)+ν (C=C)+δ (CH_2)
374	33 f_{ch}, 11 f_{ad}, 25 f_{de}	DZF	33 S_{19}, 37 S_{26}	SMF	$\delta\left(N\begin{smallmatrix}CH_3\\CH_3\end{smallmatrix}\right)+\delta$ (C—C=C)
463	18 f_d, 12 f_c, 14 f_{ch}, 10 f_{ac}, 10 f_{ad}, 17 f_{de}	DF	12 S_{15}, 10 S_{17}, 23 S_{19}, 16 f_{26}	MF	$\nu_s\left(N\begin{smallmatrix}CH_3\\CH_3\end{smallmatrix}\right)+\nu$ (C—C) $+\delta\left(N\begin{smallmatrix}CH_3\\CH_3\end{smallmatrix}\right)+\delta$ (C—C=C)
1420	50 f_{hj}	DZF	20 S_{20}, 10 S_{21}, 36 S_{24}	DMF	δ (CH_2)+δ (C—H)+γ (CH_2)
1650	44 f_b, 10 f_h, 10 f_{ac}	DZF	36 S_{16}, 11 S_{18}	DMF	ν (C=O)+ν (C=C)
170	17 f_{bc}, 54 f_{ac}, 24 f_{ad}	ZF	24 S_{23}, 70 S_{27}	PF	$\gamma\left(N\begin{smallmatrix}CH_3\\CH_3\end{smallmatrix}\right)+\delta$ (C—C)
806	75 f_{dl}	GF	79 S_{13}	PF	γ $(CH_3)_2$
			A″ species		
2222	100 f_l	GF	100 S_{34}	PF	ν_{as} $(CH_3)_2$
2222	100 f_l	GF	100 S_{35}	PF	ν_{as} $(CH_3)_2$
1043	93 f_{lm}	GF	90 S_{36}	PF	δ_{as} $(CH_3)_2$
1049	11 f_{dl}, 87 f_{lm}	GF	82 S_{37}, 15 S_{39}	PF	δ_{as} $(CH_3)_2$
818	84 f_{dl}	GF	85 S_{28}	PF	γ $(CH_3)_2$
889	78 f_{dl}, 12 f_{lm}	GF	10 S_{37}, 80 S_{39}	PF	γ $(CH_3)_2$
			CD_2 CD CON C_2 D_6		
			A′ species		
2115	46 f_i, 44 f_l	ZF	46 S_1, 45 S_7	SMF	ν (C—H)
2331	97 f_j	GF	95 S_2	PF	ν_{as} $(CH)_2$
2225	70 f_j, 19 f_l	GF	71 S_3, 19 S_5	PF	ν_s (CH_2)
2239	97 f_l	GF	96 S_4	PF	ν_{as} $(CH_3)_2$
2227	16 f_j, 80 f_l	GF	16 S_3, 79 S_5	PF	ν_{as} $(CH_3)_2$
2111	95 f_l	GF	98 S_6	PF	ν_s $(CH_3)_2$
2117	39 f_i, 51 f_l	ZF	39 S_1, 52 S_7	SMF	ν_s $(CH_3)_2$
1052	92 f_{lm}	GF	91 S_8	PF	δ_{as} $(CH_3)_2$
1045	93 f_{lm}	GF	93 S_9	PF	δ_{as} $(CH_3)_2$
1095	19 f_d, 51 f_{dl}, 37 f_{lm}	ZF	72 S_{10}, 14 S_{15}	PF	δ_s $(CH_3)_2+\nu_s\left(N\begin{smallmatrix}CH_3\\CH_3\end{smallmatrix}\right)$
1033	11 f_{hj}, 46 f_{dl}, 29 f_{lm}	ZF	48 S_{11}, 19 S_{24}	DMF	δ_s $(CH_3)_2+\gamma(CH_2)$
1468	14 f_d, 59 f_a, 10 f_{de}	ZF	11 S_{15}, 13 S_{19}, 56 f_{22}	SMF	$\nu_s\left(N\begin{smallmatrix}CH_3\\CH_3\end{smallmatrix}\right)+\delta\left(N\begin{smallmatrix}CH_3\\CH_3\end{smallmatrix}\right)+\nu$ (C—N)
754	42 f_{hi}, 35 f_{ci}	ZF	77 S_{21}	PF	ν (C—H)
829	27 f_{hj}, 31 f_{dl}	DF	33 S_{12}, 26 S_{24}	DMF	γ $(CH_3)_2+\gamma$ (CH_2)
518	30 f_d, 24 f_{ab}, 11 f_{ad}	DF	11 S_{14}, 19 S_{15}, 11 S_{23}, 32 S_{25}	MF	$\nu_{as}\left(N\begin{smallmatrix}CH_3\\CH_3\end{smallmatrix}\right)+\nu_s\left(N\begin{smallmatrix}CH_3\\CH_3\end{smallmatrix}\right)+\gamma\left(N\begin{smallmatrix}CH_3\\CH_3\end{smallmatrix}\right)+\delta$ (O=C—N)

(Contd.)

Table 5—PED and Vibrational Assignment of Deuterated N, N-Dimethyl Acrylamides (Contd)

Calc. frequency (cm^{-1})	PED in internal force constants	Type of mode	PED in symmetry coordinates	Nature of mode	Vibrational Assignment
			CD_2 CD CON C_2 D_6		
			A' species		
934	$12 f_c$, $26 f_{hi}$, $25 f_{dl}$	DF	10 S_{11}, 17 S_{12}, 12 S_{17}	MF	$\delta_s (CH_3)_2 + \gamma (CH_3)_2 + \nu$ (C—C)
288	$12 f_c$, $17 f_{bc}$, $39 f_{ab}$, $36 f_{ad}$	ZF	35 S_{23}, 33 S_{25}, 26 S_{27}	SMF	$\gamma\left(N\begin{smallmatrix}CH_3\\CH_3\end{smallmatrix}\right) + \delta$ (O=C—C) $+\delta$ (C—C)
1338	$54 f_d$, $15 f_b$, $11 f_{dl}$	ZF	19 S_{11}, 55 S_{14}, 16 S_{16}	SMF	$\delta_s (CH_3)_2 + \nu_{as}\left(N\begin{smallmatrix}CH_3\\CH_3\end{smallmatrix}\right)$ $+ \nu$ (C=O)
668	$43 f_d$, $19 f_{dl}$	DZF	12 S_{10}, 14 S_{12}, 40 S_{15}	DMF	$\delta_s (CH_3)_2 + \gamma (CH_3)_2$ $+ \nu_s\left(N\begin{smallmatrix}CH_3\\CH_3\end{smallmatrix}\right)$
997	$49 f_{hj}$, $13 f_{jk}$, $14 f_{bc}$	DZF	16 S_{11}, 45 S_{20}, 17 S_{24}	DMF	$\delta_s (CH_3)_2 + \delta (CH_2) + \gamma (CH_2)$
1542	$23 f_c$, $62 f_h$	ZF	18 S_{17}, 60 S_{18}	SMF	ν (C—C) + ν (C=C)
351	$38 f_{ch}$, $19 f_{de}$	DZF	25 S_{19}, 43 S_{26}	SMF	$\delta\left(N\begin{smallmatrix}CH_3\\CH_3\end{smallmatrix}\right) + \delta$ (C—C=C)
454	$16 f_d$, $11 f_c$, $13 f_{ad}$, $23 f_{de}$, $10 f_{dl}$	DF	11 S_{15}, 31 S_{19}, 10 S_{26}	MF	$\nu_s\left(N\begin{smallmatrix}CH_3\\CH_3\end{smallmatrix}\right) + \delta\left(N\begin{smallmatrix}CH_3\\CH_3\end{smallmatrix}\right)$ $+ \delta$ (C—C=C)
1230	$18 f_b$, $31 f_c$, $26 f_{hj}$	DF	17 S_{16}, 19 S_{17}, 20 S_{24}	MF	ν (C=O) + ν (C—C) + γ (CH_2)
1626	$52 f_b$, $17 f_c$, $12 f_{ad}$	ZF	46 S_{16}, 13 S_{17}, 11 S_{23}	DMF	ν (C=O) + ν (C—C) + $\gamma\left(N\begin{smallmatrix}CH_3\\CH_3\end{smallmatrix}\right)$
161	$17 f_{be}$, $54 f_{ac}$, $22 f_{ad}$	ZF	22 S_{23}, 11 S_{26}, 66 S_{27}	PF	$\gamma\left(N\begin{smallmatrix}CH_3\\CH_3\end{smallmatrix}\right) + \delta$ (C—C=C) $+\delta$ (C—C)
806	$75 f_{dl}$	GF	79 S_{13}	PF	$\gamma (CH_3)_2$
			A'' species		
2222	$100 f_l$	GF	100 S_{34}	PF	$\nu_{as} (CH_3)_2$
2222	$100 f_l$	GF	100 S_{35}	PF	$\nu_{as} (CH_3)_2$
1043	$93 f_{lm}$	GF	95 S_{36}	PF	$\delta_{as} (CH_3)_2$
1049	$11 f_{dl}$, $87 f_{lm}$	GF	90 S_{37}, 10 S_{39}	PF	$\delta_{as} (CH_3)_2$
818	$84 f_{dl}$	GF	85 S_{38}	PF	$\gamma (CH_3)_2$
889	$78 f_{dl}$, $12 f_{lm}$	GF	10 S_{37}, 85 S_{39}	PF	$\gamma (CH_3)_2$

DMAC has been doubly assigned to the fundamentals due to symmetric stretches of $(CH_3)_2$ as indicated by normal coordinate analysis. The Raman band at 2961 cm^{-1}, which is stronger than that at 2937 cm^{-1}, is doubly assigned to the A'' asymmetric stretches of $(CH_3)_2$ and a relatively weak Raman band at 3000 cm^{-1} is doubly assigned to A' asymmetric stretches of $(CH_3)_2$. Both these bands are absent from the infrared spectrum. The corresponding bands of DMAC-d_3 are calculated to be near 2930, 2931, 2978, 2978, 2985 and 2980 cm^{-1} while those of DMAC-d_8 and DMAC-d_9 are predicted near 2111, 2116, 2222, 2222, 2239 and 2227 cm^{-1}. The isotopic shifts, the magnitude of the frequencies and their assignment are reasonable when compared with their counter parts in some dimethyl compounds such as DMA,[7,8] DMSF,[9] dimethyl diazinine,[33] and dimethyl sulphone.[34] This is also confirmed by the PED given in Tables 3 and 5 as the corresponding symmetry coordinate contributes almost 100% of potential energy to these modes. The assignment of the vibrational modes near 2115 and 2117 cm^{-1} in DMAC-d_9, which show a mixing, are aided by their assignment in DMAC-d_8.

Ten distinct bands are expected in DMAC in the region 1000-1500 cm^{-1} which can be reasonably assigned to the deformational modes of methyl groups. But the infrared spectrum reveals only five bands near 1460, 1376, 1405, 1148 and 1054 cm^{-1} and the Raman spectrum shows only four bands near 1458, 1400, 1150 and 1058 cm^{-1}. Depending on the PED and the calculated values of frequencies, the band at 1460 cm^{-1} is assigned to the two asymmetric deformations of A' type and two asymmetric deformations of A'' type of the $(CH_3)_2$. On deuteration, as expected from PED and related compounds, these appear in the region 1040-1050 cm^{-1} with essentially unchanged composition. The bands at 1148 and 1054 cm^{-1} are each doubly assigned to the A' and A'' rocking modes. On deuteration these modes, as expected go down to near 874 and 806 cm^{-1} in A' species and 889 and 818 cm^{-1} in A'' species respectively. The bands at 1376 and 1405 cm^{-1} are assigned to the symmetric deformation of $(CH_3)_2$. The PED obtained on the basis of GVFF shows the former to be pure and the latter to be a mixed mode. As a result, the band at 1376 cm^{-1} is expected to show a larger isotopic shift than that at 1405 cm^{-1}. But the calculated frequencies of these modes in DMAC-d_6 appear at 1111 and 1033 cm^{-1} respectively. The distributions in MUBFF show the band at 1376 cm^{-1} to be mixed and that at 1405 cm^{-1} to be pure, accounting for the isotopic shifts. Hence these are assigned on the basis of the PED in MUBFF. On the basis of the PED in UBFF, the symmetric modes of $(CH_3)_2$ should appear at 1418 and 1430 cm^{-1} and both of them are pure. This is again in contradiction with the expected isotopic shifts. This could be an inadequacy of the UBFF. A similar case was recorded by Sundius in the case of chlorinated alkanes.[31] The assignments in Tables 4 and 5 are made on the above line of reasoning.

4.3.2 *Frequencies of the ethylene group*—The infrared bands at 2825, 3095 and 3030 cm^{-1} are assigned to (C—H) stretching, and asymmetric and symmetric modes of CH_2 stretching vibrations. On deuteration, they shift to 2116, 2331 and 2227 cm^{-1}. The assignments are confirmed on the basis of PED in Tables 3 and 5.

The band near 1612 cm^{-1} in infrared spectrum which is very strong in Raman near 1614 cm^{-1} is essentially due to $\nu(C{=}C)$ mixing with $\delta(CH_2)$. This mixing is substantiated by the fact that it shifts to 1543 cm^{-1} on deuteration of ethylene group and remains unaltered on deuteration of methyl groups.

The bands near 1422, 1054 and 1298 cm^{-1} were assigned to the deformational modes of (CH_2) and CH groups. This is reasonable when compared to their values in acrylamide.[10] They undergo the expected shift on deuteration on the basis of PED. The vibration $\delta(C{=}C{-}C)$ was assigned to the Raman shift near 505 cm^{-1} and PED in Table 3 shows that it mixes with $N(CH_3)_2$ deformational mode.

The shifts on deuteration of most of these bands are comparable with those of vinyl chloride.[35]

4.3.3 *Frequencies of the amide group*—The strongest infrared band near 1650 cm^{-1} which has a relatively weak Raman counterpart near 1654 cm^{-1}; is assigned to amide band I. On deuteration of ethylene group, it shows a small shift to 1631 cm^{-1} confirming a small contribution from $\gamma(CH_2)$.

The strong infrared band near 1495 cm^{-1}, is assigned to the amide band III. The calculated frequency at 1472 cm^{-1} on deuteration of methyl groups is in accordance with its mixing with $\gamma(CH_3)_2$.

Neither amide I, nor the amide III bands are group frequencies from the quantitative point of view as can be seen from the PED given in Tables 3 and 5.

The symmetric and asymmetric stretching vibrations of $N\begin{smallmatrix}CH_3\\CH_3\end{smallmatrix}$ are assigned by taking into account their characteristic interchange of intensity in infrared and Raman. Thus, the weak infrared band near 760 cm^{-1} and relatively strong band near 1262 cm^{-1} which have strong and relatively weak Raman counter parts near 760 and 1269 cm^{-1} respectively are assigned to symmetric and asymmetric modes of $\left(N\begin{smallmatrix}CH_3\\CH_3\end{smallmatrix}\right)$. The shift on deuteration of methyl groups is in accordance with their mixing with $\gamma(CH_3)_2$.

The frequency of $\delta(C{-}C)$ vibration was not observed. Hence it was given a zero weight during refinement. Its calculated value is near 180 cm^{-1} according to GVFF calculations. This agrees with the value reported for DMA[7,8] by Lagrange near 168 cm^{-1} and in variance with that reported by Durga Prasad *et al.*[6] for the same molecule near 470 cm^{-1}. The PED shows that it is predominently $\delta(C{-}C)$ in character.

It is not difficult to assign the other modes of vibration. Some of the vibrations of the A'' species were assigned tentatively by comparing with the assignments in related systems. These are given in Table 4 along with the vibrational assignment of other frequencies.

5. Conclusions

1. There is no unique way of obtaining force constants for big molecules.
2. Usage of UBFF is disadvantageous to classify normal modes as some non-bonded repulsion constants contribute enormously.
3. Using several potential functions in normal coordinate analysis is always fruitful, as the misassignment of frequencies due to certain potential energy distributions characteristic of the potential function used, can be avoided.
4. The stretching vibrations of $(CH_3)_2$, CH_2, CH and their deuterated analogs are pure as the corresponding symmetry coordinate contributes 100% of potential energy.
5. The asymmetric deformations of $(CH_3)_2$, $(CD_3)_2$ along with A'' rocking modes are pure.
6. Amide I and III bands are by no means group frequencies.
7. Other frequencies can be said to be mixed as several other bands contribute to their potential energy.
8. In general, group frequencies are pure frequencies; zone frequencies show selective mixing, delocalized zone frequencies exhibit delocalized mixing and delocalized frequencies are mixed frequencies.

Acknowledgement

The authors thank Prof. N A Narasimham, Head, Spectroscopy Division, Bhabha Atomic Research Centre (BARC), Bombay, for providing experimental and computational facilities. They are also thankful to Dr V B Kartha (BARC), for helpful discussions.

References

1. Venkata Chalapathi V & Venkata Ramiah K, *Proc. Indian Acad. Sci.*, 68 (1968), 109.
2. Venkata Chalapathi V & Venkata Ramiah K, *Curr. Sci.*, 37 (1968), 453.
3. Venkata Ramiah K & Syamala Krishna Sayee P, *Curr. Sci.*, 38 (1969), 457.
4. Indira Chary C A & Venkata Ramiah K, *Proc. Indian Acad. Sci.*, 69 (1969), 18.
5. Durga Prasad G, Sathyanarayana D N & Patel C C, *Bull. chem. Soc. Japan*, 44 (1971), 316.
6. Durga Prasad G, Sathyanarayana D N, Patel C C *et al.*, *Spectrochim. Acta*, 28A (1972), 2311.
7. Garigou-Lagrange C, DE Loze C, Bacelon P *et al.*, *J. Chim. Phys.*, 67 (1970), 1936.
8. Garigou-Lagrange C & Therese Forel M, *J. Chim. Phys.*, 68 (1971), 1329.
9. Anthoni U, Henriksen L, Nielson P H *et al.*, *Spectrochim. Acta*, 30A (1974), 1351.
10. Ramana Rao G, Balasubrahmanian V & Venkata Ramiah K, *Indian J. pure appl. Phys.*, 13 (1975), 546.
11. Ramana Rao G & Venkata Ramiah K, To be communicated.
12. Wilson E B, *J. chem. Phys.*, 7 (1939), 1047; 9 (1941), 96.
13. Jakes J & Schneider B, *Czech. chem. Commun.*, 33 (1968), 643.
14. Shimanouchi T, *J. chem. Phys.*, 17 (1949), 245, 734, 848.
15. Turner J D & Lingafelter E C, *Acta Crystallogr*, 8 (1955), 551.
16. Turner J D & Lingafelter E C, *Acta Crystallogr.*, 8 (1955), 549.
17. Kurokawa S, *Bull. chem. Soc. Japan*, 28 (1955), 660.
18. Brathorde J R & Lingafelter E C, *Acta Crystallogr.*, 11 (1958), 729.
19. Ramana Rao G, Balasubrahamanian V & Venkata Ramiah K, *Indian J. pure appl. Phys.*, 16 (1978), 657.
20. Ramana Rao G & Venkata Ramiah K, Under Preparation.
21. Kuroda Y, Saito Y, Machida K & Uno T, *Bull. chem. Soc. Japan*, 45 (1972), 2371.
22. Marquardt D W, *SIAM Journal*, 11 (1963), 431.
23. Papousek D, Tolmen S & Pliva J, *J. molec. Spectrosc.*, 15, (1965), 502.
24. Fuhrer H, Kartha V B, Krueger P J *et al.*, *Chem. Rev.*, 72 (1972), 439.
25. Fuhrer H, Kartha V B, Kidd G *et al.*, *Nat. Res. Counc. Can., NRCC Bull. No.* 15, *Computer Programmes for infrared* Spectrophotometry, 5 (1976), 192.
26. Usha Bai P & Venkata Ramiah K, *Indian J. pure appl. Phys.*, 11 (1973), 171.
27. Shimanouchi T, *Molecular force field in physical Chemistry—an advanced treatise* Vol. IV. Ed Erying, Henderson and Jost.
28. Ken Ohwada, *Spectrochim. Acta*, 34A (1978), 147.
29. Scherer J R & Overend J, *Spectrochim. Acta*, 17 (1961), 719.
30. Jakes J & Krimm S, *Spectrochim. Acta*, 27A (1971), 1934.
31. Sundius T, *Spectrochim. Acta*, 32A (1976), 415.
32. Jensen K A, Dahl B M, Nielsen P H & Borch G, *Acta Chem. Scand.*, 25 (1971), 2029, 2039; 26 (1972), 2241.
33. Mitchell R W & Merritt J A, *J. molec. Spectrosc.*, 27 (1968), 27.
34. Uno T, Machida K & Hanai K, *Spectrochim. Acta*, 27A (1971), 107.
35. Zaki El-Sabban M & Zwolinski Bruno J, *J. molec. Spectrosc.*, 27 (1968), 1.

Indian Journal of Pure & Applied Physics
Vol. 18, February 1980, pp. 107-109

Effect of Etching Conditions on Track Registration Characteristics of Soda Lime Glass Detector

M M Ahmad, A Khan & D S Srivastava
Physics Section, Z H College of Engineering & Technology, Aligarh Muslim University, Aligarh 202 001

Received 29 *January* 1979

Effect of stirring, concentration and temperature of HF etchant on bulk etch rate and track etch rate for Cf-252 fission fragments in a soda lime glass, has been studied. It has been found that vigorous stirring removes the etch product layer from the surface of the detector and gives a constant etch rate. A function $V_G(N, T)$ has been fitted to the observed data on variation of V_G with normality (N) and temperature (T) of the etchant. Although the bulk etch rate is found to increase with concentration of HF at 20°C, the track etch ratio (V_T/V_G) and the related parameters, viz. the critical angle and the etching efficiency are found to be practically independent of the concentration.

1. Introduction

Soda lime glass microscope slides have been used by many workers as detectors for fission fragments in the study of (n, f) reaction[1] and also in the neutron flux measurements.[2,3] In the glass standards used as neutron dosimeters, the uranium content of the glass itself produces fission fragments due to neutron-induced fission. These fission fragments give a track density, (ρ_D) on a freshly opened etched surface of the detector which is related to the neutron dose (ϕ) by the relation $\rho_D = B\phi$ where B is a constant whose value is known from calibration experiments. In order to use the same constant value of B for a given glass standard, its etching must strictly be performed under the prescribed standard conditions[4] (viz. 5 sec in 48% HF at 23°C for the glass dosimeter of Fleischer *et al.*[2])

Since usually small etching times of a few seconds in 40-48% HF are prescribed for standard glass dosimeters, the time of transit in removing the glass detector from the etching solution (at 23°C) to the flowing water bath is comparable to the etching time. During this time, the concentrated HF adhering to the glass surface keeps on etching it. The effect of this extra etching is appreciable, particularly in those laboratories where the room temperature is much higher (35 to 45°C) than the prescribed etching temperature of 23°C. This results in an error in using the same constant value B as given for the glass standard used. This error can be greatly minimized if one uses a lower concentration of the HF etchant and etches the glass dosimeter at the higher room temperature for a time which will give the same value of removed layer as is obtained under the prescribed standard etching conditions.

It was, therefore, proposed to study the effect of etching conditions, concentration, temperature and stirring of the etchant on the track registration characteristics, viz. the bulk etch rate V_G, the track etch rate V_T and related quantities like the critical angle and the etching efficiency of the soda lime glass detector.

2. Experimental Details

Soda lime glass local microscope slides[3] were cut to pieces of about 1 cm^2 size and were washed in alcohol. They were then etched in hydrofluoric acid of different concentrations kept in polythene containers in well controlled (temp., $\pm 0{\cdot}2$ °C) water bath. The bulk etch rates (V_G) were obtained by measuring the removed layer after definite intervals of etching using a precision dial gauge of 1 μm accuracy. The track etch rates (V_T) for normally entering fission fragments were derived from the slope measurements of the track diameter growth curves, using the initial linear parts of the curves, for which the slope is given by

$$\frac{dD}{dt} = 2\,V_G \left\{ \frac{V_T/V_G - 1}{V_T/V_G + 1} \right\}^{1/2}$$

The etching solution was constantly stirred by means of a magnetic stirrer at an angular speed of 300 rev/min.

3. Results and Discussion

3.1 Effect of Stirring

In an unstirred HF solution, the measured bulk etch rate (V_G) was found to be constant only when shorter etching intervals ($\leqslant 5$ sec) were used for successive etching. For longer etching intervals (10 sec or more), the measured bulk etch rate was found to decrease with increase of etching intervals. This necessitated the stirring of the etching solution. On using a medium angular speed ($\simeq$ 300 rpm), the same constant value of bulk etch rate was obtained for etching intervals as long as 20 sec (Fig. 1). For etching intervals of more than 20 sec, the bulk etch rate slightly decreased even after stirring. A higher stirring speed might recover this effect but then the etching solution started splashing out of the container.

The cause for the decrease of the bulk etch rate was considered to be due to the concentrated etch product of the glass adhering to the detector surface. Vigorous stirring of the etchant keeps on removing this layer, and hence gives a constant value of V_G. Our contention was confirmed by etching the glass detector in 48% HF saturated with the etch product of glass. A lower value of V_G was obtained in this case. This effect in glass detector is reverse of what was found for plastic detector by Enge *et al.*[5]

3.2 Effect of Concentration and Temperature of HF on V_G

For a given concentration, the bulk etch rate was found to increase exponentially with the etching temperature, given by a relation of the type $V_G = A \exp(-E_a/kT)$ where A is a constant and E_a the activation energy of bulk etching, k the Boltzmann constant and T the absolute temperature of the etchant. The activation energy of bulk etching can be derived from the slope (m) of the ($\log_{10} V_G$) versus ($1/T$) curve and is given by

$$E_a = 0{\cdot}1986 \times m \text{ (in eV)} \qquad \ldots(1)$$

The bulk etch rate was found to increase with the concentration of the HF solution as well; the activation energy of bulk etching was, however, found to be independent of the normalities of the hydrofluoric acid (between 5 N and 24 N).

Our observed variation of bulk etch rate of the soda lime glass detector (Table 1) with etching temperature (T, K) and concentration (normality N) of the etching solution was fitted to the function

$$V_G(N,T) = 2{\cdot}66 \times 10^8 \exp\left\{ 31 - \frac{71}{N+7{\cdot}2} - \frac{10^3}{0{\cdot}1155\,T} - 0{\cdot}0635\,T \right\} \text{ (in } \mu m/\text{sec)} \qquad \ldots(2)$$

using a computer program. A plot showing the variation of the above function with T and the experimental points distributed on it gives straight lines parallel to each other, for different concentrations of the etching solution from which it can be concluded that the activation energy of bulk etching is independent of the normality of the etching solution.

The value of activation energy for bulk etching of our soda lime glass detector is found to be 0·244 eV from Eq. (2) and 0·243 $\pm$ 0·012 eV from separate plots of the data and Eq. (1).

Eq. (2) is useful in selecting a suitable etching time for soda lime glass detector using a dilute HF solution at room temperature so as to reach the same value of removed layer from single surface of the detector as is obtained under the prescribed etching conditions.

3.3 Effect of Concentration of HF On V_T/V_G

Figs. 2 and 3 show the results of bulk etch rate and track diameter measurements for fission fragments in the soda lime glass detector at 20°C with

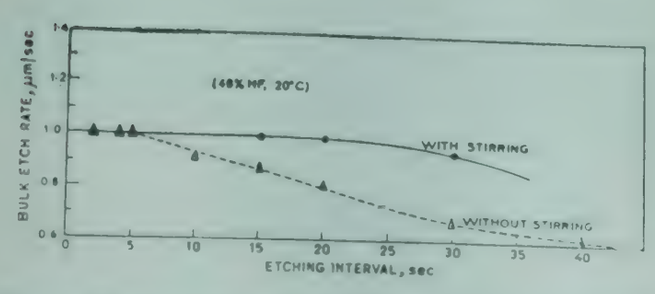

Fig. 1—The measured bulk etch rate versus etching intervals used during successive etching with stirring and without stirring the solution

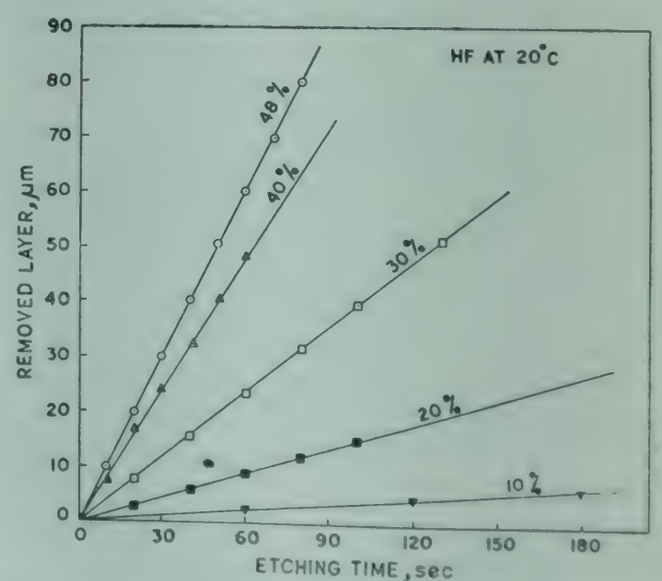

Fig. 2—Removed layer from single surface of glass versus the etching time with concentration of HF as parameter at 20°C

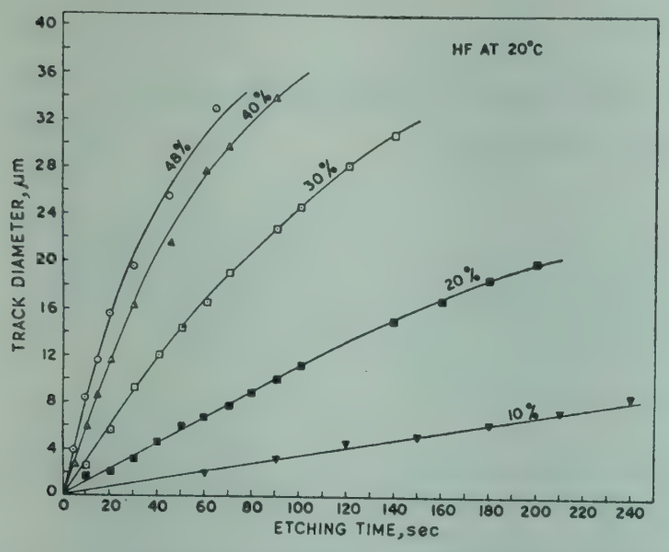

Fig. 3—Track diameter (for larger tracks) versus etching time for Cf-252 irradiated fission fragments in soda lime glass detector with concentration of HF as parameter at 20°C

Table 1—Variation of V_G for Soda Lime Glass Detector with T and Concentration of HF, and Variation of V_T/V_G, θ_c and η with Concentration* of HF at 20°C

Concentration of HF		V_G in μ m/sec at			V_T/V_G in 48% HF at 20°C	θ_c	η
%	Normality, N	20°C	30°C	40°C			
48	24	1·01	1·4	1·9	1·40	45·6*	0·29
40	20	0·81	1·15	1·55	1·33	48·8*	0·25
30	15	0·39	0·53	0·70	1·35	47·8*	0·26
20	10	0·15	0·21	0·28	1·34	48·3°	0·25
10	5	0·042	0·055	0·075	1·39	46·0°	0·28

* θ_c and η values are for 48% HF at 20°C

concetration of HF as the parameter. The derived variation of V_G and V_T/V_G is given in Table 1. It is seen that while the bulk etch rate (V_G) increases with concentration, the track etch ratio (V_T/V_G) remains almost constant. It may, therefore, be concluded that the critical angle for track etching [given by θ_c = arc sin (V_G/V_T)] and also track etching efficiency [given by $\eta = 1-\sin\theta_c = 1-(V_G/V_T)$] are practically independent of the concentration of the etchant.

Acknowledgement

The authors wish to thank Dr G K Mehta of the Indian Institute of Technology, Kanpur, for Cf-252 irradiation facility and Prof. T H Naqvi, Head of the Section for the laboratory facilities. Financial assistance from the University Grants Commission, New Delhi, is also gratefully acknowledged.

References

1. Csikai J & Nagy S, *J. nucl. Energy*, 21 (1967), 375.
2. Fleischer R L, Price P B & Walker R M, *Nucl. Sci. Engng*, 22 (1965), 153.
3. Srivastava D S, Sampathkumar R, Chaudhury N K & Iyer R H, BARC Rep. 752, (Bhabha Atomic Research Centre, Bombay), 1974.
4. Fleischer R L, Price P B & Walker R M, *Nuclear tracks in solids* (University of California Press, Berkeley, USA), 1975, 180.
5. Enge W, Grabisch K, Dallmeyer L, Bartholoma K P & Beaujean R, *Nucl. Instrum. Meth.*, 127 (1975), 125.

Indian Journal of Pure & Applied Physics
Vol. 18, February 1980, pp. 110-113

Dielectric Relaxation Time & Dipole Moment of Some Substituted Anilines in Benzene Solutions

S M Khameshara & M L Sisodia
Department of Physics, University of Rajasthan, Jaipur 302 004

Received 15 *December* 1978; *revised received* 6 *March* 1979

Measurements of static dielectric constant at 300kHz, refractive index (for sodium D-line) and complex dielectric constant at 9·945 GHz (X-band) have been made for 2-chloro-6-methyl aniline, 3-chloro-2-methyl aniline, 3-chloro-4-methyl aniline, 4-chloro-2-methyl aniline and 5-chloro-2-methyl aniline at 35 C in dilute solutions of benzene. Dielectric relaxation times (τ) have been determined following the three methods, viz. method of Higasi *et al.*, Gopala Krishna's method and Higasi's method. The values of τ and distribution parameter (α) show evidence for the existence of more than one relaxation mechanism. This has been interpreted in terms of intramolecular orientation of amino group occurring simultaneously with the overall molecular orientation. The values of the dipole moment determined from the Higasi's method, Gopala Krishna's method, Guggenheim's method and by vectorial addition of group moments are found to be in good agreement.

1. Introduction

The study of dielectric absorption at microwave frequencies has provided evidence for the existence of internal or intramolecular orientation in several organic molecules.[1-3] Bergmann *et al.*[4] have given a method for analyzing the dielectric relaxation data in terms of two relaxation times, one for molecular orientation (τ_1) and the other for interamolecular orientation (τ_2). Using this method Garg and Smyth[5] analyzed their data on liquid aniline and N—N′ dimethyl aniline and found that τ_1 and τ_2 are respectively 22·0 and 0·9 psec for aniline and 28·0 and 1·5 psec for N—N′ dimethyl aniline. Smyth[5] has postulated that the relatively small value of τ_2 obtained for aniline and a small change in the value of τ_2 from aniline to N—N′ dimethyl aniline can only be explained by an ammonia-like inversion of the nitrogen bonds as a possible dipole reorientation mode in stead of the group rotation around the C—N bond. Higasi *et al.*[6] have given a method for estimating either of the two relaxation times at a single frequency in terms of $\tau(1)$ and $\tau(2)$, where $\tau(2)$ refers to the molecular orientation and $\tau(1)$ is a function of τ_1, τ_2 and C_2, the weight factor for intramolecular orientation. Srivastava and Vij[7] have used this method to analyze the dielectric relaxation data for various substituted anilines and suggested that $\tau(1)$, $\tau(2)$ method given by Higasi *et al.*[6] might become a good alternative to Bergmann's method[4] for the estimation of both the dielectric relaxation times under certain conditions. The present work extends this study to some disubstituted anilines.

Although several workers[7-9] have studied various aspects of dielectric relaxation for monosubstituted anilines, no such studies have been made in case of disubstituted anilines. In the present paper, dielectric relaxation study of five disubstituted anilines namely, 2-chloro-6-methyl-aniline (A), 3-chloro-2-methyl-aniline (B), 3-chloro-4-methyl-aniline (C), 4-chloro-2-methyl-aniline (D) and 5-chloro-2-methyl-aniline (E), has been carried out in dilute solutions of benzene at 9·945 GHz, for the first time with a view to studying the relaxation mechanism involved in such molecules.

2. Experimental Details

The samples of compounds A (purum), B (purum), C (pract.), D (pract.) and E (purum) were supplied by M/s Fluka. The substances were used without any further purification. Benzene (AnalaR) supplied by M/s BDH was used after drying over sodium and double distillation. The static permittivity of solutions at 35°C was measured by the heterodyne beat method at 300 kHz. The refractive index was measured with the help of an Abbe's refractometer. The technique used for the measurements of wavelength in the dielectric and that of voltage standing wave ratio at 9·945 GHz was the same as described earlier.[10] The calculations of dielectric permittivity (ϵ') and dielectric loss (ϵ'')

Table 1—Measured Values of ϵ_0, n_D^2, ϵ' and ϵ'' for Different Compounds in Benzene Solutions at 35°C

Name of compound	Conc. (wt fraction)	ϵ_0	n_D^2	ϵ'	ϵ''
2-Chloro-6-	0·0184	2·298	2·223	2·295	0·017
methyl-aniline	0·0305	2·323	2·226	2·322	0·026
(A)	0·0417	2·368	2·230	2·347	0·040
	0·0573	2·425	2·234	2·397	0·058
	0·0636	2·450	2·236	2·419	0·065
3-Chloro-2-	0·0083	2·288	2·223	2·282	0·018
methyl-aniline	0·0207	2·355	2·227	2·326	0 043
(B)	0·0270	2·395	2·229	2·357	0·055
	0·0363	2.453	2·232	2·397	0·073
	0·0421	2·488	2·233	2·426	0·086
3-Chloro-4-	0·0121	2·280	2·222	2·288	0·018
methyl-aniline	0·0214	2·323	2·224	2·312	0·032
(C)	0·0374	2·394	2·227	2·350	0·060
	0·0403	2·413	2·228	2·361	0·066
	0·0548	2·475	2·231	2·397	0·091
4-Chloro-2-	0·0196	2·374	2·223	2·347	0·063
methyl-aniline	0·0300	2·444	2·225	2·382	0·090
(D)	0·0417	2·531	2·227	2·426	0·121
	0·0481	2·583	2·229	2·445	0·138
5-Chloro-2-	0·0194	2·344	2·221	2·315	0·050
methyl-aniline	0·0249	2·376	2·223	2·333	0.064
(E)	0·0307	2·416	2·225	2·354	0·081
	0·0480	2·521	2·229	2·411	0·129
	0·0569	2·593	2·231	2·437	0·150

For benzene $\epsilon_0 = 2{\cdot}253$ and $n_D^2 = 2{\cdot}221$

Table 2—Values of a_0, a', a'', a_∞ a_D and $(a_\infty - a_D)$ at 35°C

Solute compd	a_0	a'	a''	a_∞	a_D	$a_\infty - a_D$
A	3·80	2·73	1·10	1·60	0·29	1·31
B	6·24	4·06	1·96	2·30	0·30	2·00
C	4·53	2 60	1·63	1·22	0·22	1·00
D	7·34	3·47	2·63	1·68	0·24	1·44
E	6·45	3·26	2·69	0·99	0·26	0·73

The compound A-E are the same as detailed in Table 1

were made following the method of Heston *et al.*[11] adapted for short-circuited termination. The accuracy of measurement of ϵ' and ϵ'' is about 1% and 5% respectively. The values of ϵ_0, ϵ', ϵ'' and n_D^2 were found to be linearly dependent upon weight fraction (W_2) for all the systems and are presented in Table 1. The values of the so called slopes a_0, a', a'' and a_D were determined and are presented in Table 2. All the measurements were made at 35°C and the temperature was controlled within ± 0·5°C by a thermostat.

3. Calculations and Results

The Debye equation[12] in terms of a_0, a', a'' and a_∞ yield two independent equations.

$$\tau(1) = \frac{a''}{W(a' - a_\infty)} \quad \ldots(1)$$

$$\tau(2) = \frac{a_0 - a'}{W(a'')} \quad \ldots(2)$$

where a_0, a', a'' and a_∞ are defined in the linear range by the equations:

$$\epsilon_0 = \epsilon_1 + a_0 W_2$$

$$\epsilon' = \epsilon_1' + a' W_2$$

$$\epsilon'' = a'' W_2$$

$$\epsilon_\infty = \epsilon_{1\infty} + a_0 W_2 \quad \ldots(3)$$

Subscript 1 refers to pure solvent, 2 to pure solute, 0 to the static frequency measurement and ∞ to the values at infinite frequency. W_2 may be taken as weight fraction of the solute. Higasi *et al.*[6] have proved that

$$\tau(1) = \tau_1 \quad \ldots(4)$$

and $$\tau(1) = \tau_1(1 - C_2) + C_2 \tau_2 \quad \ldots(5)$$

This shows that results given by Eq. (2) would correspond to the dielectric relaxation time for overall or molecular orientation and those given by Eq. (1) are explicit functions of τ_1, τ_2 and C_2.

It has been proved by Vij and Srivastava[13] that $\tau(1)$ is approximately equal to τ_{GK} determined using Gopala Krishna's method.[14] It follows, therefore, that τ_{GK} depends on τ_1, τ_2 and C_2. The significant difference between $\tau(2)$ and τ_{GK} provides an indication of the presence of intramolecular orientations in molecules. With this consideration in mind, the relaxation time has also been calculated by Gopala Krishna's method.[14]

In the absence of experimental data for a wide range of frequencies, Higasi's method[15] has been used for the calculation of the distribution parameter (α) with the assumption that $a_\infty \approx a_D$. This will at least provide us with quantitative information about the existence of more than one relaxation mechanism.

The relaxation time (τ_0) has also been calculated by Higasi's method[15] for comparison.

The large difference $(a_\infty - a_D)$ provides an evidence of two-relaxation mechanism in organic molecules. One involves the rotation of the molecule as a whole and the other involves intramolecular or the group rotation. For this purpose, we have calculated $\tau(2)$ using Eq. (2) and then we calculated a_∞ from Eq. (1) on the assumption that

$\tau(1)$ is equal to $\tau(2)$. In this case the parameter a_∞ would correspond to those orientations of the molecule to which the value of $\tau(2)$ corresponds.

The dipole moment has been calculated using Higasi's equation[16]

$$\mu^2 = \frac{27\,kT\,M_2\,(a_0 - a_\infty)}{4\pi N d_1\,(\epsilon_1 + 2)^2} \qquad ...(6)$$

where M_2 is the molecular weight of the solute and all other symbols have their usual meaning.

The dipole moment has also been calculated by Gopala Krishna's method,[14] Guggenheim's method[17] and by vector addition of group moments[18] for comparison.

The evaluated values of τ_0, τ_{GK}, $\tau(1)$, $\tau(2)$, α and μ for compounds A-E are presented in Table 3.

4. Discussion

It is significant from Table 3 that the values of τ for all the molecules obtained by Gopala Krishna's method[15] are invariably lower than those obtained by Higasi's method.[15] This may be due to the fact that the former method is based on the Debye's model of single relaxation process in which α is very nearly zero whereas Higasi's model gives appreciable distribution for the relaxation process. This, therefore, provides an additional contribution to the dielectric relaxation time to these molecules and as such the τ values from Gopala Krishna's method are comparatively less than those from Higasi's method. Similar results were reported earlier by Krishnaji *et al.*[19] and Srivastava *et al.*[20] for some polar molecules.

From Table 3 it is also evident that the τ values obtained by Gopala Krishna's[14] method are less than those of $\tau(1)$. This is in agreement with the results of Vij *et al.*[13] and may be due to the fact that in Gopala Krishna's method a_∞ is assumed to be zero.

The relaxation time $\tau(2)$ for molecular or overall orientation is significantly greater than τ_{GK} and $\tau(1)$ for all the molecules. This might be due to the existence of intramolecular rotations in the molecules.

The values of τ_0 for all the molecules obtained by Higasi's method[15] are lower than the values of $\tau(2)$. This might be due to the fact that the former method gives the average value of the relaxation time whereas the latter gives the relxation time for overall orientation only. This difference between the two relaxation times also indicates the existence of intramolecular relaxation process in addition to the overall molecular relaxation process, because, in such cases, the more the contribution from the intramolecular relaxation process, the shorter is the average relaxation time.

The value $\tau(2)$, the relaxation time for overall molecular orientation for A is 15·6 psec whereas that of 2-chloro-aniline is 7·5 psec (Ref. 8). This indicates that the addition of $-CH_3$ group in the former molecule sharply increases its relaxation time which might be due to the larger size and more polarity of A than those of 2-chloro-aniline. Similar behaviour has been observed for B, C, D and E with respect to their corresponding molecules 3-chloro-aniline and 4-chloro-aniline.[8]

It should be remarked that either the *ortho*-positioned methyl group or chloro group in these substituted anilines does not produce a drastic steric hindrance either to the reorientation to the amino group or to the overall orientation of the molecule. This is supported by the fact that $\tau(2)$ for A $<$ $\tau(2)$ for B $<$ $\tau(2)$ for C $<$ $\tau(2)$ for D. Similar is the trend for τ_0, and τ_{GK}. This could be attributed to the increasing effective radius of the rotating unit and the inner friction experienced by these molecules being in the same order, and can be explained on the basis of mutual and the averaged mutual viscosities of the compounds. Similar results have been reported earlier.[7-9]

Table 3—Values of Relaxation Time (τ), Distribution Parameter (α) and Dipole Moment (μ) of the Compounds in Dilute Solution of Benzene at 35°C

Compd	$\tau \times 10^{12}$ sec				α	$\mu \times 10^{18}$ (experimental)			
	Higasi[13] (τ_0)	Gopala Krishna[14] (τ_{GK})	$\tau(1)$ Ref. 6	$\tau(2)$ Ref. 6		Higasi[16]	Gopala Krishna[14]	Guggenheim[17]	$\mu \times 10^{18}$ (calculated)
A	7·8	5·7	7·2	15·6	0·22	2·20	2·17	2·32	2·09
B	9·9	6·4	8·4	17·8	0·23	2·86	2·85	3·02	2·53
C	13·6	8·3	11·0	18·9	0·17	2·43	2·45	2·61	2·30
D	18·5	9·0	13·0	23·6	0·19	3·12	2·91	3·28	3·03
E	16·6	10·3	14·4	19·0	0·09	2·92	2·87	3·10	2·86

The large difference in the value of $(a_\infty - a_D)$ (given in Table 2) suggests that, apart from relaxation in the main dispersion region, another relaxation mechanism seems to occur in the mm range which is due to the relaxation of the amino group. One would, therefore, conclude that relaxation process in these substituted anilines involves the molecular orientation as well as the intramolecular rotational mechanism. This further suggests that dipole in anilines is inclined at a particular angle to the C—N bond, thus making the molecule non-planar. The amino group together with the benzene ring perhaps retains its pyramidal shape similar to that of an ammonia molecule even when one of its hydrogen atoms has been replaced.

Table 3 shows that the value of α for all these molecules in dilute solution of benzene is appreciable. This observation also provides an evidence of two relaxation mechanisms in anilines. The value of α for E is 0·09 while for B it is 0·23. This indicates, as is expected, that the hindrance for the intramolecular rotation of $-NH_2$ group is greater in the former molecule than that in the latter.

The μ values for all these molecules evaluated by Higasi's method,[16] Gopala Krishna's method[14] and Guggenheim's method[17] are in good agreement within the experimental error. The μ values for these molecules have also been calculated on the basis of the vectorial addition of the group moments.[18] The difference between the calculated and the experimental values of μ might be due to the non-consideration of inductive and mesomeric effects. However, the increase of the dipole moment values in these disubstituted anilines is in the same order as observed experimentally.

Acknowledgement

The authors are thankful to Dr M P Saksena, Head of the Department of Physics, for providing laboratory facilities. They are also thankful to Dr H D Purohit and P C Gupta for useful discussions. One of them (SMK) is indebted to the University Grants Commission, New Delhi, for providing with a teacher fellowship.

References

1. Fischer E & Frank F C, *Phys. Z.*, **40** (1939), 345.
2. Higasi K & Smyth C P, *J. Am. chem. Soc.*, **82** (1960), 4759.
3. Vaughan W E & Smyth C P, *J. phys. Chem.*, **65** (1961), 98.
4. Bergmann K, Roberti D M & Smyth C P, *J. phys. Chem.*, **64** (1960), 665.
5. Garg S K & Smyth C P, *Molecular relaxation processes* Chemical Society Publication No. 20, 1966, 8.
6. Higasi K, Koga Y & Nakamura M, *Bull. chem. Soc. Japan*, **44** (1971), 988.
7. Srivastava K K & Vij J K, *Bull. chem. Soc. Japan*, **43** (1970), 2307.
8. Eloranta Jaakko K, *Z. Naturf.*, **27a** (1972), 1652.
9. Srivastava S C & Suresh Chandra, *Indian J. pure appl. Phys.*, **13** (1975), 101.
10. Arrawatia M L, Gupta P C & Sisodia M L, *Indian J. pure appl. Phys.*, **15** (1977), 770.
11. Heston (Jr) W M, Franklin A D, Hennely E J & Smyth C P, *J. Am. chem. Soc.*, **72** (1950), 3443.
12. Debye P, *Z. Phys.*, **35** (1934), 101.
13. Vij J K & Srivastava K K, *Trans. Faraday Soc.*, **66** (1970), 1087.
14. Gopala Krishna K V, *Trans. Faraday Soc.*, **53** (1957), 767.
15. Higasi K, *Bull. chem. Soc. Japan*, **39** (1966), 2157.
16. Higasi K, *Denki Kenkyusho Iho*, **4** (1952), 231.
17. Guggenheim E A, *Trans. Faraday Soc.*, **45** (1949), 714.
18. Minkin V I, Osipov O A & Zhdanov Y A, *Dipole moment in organic chemistry*, translated from Russian by B J Hazzard (Plenum Press, London), 1970, 91.
19. Krishnaji, Srivastava S C & Dina Nath, *Bull. chem. Soc. Japan*, **43** (1970), 2805.
20. Srivastava S K & Srivastava S L, *Indian J. pure appl. Phys.*, **10** (1972), 693.

Indian Journal of Pure & Applied Physics
Vol. 18, February 1980, pp. 114-120

Isotope Shift in Unclassified & Some New Lines of Neodymium Spectra in the Region 3930-6450 Å

S A Ahmad & G D Saksena

Spectroscopy Division, Bhabha Atomic Research Centre, Trombay, Bombay 400 085

Received 27 *April* 1979

Isotope shifts, $\Delta\sigma$ (142-144), have been measured in neodymium spectra in the region 3930-6450 Å on a recording Fabry-Perot spectrometer using enriched isotopes excited in liquid air-cooled hollow cathodes. The isotope shift values for 269 unclassified lines, which also include new lines found in the present studies, are reported here. Earlier data are available only for 7 lines in this region. The present data will be helpful in further classification of neodymium spectra.

1. Introduction

Isotope shift data in atomic spectra are useful means for the classification of the spectra. Sometimes these may not lead to immediate unequivocal classification of the transitions involved; nevertheless, they are extremely useful in the confirmation of classification of the transitions made usually on the basis of Zeeman studies. The isotope shift data are the only means of providing information on the electronic configurations of the levels involved in a particular transition. The present studies of isotope shifts in the complex neodymium spectra have been undertaken with the above objectives in view. Isotope shift studies in neodymium spectra, involving measurement of $\Delta\sigma$ (142-144) in classified lines of Nd I (neutral atom) and Nd II (singly ionized) as well as unclassified lines in the region 3900-4760 Å have been earlier reported by Ahmad and Saksena.[1] These studies have been extended up to 6450 Å, and in this paper we report the isotope shift values $\Delta\sigma$ (142-144) for 269 unclassified lines of neodymium spectra in the entire 3930-6450 Å region. These lines could not be classified with existing energy levels as was checked by running a computer program with known energy level listings of Blaise *et al.*[2] for both Nd I and Nd II. New energy levels will have to be identified in order to classify these lines and the isotope shift data presented here will be useful for classifying them.

The present status of isotope shift measurements in neodymium spectra has been summarized by Ahmad and Saksena[1] and all the references till this date have been listed therein. Out of 269 lines for which the isotope shifts have been reported, only 7 have been studied by earlier workers.[3-5]

2. Experimental Details

The experimental set-up is essentially the same as described by Ahmad *et al.*[1] The investigations were carried out on the recording Fabry-Perot spectrometer assembled in our laboratory,[6] the source being liquid air-cooled hollow cathode lamps. The interferometric plates of fused quartz were good to $\lambda/100$ ($\lambda = 5460$ Å) and three sets of plates each with broad band, seven-layer dielectric coatings covered the entire region from 3900-6500 Å. The resolving power was $\sim 10^6$ with a 32 mm spacer.

All the lines were recorded first with single isotope of Nd ($A = 144$) of 94·5% isotopic purity. This was done in order to determine whether the line was single. Many lines reported as a single line were found to consist of close pair of lines whereas some reported doublets were found to be single lines with large isotopic shifts. For measuring isotope shift (IS), $\Delta\sigma$ (142-144), in lines showing large shifts, (IS $>$ 40 mK, mK representing milli Kaiser $= 10^3$ cm^{-1}) a mixure of ^{142}Nd (98·2 %) and ^{144}Nd (94·5 %) was used. For smaller shifts (IS $<$ 40 mK), the measurements were done using a mixture of ^{142}Nd (98·2 %) and ^{146}Nd (97·4 %) [Fig. 1]; the data were normalized to $\Delta\sigma$ (142-144) using the known value of relative isotope shift $\Delta\sigma$ (142-144)/$\Delta\sigma$ (142-146) = 1·03/2·00.

Isotope shifts in close pair of lines were measured using the "source exchange" technique described earlier by Ahmad *et al.*[7] This is illustrated in Fig. 2 where the actual separation between the two transitions λ_1 and λ_2 is 0·133 cm^{-1} for ^{144}Nd, and IS in these lines is ~ 0 and -13 mK respectively; these measurements were possible only by the "source exchange" technique.

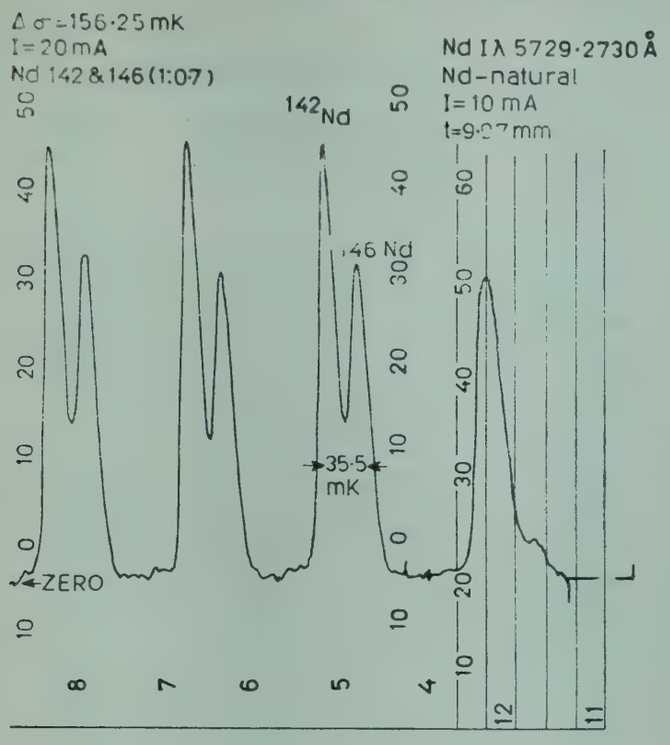

Fig. 1—The 5729·2 Å line recorded with 10 mm spacer and natural sample of Nd (reproduced on extreme right) and the three orders of the same line recorded with 32 mm spacer and a 10:7 mixture of enriched isotopes ^{142}Nd (98·2 %) and ^{146}Nd (97·4 %)

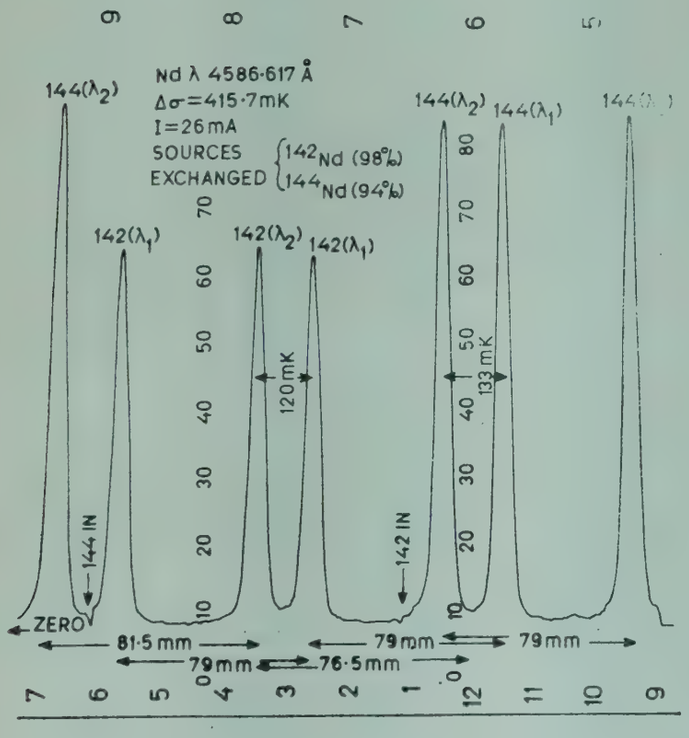

Fig. 2—Separation (133 mK) of two close lines at 4586·6 Å for ^{144}Nd and the isotope shift measurements in these two lines using "source exchange" technique with ^{142}Nd (98·2%) and ^{144}Nd (94·4 %). Isotope shift $\Delta\sigma$ (142-144) in λ_1 and λ_2 is ~ 0 and −13 mK, respectively

3. Results and Discussion

All the 269 unclassified lines for which isotope shift measurements [$\Delta\sigma$ (142-144)] have been carried out in the present study are listed in Table 1. The wavelengths have been arranged in increasing order in column 1 and their values are taken from MIT Tables,[8] King,[9] Klinkenberg,[10] Hassan[11] and Wyart.[12] Wavelength values above 4664 Å are taken from the exhaustive list of Wyart.[12] Among the 269 lines in Table 1, there are 22 lines between 4812 and 5490 Å which were reported only by Klinkenberg[10] and these have also been observed by us; the reason may be hollow cathode excitation which was used in both these studies. Line pairs denoted as λ_1 and λ_2 are very close lines whose separations have been measured using the single ^{144}Nd isotope and these are listed in Table 2. Intensities of the lines as emitted in the liquid air-cooled hollow cathode are given in column 2; the relative intensity value of the line has been deduced assuming a maximum value of 100 for the strongest line in our list at 4913·409 Å. King's "temperature classes",[9] wherever available for the lines are given in column 3. Lines belonging to "temperature classes" I, IA, II, IIA, III, IIIA, IV and IVA are found to usually belong to neutral atom (Nd I) spectrum whereas lines with IIIE, IVE or VE are mostly found to be due to singly ionized (Nd II) spectrum. The (IS) values, $\Delta\sigma$ (142-144), are given in column 4 in units of milli Kayser. The accuracy of the measurement in most of the cases is $\pm$ 3 mK. A value of $+\epsilon$ or $-\epsilon$ indicates only the sign of the shift, their magnitude being less than 10 mK.

During the course of the present study of isotope shift, it was found that in a number of cases there were additional lines in close proximity of lines previously listed in literature. The separations of these unlisted new lines from the closely listed lines have been measured using a single isotope ^{144}Nd (94·5 %). The listed wavelengths in literature are shown in column 1 of Table 2; the mean values of separation (for ^{144}Nd) of two lines λ_1 and λ_2 observed at those wavelengths are given in column 2 in units of cm^{-1}. The relative intensities of the lines are given in column 3. The λs shown in parentheses are already classified lines and, therefore, not listed in Table 1.

The expected values of IS for different types of transitions occurring in Nd I and Nd II have been discussed by Ahmad and Saksena[1] and they are presented in Fig. 3 and Fig. 4. As can be seen from Fig. 1 for Nd I significant positive IS is expected only for $4f^35d6s^2 - 4f^46s^2$ and $4f^35d6s^2 - 4f^45d6s$ transitions. Large negative IS (~ −100 mK) are expected for

Table 1—Isotope Shift Δ σ (142-144) in Unclassified Lines of Neodymium Spectra in the Region 3930-6450 Å

Wavelength* λ (Å)	Hollow cathode intensity†	Temp. class of King[9]	Δσ (142-144) (mK)	Wavelength* λ(Å)	Hollow cathode intensity†	Temp. class of King[9]	Δσ (142-144) (mK)
3936·136	10	IVE	0	4586·967	25	II	−84·9
3944·421	8	I	0	4593·95 λ	2		+57
4042·507	7	IIA	−ϵ	4606·76 λ_2	4		−90
4084·268	10	II	+31·9	4624·91	2	IVA	−66·6
4088·799	2	II	0	4628·418	10	IIIA	−70
4110·552	3	IIA	0	4629·252	10	IIA	0
4125·048	25	I	0	4649·673	65	I	−0
4224·369	10	II	−ϵ	4657·219	4	III	−41·5
4226·992	7	IVE	0	4678·203	5	IIIA	−96·2
4234·094	10	II	−72	4680·205	3	IIIA	−96·2
4235·229	8	IVE	−98·9	4702·49	4	IIIA	0
4245·814	4	IA	0	4703·11 λ_1	2		+15
4246·781	8	IIIA	−91·8	4703·11 λ_2	4	III	+95
4250·693	25	II	−52·4	4703·56 λ_1	11		−20·3
4261·841	5	IVE	−30	4726·552	30		+ϵ
4263·341	2	IIIA	0	4729·356	7	IIIA	−99·3
4310·506 λ_2	2		−78	4734·781	20	IIA	0
4319·948	5	IVA	−103·7	4735·377	4		0
4347·221	15	IA	0	4758·634	7	IIA	−ϵ
4356·02 λ_1	3		−86	4761·756	10	IIIA	0
4397·312	12	IIA	0	4762·476	5	IIIA	−34·9
4404·62 λ_2	8		−86	4774·187	5	IIIA	−75·4
4419·623	5	II	0	4775·039	4	IIIA	−116
4420·11 λ_2	7		−94	4812·21 λ_1	3		−74·5
4470·689	17	IIA	0	4812·21 λ_2	2		−45·4
4479·385	3	IIA	0	4812·665	6	IIIA	−55·4
4494·76 λ_1	3		−92	4827·562	10	III	−37·8
4499·66 λ_1	2	IVA	−132	4827·740	7	III	−10·8
4499·66 λ_2	4	IVA	−91·6	4828·58 λ_2	3		+ϵ
4501·292	3	IIIA	−90·3	4832·28 λ_2	5		+6·1
4501·952	22	IA	−ϵ	4844·297	4		−99·7
4505·01 λ_1	3	IV	0	4844·468	3		−38·4
4505·01 λ_2	2	IIIA	−88	4847·12 λ_1	4	IIIA	−59·8
4514·884	7	IIIA	0	4847·12 λ_2	3		−39·4
4516·381	3	IIIA	0	4854·53 λ_1	9	IIIA	−24·9
4527·246	47	I	0	4854·53 λ_2	5	IIIA	0
4529·154	3	IVA	−90·3	4861·773†	4	IIIA	−45·6
4539·432	5	IIA	0	4861·773	10		−7·5
4541·09	2	IVA	−63·2	4863·533	7	IIIA	−41·7
4557·768	7	IIIA	0	4864·196	18	IIIA	−25
4586·61 λ_2	30		−12·6	4867·839	19	IIIA	−95·6

(contd.)

Table 1—Isotope Shift Δσ (142-144) in Unclassified Lines of Neodymium spectra in the Region 3930-6450 Å (contd.)

Wavelength* λ (Å)	Hollow cathode intensity†	Temp. class of King[9]	Δσ (142-144) (mK)	Wavelength* λ(Å)	Hollow cathode intensity†	Temp. class of King[9]	Δσ (142-144) (mK)
4875·10 λ_1	3		−51·3	5097·723	8		−102
4875·10 λ_2	4		−43·9	5107·94	5		−81·3
4877·09 λ_1	4		+84·6	5114·526	23	IIIA	0
4877·09 λ_2	3		−40·5	5125·921*	22	IIIA	−74·2
4880·46 λ_2	10		0	5127·19 λ_2	3		+16·7
4881·215	2		−70·5	5151·00 λ_1	8	IIIA	−71·9
4883·338	5		−35·7	5151·00 λ_2	8		−51·3
4886·37 λ_1	2		−42·8	5156·04 λ_1	7		−77·6
4886·742	7		−36	5156·04 λ_2	3		−35·7
4892·180	8		−82·1	5157·15 λ_2	2		+20·5
4893·895	3		−24·8	5162·145	30	IIIA	−17·5
4899·61	7		−71·9	5168·322	10		−63
4900·37	8		−42	5173·280	4		−72·4
4904·680	9		−43·8	5173·926	10		0
4911·96 λ_1	7		−22·7	5182·23	2		0
4911·96 λ_2	2		−37·8	5182·90	10	IIIA	−23·8
4913·409	100	I	−18·9	5188·221	15	IIIA	−108·3
4914·256	7		−41·6	5191·43 λ_2	12		−13·7
4927·63	10	IIIA	−35	5203·93	5		+44·8
4929·11 λ_1	2		−38·2	5205·683	9	IIIA	−91
4930·29	4	IIIA	−42·4	5223·53	2		−60·2
4940·32 λ_1	3		−21·8	5226·239	2		−85·0
4968·182	10	IIIA	−37·8	5229·69	2		−10
4968·88 λ_1	6	IIIA	−72·3	5231·825	5		−70
4968·88 λ_2	4		−37·5	5233·023	6	IIIA	−106·2
4973·40	22	IIIA	−ϵ	5233·97	5		−65
4988·04 λ_1	9	IIIA	−101·3	5234·57	5	IIIA	+15
4988·04 λ_2	9		−41·5	5239·016	6		0
5011·04	8		−26·8	5240·683	2		−ϵ
5023·524	20		−89·4	5250·718	4	VE	−40
5025·58	12		0	5252·331	8		−15
5046·16 λ_1	17	IIIA	−75·2	5264·94	7		+36·3
5046·16 λ_2	8	IIIA	−93	5265·56	4		−ϵ
5064·72	13		−75·8	5265·756	3		−54
5069·068	20	IIIA	−96·5	5267·959	5		+20
5079·63	14	IIIA	−11·3	5270·680	3		−10
5081·89	20		−91·8	5274·509	3		−43·7
5089·721	50	II	+ϵ	5275·336	2		−15
5092·33	18	IIIA	−ϵ	5275·411	4		−ϵ
5096·51 λ_1	4		−76·2	5277·315	6		0
5097·723	5		0	5279·78	5		−20

(Contd.)

Table 1—Isotope Shift Δσ (142-144) in Unclassified Lines of Neodymium Spectra in the Region 3930-6450 Å (Contd.)

Wavelength* λ(Å)	Hollow cathode intensity†	Temp. class of King[9]	Δσ (142-144) (mK)
5281·793	6		0
5282·505	3		0
5294·10	12		+41·9
5297·349	11		−80
5300·574	22	IIIA	−102·8
5305·114	7	IIIA	0
5306·566	6		−10
5310·779	9		−52·0
5324·568	6	IIIA	−53·6
5327·141	5	IIIA	−ϵ
5349·253	4	IIIA	−ϵ
5352·188	1		−52·3
5356·10	1		+20
5362·838	6	IIIA	−49·8
5366·813	4		+ϵ
5371·375	7	III	+10
5371·756	1		−10
5379·292	4	IIIA	−20
5379·601	4	IIIA	−67·9
5383·978	4	IIIA	−42·6
5387·204	2		−15
5395·122	5		−48
5402·889	11	III	−ϵ
5408·497	1		−46·5
5410·14	1		+41
5416·87	5	III	+ϵ
5420·27	2		−15
5422·480	7	III	+15
5424·055	8	III	−63·2
5436·792	4	III	0
5438·65	3	III	−83
5440·491	6	IIIA	−0
5441·513	5	IIIA	−52·8
5447·266*	9	III	−52
5451·098	8	IVE	−22·1
5458·013	8	III	−10
5468·003	4	IIIA	+15
5468·044	3		+15
5473·744	3		−70
5484·89	6	IIIA	−34·1
5490·13	2		+10
5492·290	10	III	−51·3
5494·082	1	VE	+ϵ
5496.411	6	III	−74·1
5498·852	9	III	−32·9
5510·129	3		−75·6
5515·668	4	III	−49
5552·854	5	III	−32·2
5574·678	7	III	−67
5581·953	4	IIIA	−0
5583·156	4		−20
5601·427	11	III	−55
5606·63 λ_1	4	IIIA	−68·7
5606·63 λ_2	3		−75
5615·667	2	IIIA	0
5635·752*	22	III	−50·3
5647·993*	9	III	−65
5663·613	3	III	−32
5665·253	3	III	−10
5699·736	2	IIIA	−15
5701·569	8	III	−25·1
5717·615	3	III	+15
5731·043	7	IIIA	0
5734·27 λ_1	4		+15
5736·085	2		+10
5738·887	7		−15
5750·533	2	IIIA	−64·7
5762·362	5	III	+10
5767·328	8	III	+10
5773·89 λ_1	3	III	+ϵ
5773·89 λ_2	2		+ϵ
5777·783	2		0
5780·58	5	III	+45
5790·008	3		−10
5806·41 λ_1	1	III	−15
5806·41 λ_2	3		−38
5813·165	4	IIIA	+20
5813·879*	23	III	−48
5823·76	4	IIIA	+10
5825·11	6	IIA	+ϵ
5829·590	2	II	+15
5829.758	7	IIA	0

(Contd.)

Table 1—Isotope Shift Δσ (142-144) in Unclassified Lines of Neodymium Spectra in the Region 3930-6450 Å (Contd.)

Wavelength* λ(Å)	Hollow cathode intensity†	Temp. class of King[9]	Δσ (142-144) (mK)	Wavelength* λ(Å)	Hollow cathode intensity†	Temp. class of King[9]	Δσ (142-144) (mK)
5862·438	5		−10	6001·946	4	IIIA	0
5867·05 λ_1	3	IIIA	+10	6002·313	3	III	+10
5892·6	5	III	−42	6073·129*	1	III	−31
5900·433	5	III	−42·6	6133·580	3	III	+12
5905·788	4	III	−39	6137·392	4	III	−12·9
5921·206*	25	IA	−25·2	6165·339	3	IIIA	+17
5932·464	2	IIIA	+ϵ	6218·16	3	III	+12
5939·744	4	III	−19·7	6270·273	4	III	+10
5941·368	4	IIIA	−46·2	6283·910	3	IIA	−15
5948·61	2	IIIA	−10	6313·40	4	IIIA	−25
5955·843	2	IIA	+10	6431·695	7	IIIA	−15
5996·946	3	III	−ϵ		—		

* λ_1 and λ_2 are two close lines, one of them being a new line, whose separations have been measured by the authors and presented in Table 2. Out of these two lines if one could be classified, then only the unclassified line is listed there. The wavelengths marked with asterisks have been studied by earlier workers.

† Intensity of lines in a liquid air cooled hollow cathode lamp measured relative to assumed value of 100 for the most intense line in the table at 4913·408 Å.

Table 2—Separation of the New Lines from the Closest Listed Lines Measured in ^{144}Nd

Wavelength of the listed line λ (Å)	Separation† for ^{144}Nd (cm^{-1})	Intensity @ λ_1	Intensity @ λ_2	Wavelength of the listed line λ (Å)	Separation† for ^{144}Nd (cm^{-1})	Intensity @ λ_1	Intensity @ λ_2
4310·506‡	0·170	(3)	2	4880·469	0·403	(10)	3
4356·021	0·206	3	(2)	4886·36	0·220	2	(4)
4404·622	0·252	(24)	8	4911·362	0·634	7	2
4420·110	0·132	(3)	7	4929·10	0·583	2	(12)
4494·768*	0·305	3	8	4940·30	0·190	3	(12)
4499·66‡	0·068	2	4	4968·88	0·289	6	4
4505·011*	0·331	3	2	5046·16	0·221	17	8
4586·617	0·133	(33)	30	5096·51	0·081	4	(5)
4593·950	0·280	(5)	2	5097·723‡	0·100	5	8
4606·761	0·381	(2)	4	5127·199	0·610	(12)	3
4703·116	0·350	2	4	5151·00	0·075	8	8
4703·567	0·632	11	(14)	5156·04	0·137	7	3
4812·21	0·479	3	2	5191·43*	0·105	(8)	2
4828·58*	0·100	7	(3)	5606·632	0·251	4	3
4832·28	0·065	(10)	5	5734·274	0·253	4	(9)
4847·12	0·095	4	3	5773·89‡	0·310	3	2
4861·77‡	0·167	4	10	5806·41	0·096	1	3
4875·100	3·568	3	4	5867·05‡	0·250	3	(13)
4877·092	0·292	4	3	—			

* Lines of two different temperature classes falling at this wavelength (King[9]).

† The accuracy of measurement is usually ± 0·005 cm^{-1}.

@ $\lambda_2 > \lambda_1$. The λ's in parentheses are already classified lines and not listed in Table 1. The intensities are relative to assumed value of 100 for 4913·409 Å line listed in Table 1.

‡ Suspected doublet (King[9], Wyart[12]).

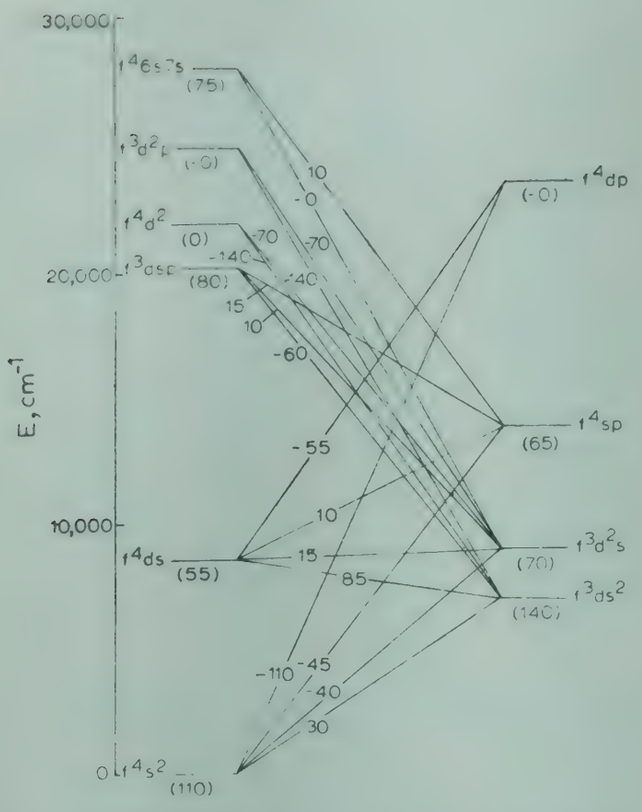

Fig. 3—Empirically expected isotope shift, Δ σ (142-144), in Nd I levels (in parentheses) and transitions (along the lines). Principal quantum number n for f, d, s and p are 4, 5, 6 and 6, respectively

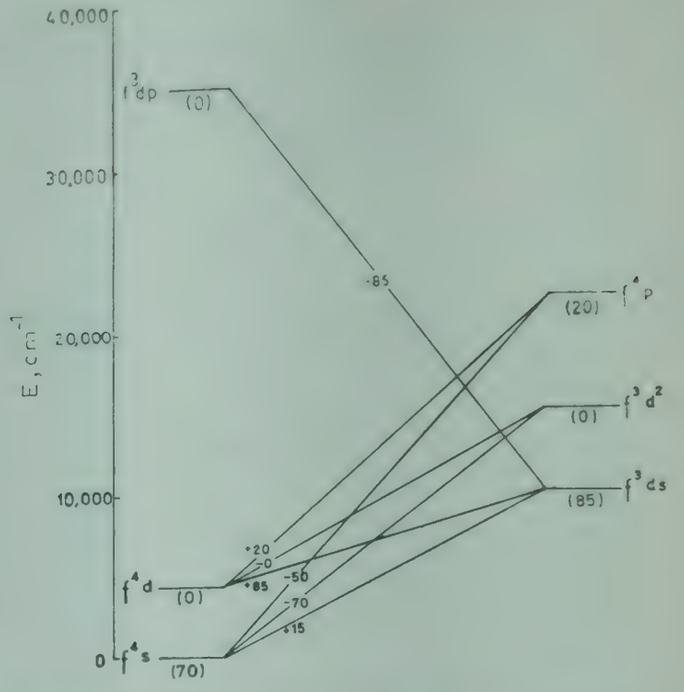

Fig. 4—Empirically expected isotope shift, Δ σ (142-144), in Nd II levels (in parentheses) and transitions (along the line). Principal quantum number n for f, d, s and p are 4, 5, 6 and 6, respectively

$4f^4 5d6p - 4f^4 6s^2$ and $4f^3 5d^2 6p - 4f^3 5d6s^2$ transitions, whereas smaller negative IS (~ -55 mK) are expected for transitions of the type $4f^4 5d6p - 4f^4 5d6s$ and $4f^3 5d6s6p - 4f^3 5d6s^2$. There are a large number of lines showing IS $\geqslant -70$ mK and in all probability they involve transitions from undiscovered high even levels to low odd levels of $4f^3 5d6s^2$ configuration. It is likely that energy levels of some new configurations are identified later which may involve the transitions for which the isotope shifts are reported here, and in that case the present data will be useful for confirmation of these new configurations. As for Nd II, there are very few unclassified lines encountered in the present study, and these appear to be transitions of $4f^4 6s - 4f^4 6p$ type.

The present isotope shift data which are mostly for lines of neutral neodymium atom will be helpful in identification of new high even and odd energy levels and further classification of the spectra. We are extending our measurements of isotope shift to ultraviolet and near infrared region and efforts are being made to identify new energy levels.

Acknowledgement

The authors are thankful to Dr N A Narasimham for his interest and to Shri A Venugopalan for his help.

References

1. Ahmad S A & Saksena G D, *Physica*, 85C (1977), 199.
2. Blaise J, Chevillard J, Verges J & Wyart J F, *Spectrochim. Acta*, 25B (1970), 333.
3. Klinkenberg P F A, *Physica*, 11 (1945), 327.
4. Korolev F A & Osipov I P, *Dokl. Akad. Nauk.* SSSR, 110 (1956), 365.
5. Rao P R & Gluck G, *Proc. R. Soc.*, A277 (1964), 540.
6. Saksena G D & Ahmad S A, *Technical Report*, (Bhabha Atomic Research Centre, Bombay) Rep. No. 290, 1967.
7. Ahmad S A, Saksena G D & Venugopalan A, *Indian J. pure appl. Phys.*, 14 (1976), 835.
8. *MIT Wavelength Tables*, (USA), Revised Edn, 1969.
9. King A S, *J. Astrophys.*, 78 (1933), 9.
10. Klinkenberg P F A, Dissertation, University of Amsterdam, 1955.
11. Hassan G E M A, *The atomic spectra of Nd I and Nd II*, Ph D thesis, University of Amsterdam, 1962.
12. Wyart J F, Thesis, University of Paris, 1968.

Indian Journal of Pure & Applied Physics
Vol. 18, February 1980, pp. 121-126

Simulated Inductance Using Operational Amplifiers

R S Sharma & N A Shah
Department of Physics, University of Kashmir, Srinagar 190 006

Received 12 *October* 1978; *revised received* 7 *May* 1979

Some circuits for realizing grounded inductors using operational amplifiers are reported. It is shown how the behaviour of such a solid state inductor differs from a passive inductor.

1. Introduction

A circuit designer may be interested in realizing an inductance suitable for integrated circuit applications. The object is to obtain a high inductance of high Q without serious stability and sensitivity problems. The purpose of this paper is to develop and investigate in detail the active circuits for realizing a grounded inductance and present a physical picture of the important parameters of the inductance as a function of the circuit components. These graphs can then be used for designing a solid state inductor.

2. Circuit I

The circuit under consideration is shown in Fig. 1 (a). Assuming the amplifier to be an ideal operational amplifier, one obtains the input impedance of the circuit as

$$Z_{11} = \frac{R_1 \{ R_4 + \omega^2 C^2 R_1 [R_2 R_3 + R_3 R_4 + R_2 R_4] + j\omega C (R_2 R_3 + R_3 R_4 + R_2 R_4 - R_1 R_4)\}}{R_4 (1 + \omega^2 C^2 R_1^2)} \quad ...(1)$$

In this expression substitute $R = \frac{R_2 R_3 + R_3 R_4 + R_2 R_4}{R_4}$ ...(2)

Then $Z_{11} = \frac{R_1 (1 + \omega^2 C^2 R_1 R) + j\omega C R_1 (R - R_1)}{1 + \omega^2 C^2 R_1^2}$ ...(3)

The condition for the inductive input impedance is $R > R_1$. The parameters of the simulated inductor are given by

$$\text{Inductance } L = \frac{C R_1 (R - R_1)}{1 + (\omega C R_1)^2} \quad ...(4)$$

$$\text{Series resistance } R_S = \frac{R_1 [1 + \omega^2 C^2 R_1 R]}{1 + (\omega C R_1)^2} \quad ...(5)$$

$$\text{Quality factor } Q = \frac{\omega C (R - R_1)}{1 + (\omega C)^2 R_1 R} \quad ...(6)$$

These expressions for the parameters of the inductor are the same as those of the circuit described by Berndt and Dutta Roy.[1] The latter circuit differs in that it has R_4 equal to infinite. The advantage of the present circuit over the circuit given by Berndt and Dutta Roy is that by choosing the values of R_2

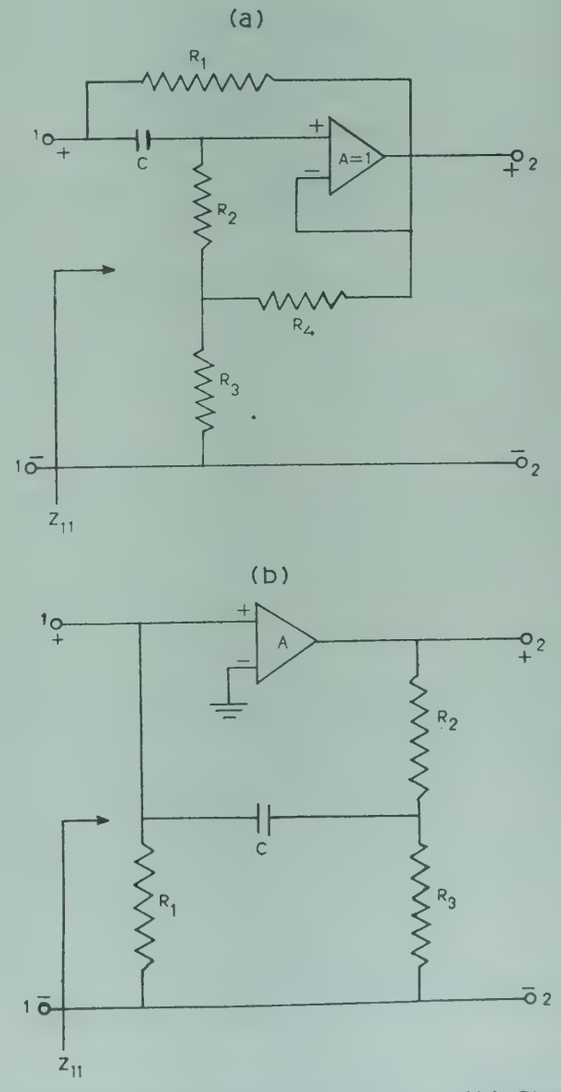

Fig. 1—Inductance simulation at the input [(a) Circuit I, (b) Circuit II]

and R_3 greater than that of R_4, one can realize a relatively higher value of R. For example, if $R_2 = R_3 = 10$ k Ω and $R_4 = 1$ k Ω, then from Eq. (2) $R = 120$ k Ω, whereas if R_4 is infinite, it is only 20 k Ω. In order to optimize Q, eon differentiates Q, wrt ωC and puts

$$\frac{\partial Q}{\partial \omega C} = 0 \text{ for a maximum.} \quad \text{This gives}$$

$$\omega C = \frac{1}{(R_1 R)^{1/2}} \qquad ...(7)$$

$$\frac{\omega L}{R} = \frac{1 - R_1/R}{1 + R_1/R} \left(\frac{R_1}{R} \right)^{1/2} \qquad ...(8)$$

$$\frac{R_s}{R_1} = \frac{2R}{R + R_1} \qquad ...(9)$$

$$Q = \frac{R - R_1}{2 (R R_1)^{1/2}} \qquad ...(10)$$

The dependences of $\omega L/R$, R_s/R_1, Q and $\omega C R$ on the ratio R/R_1 are given in Fig. 2. For getting a large value of Q, one must choose a large value of R/R_1. But a maximum value of Q need not necessarily be associated with a maximum value of the inductive reactance unlike with passive inductors. To demonstrate this, one writes Eq. (4) as

$$\omega L = \frac{\omega C R_1 (R - R_1)}{1 + (\omega C R_1)^2} \qquad ...(11)$$

Differentiate ωL wrt ωC and put $\frac{\partial \omega L}{\partial \omega C} = 0$ for a maximum.

This results $\omega C = 1/R_1$ ...(12)

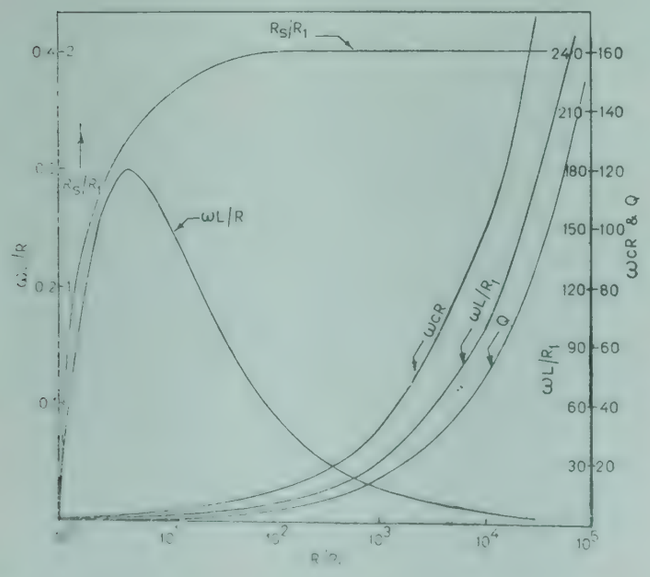

Fig. 2—Variation of $\omega L/R$, $\omega L/R_1$, Q, R_s/R_1 and $\omega C R$ with R/R_1 for the circuit of Fig. 1 (a)

From Eqs. (7) and (12), one obtains

$$\text{Ratio } \frac{f_{\max L}}{f_{\max Q}} = (R/R_1)^{1/2} \qquad (13)$$

where $f_{\max L}$ is the frequency corresponding to maximum inductive load and $f_{\max Q}$ is the frequency corresponding to maximum quality factor.

Larger the ratio R/R_1, bigger is the difference between the maxima of the inductive reactance and Q. For elaborating this point one takes up a numerical example with $C = 0{\cdot}05\ \mu F$; $R_1 = 15{\cdot}45$ k Ω and $R = 65{\cdot}48$ k Ω. The apparent inductance is 31·16 H at 100 Hz with $Q = 0{\cdot}78$. Here R_1 and R are such that Eq. (7) is satisfied. This inductance decreases with frequency as shown in Fig. 3. The dependance of ωL, R_s and Q with ωC are given in Fig. 4 (curves 1, 2 and 3 respectively). It is evident that the maximum of the reactance ωL is not accompanied with the maximum of Q. A large value of Q is associated with a smaller value of inductive reactance and vice versa. The inductive

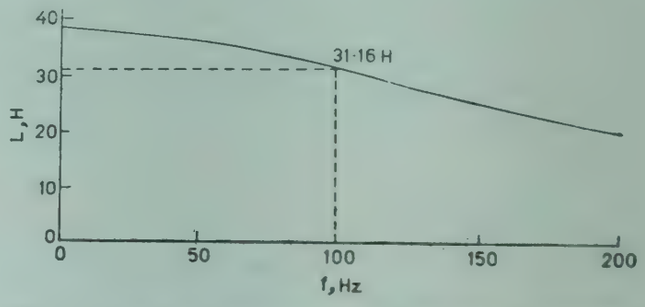

Fig. 3—Apparent inductance as a function of frequency

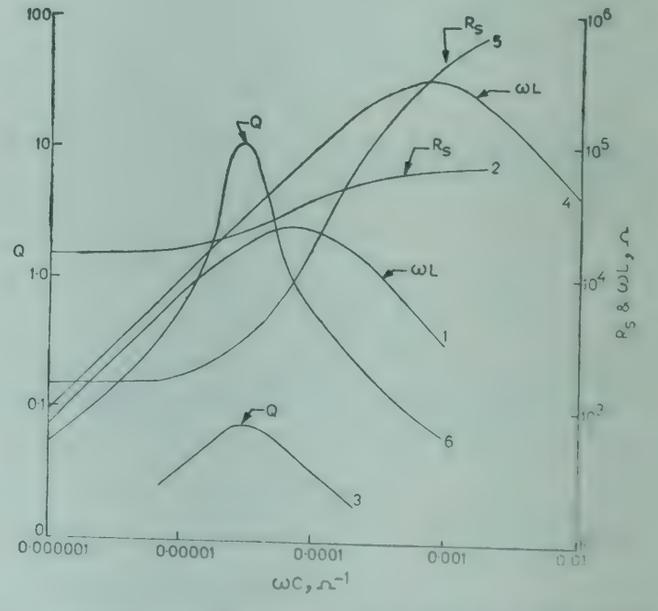

Fig. 4—Dependance of the reactance and Q of the inductor on frequency (arbitrary scale) for the circuit of Fig. 1 (a) [Curves 1-3 are for inductive reactance input and curves 4-6 are for capacitive reactance input]

reactance increases with frequency at low frequencies, eventually undergoes a maximum and finally decreases at higher frequencies. The frequency at which the inductive reactance becomes maximum shall henceforth be called as the optimum frequency f_0. It is the upper frequency limit up to which the performance of the simulated inductor is compatible with that of the passive inductor.

At frequencies above optimum frequency

$$\omega L \simeq \frac{R-R_1}{R_1 \omega C} \simeq \frac{1}{\omega C} \qquad ...(14)$$

The input reactance of this circuit has a capacitive value, i.e. it decreases with the increase of frequency. Fig. 4 (curves, 4, 5 and 6) shows the dependance of ωL, R_s and Q of the circuit with $R_1 = 1{\cdot}545$ k Ω and $R = 654{\cdot}8$ k Ω. It is evident from these curves that the optimum frequency has increased with the decrease of R_1. It is worth mentioning here that the separation between the maximum of ωL and that of Q has also increased by a factor of 10.

3. Circuit II

The circuit of Fig. 1 (b) uses an operational amplifier of gain A to realize a high inductance. The input impedance of this circuit is given by

$$Z_{11} = \frac{R_1 [R_2 + R_3 + j\,\omega\, c\, R_2\, R_3]}{R_2 + R_3 + j\omega C [R_2 R_3 + R_1 R_2 - R_1 R_3 (A-1)]} \qquad ...(15)$$

$$\text{Let } R_x = \frac{R_2 R_3}{R_2 + R_3} \qquad ...(16)$$

$$\text{and } \lambda = \frac{(A-1)\, R_x}{R_3} - \frac{R_x}{R_3} \qquad ...(17)$$

$$\text{Then } Z_{11} = \frac{R_1 [1 + j\omega C R_x]}{1 + j\omega C (R_x - \lambda R_1)} \qquad ...(18)$$

If one chooses $R_x = \lambda R_1$, the expression for the input impedance reduces to :

$$Z_{11} = R_1 + j\,\omega C R_1 R_x \qquad ...(19)$$

The apparent inductance is

$$L = C R_1 R_x = \lambda C R_1^2 \qquad ...(20)$$

and

$$Q = \omega C R_x = \omega C \lambda R_1 \qquad ...(21)$$

Unlike the circuit of Fig. 1 (a) this circuit yields a frequency independent inductor, i.e. its optimum frequency is infinite. Further the maximum of ωL and Q correspond to the same frequency. In this regard, the circuit properties do not differ from that of a passive inductor.

In general, R_x is not equal to λR_1. The relations giving the parameters of the simulated inductance are as follows

$$L = \frac{\lambda R_1^2 C}{1 + \omega^2 C^2 [R_x - \lambda R_1]^2} \qquad ...(22)$$

$$Q = \frac{\omega C \lambda R_1}{1 + \omega^2 C^2 R_x [R_x - \lambda R_1]} \qquad ...(23)$$

$$R_s = \frac{R_1 [1 + \omega^2 C^2 R_x (R_x - \lambda R_1)]}{1 + \omega^2 C^2 [R_x - \lambda R_1]^2} \qquad ...(24)$$

Following the process of optimization of Q as in the case of the circuit shown in Fig. 1 (a), one obtains from Eq. (23)

$$\omega C = \frac{1}{[R_x (R_x - \lambda R_1)]^{1/2}} \qquad ...(25)$$

Substituting the value of ωC from Eq. (25) in Eqs. (22), (23) and (24), one obtains

$$\frac{\omega L}{R_1} = \frac{1}{[R_x/\lambda R_1 - 1]\,[2 R_x/\lambda R_1 - 1]} \frac{R_x}{\lambda R_1} \qquad ...(26)$$

$$Q = \frac{1}{[R_x/\lambda R_1 - 1]^{1/2}} \frac{1}{2} \left(\frac{\lambda R_1}{R_x}\right)^{1/2} \qquad ...(27)$$

$$\frac{R_x}{R_1} = \frac{2 R_x}{\lambda R_1} \frac{1}{[2 R_x/\lambda R_1 - 1]} \qquad ...(28)$$

The dependance of $\omega L/R_1$, Q and R_s/R_1 on the ratio $R_x/\lambda R_1$ are given in Fig. 5. From this Fig. 5 it is

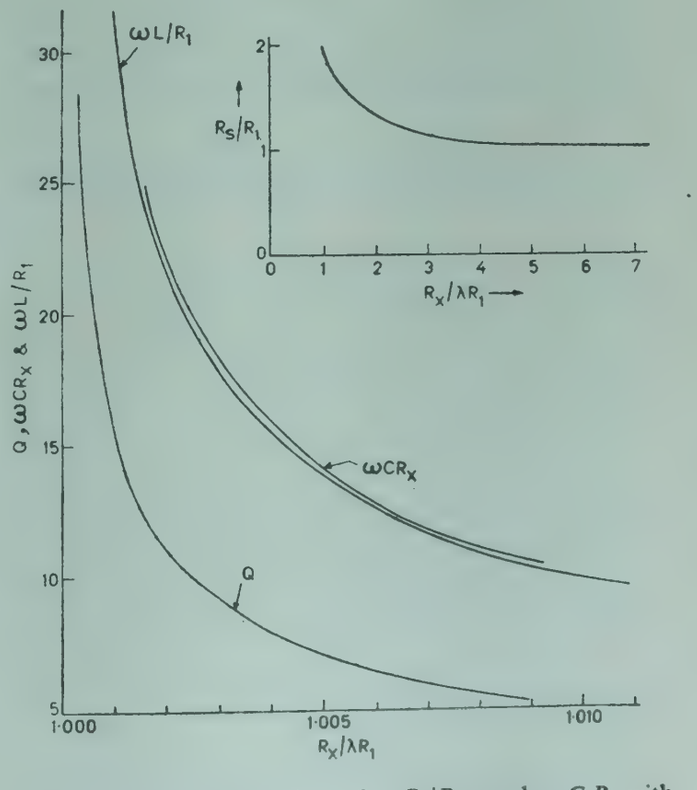

Fig. 5—Variation of $\omega L/R_1$, Q, R_s/R_1 and $\omega C R_x$ with $R_x/\lambda R_1$ for the circuit of Fig. 1 (b)

evident that a high apparent inductance with a high Q can be obtained with $R_x/\lambda R_1 = 1$. The behaviour of the circuit is similar to that of a passive inductor. In practice, it is difficult to realize $R_x = \lambda R_1$. As an example, let us choose $R_1 = 10$ k Ω, $R_2 = 200$ k Ω, $R_3 = 200$ k Ω and $A = 22$. This gives $R_x = 100$ k Ω and $\lambda = 10$ and the relation $R_x = \lambda R_1$ is satisfied. With $C = 0{\cdot}05$ μ F, an inductance of 50 H can be realized which is independent of frequency. In order to appreciate the effect of mismatching, let us take $A = 21{\cdot}98$ instead of 22. This yields $\lambda = 9{\cdot}99$. The variation of the input reactance of this circuit with frequency is given in Fig. 6. The reactance decreases with the increase of frequency at higher frequencies. In this case also there is a limited range of frequencies over which the operation of the active inductor is compatible with that of the passive inductor. The optimum frequency decreases as the ratio $R_x/\lambda R_1$ becomes greater than one. Thus for large values of $R_x/\lambda R_1$, the behaviour of the circuit shown in Fig. 1 (b) is in no way different from that of Fig. 1 (a). This is true for most of the circuits using operational amplifiers for realizing simulated inductance.[1-7] The optimum frequency thus becomes an important parameter of a solid state inductor and should be given in data sheet as specification of the solid state inductor if designed using an operational amplifier.

4. Circuit III

The circuit of Fig. 7 utilizes a unity gain operational amplifier to realize a grounded inductor. Assuming the operational amplifier to be an ideal one, the input impedance of this circuit can be expressed by

$$Z_{11} = \frac{(Z_1+Z_4)(Z_2Z_5+Z_2Z_3+Z_3Z_5)+Z_1Z_4(Z_3+Z_5)}{Z_4Z_5} \quad ...(29)$$

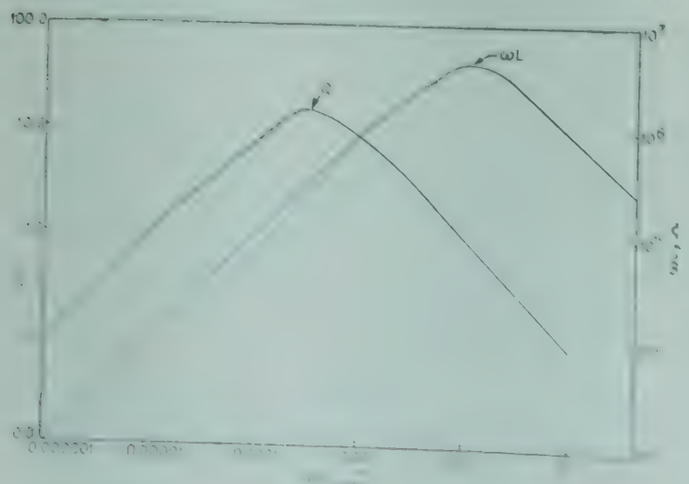

Fig. 6—Reactance and Q of the inductor as a function of frequency (arbitrary scale) for the circuit of Fig. 1 (b)

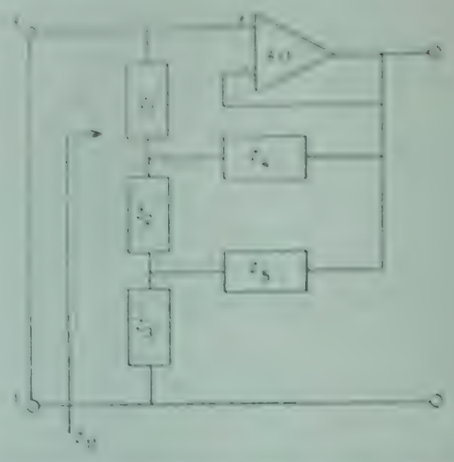

Fig. 7—Inductance simulation using unity gain operational amplifier (for circuit III)

This results in the realization of inductance if either Z_4 or Z_5 is chosen as capacitor and the other elements are taken as resistors.

Case I : Let us choose $Z_1 = R_1$; $Z_2 = R_2$; $Z_3 = R_3$; $Z_4 = X_c = 1/j\omega C$ and $Z_5 = R_5$ the expression for input impedance takes the form

$$Z_{11} = \frac{R_3R_5+R_2R_3+R_2R_5+R_1R_3+R_1R_5}{+j\omega C R_1(R_3R_5+R_2R_3+R_2R_5)} \quad ...(30)$$

The apparent inductance L, the quality factor Q and the series resistance R_s of this circuit are given by

$$L = \frac{C R_1(R_3R_5+R_2R_3+R_2R_5)}{R_5} \quad ...(31)$$

$$Q = \frac{\omega C R_1(R_3R_5+R_2R_3+R_2R_5)}{R_3R_5+R_2R_3+R_2R_5+R_1R_3+R_1R_5} \quad ...(32)$$

$$\text{and } R_s = \frac{R_3R_5+R_2R_3+R_2R_5+R_1R_3+R_1R_5}{R_5} \quad ...(33)$$

Case II : Let Z_5 be a capacitor and all other elements be resistors, then

$$Z_{11} = \frac{(R_1+R_4)(R_2+R_3)+R_1R_4}{R_4} + j\omega C \frac{R_1R_2R_3+R_1R_3R_4+R_2R_3R_4}{R_4} \quad ...(34)$$

The apparent inductance L, the quality factor Q and the series resistance R_s are given by

$$L = \frac{C[R_1R_2R_3+R_1R_3R_4+R_2R_3R_4]}{R_4} \quad ...(35)$$

$$Q = \frac{\omega C[R_1R_2R_3+R_1R_3R_4+R_2R_3R_4]}{(R_1+R_4)(R_2+R_3)+R_1R_4} \quad ...(36)$$

$$\text{and } R_s = \frac{(R_1 + R_4)(R_2 + R_3) + R_1 R_4}{R_4} \quad \ldots(37)$$

Case III : An interesting case arises if both Z_4 and Z_5 are capacitances. Let $Z_1 = R_1, Z_2 = R_2, Z_3 = R_3$, $Z_4 = Z_5 = X_C = 1/j\omega C$, then Eq. (29) reduces to

$$Z_{11} = R_1 + R_2 + R_3 - \omega^2 C^2 R_1 R_2 R_3 + j\omega C [R_1 R_2 + 2R_1 R_3 + R_2 R_3] \quad \ldots(38)$$

The effective inductance, quality factor and series resistance are given by

$$L = C [R_1 R_2 + 2R_1 R_3 + R_2 R_3] \quad \ldots(39)$$

$$Q = \frac{\omega C [R_1 R_2 + 2R_1 R_3 + R_2 R_3]}{R_1 + R_2 + R_3 \quad \omega^2 C^2 R_1 R_2 R_3} \quad \ldots(40)$$

$$\text{and } R_s = R_1 + R_2 + R_3 - \omega^2 C^2 R_1 R_2 R_3 \quad \ldots(41)$$

The real part of Z_{11} becomes zero at a frequency

$$\omega_0 = \frac{1}{C}\left[\frac{R_1 + R_2 + R_3}{R_1 R_2 R_3}\right]^{1/2}$$

One obtains an apparent inductance with infinite quality factor at this frequency. At a frequency greater than ω_0 the circuit behaves a frequency dependent negative resistance (FDNR) is series with an inductance.

5. Circuit IV

The circuit of Fig. 8 also utilizes an operational amplifier of gain unity for the simulation of an inductance. One can write an expression for input impedance of this circuit as

$$Z_{11} = \frac{(Z_1 + Z_2)(Z_4 Z_5 + Z_3 Z_5 + Z_3 Z_4) + Z_1 Z_2 (Z_3 + Z_5)}{Z_2 Z_3} \quad \ldots(42)$$

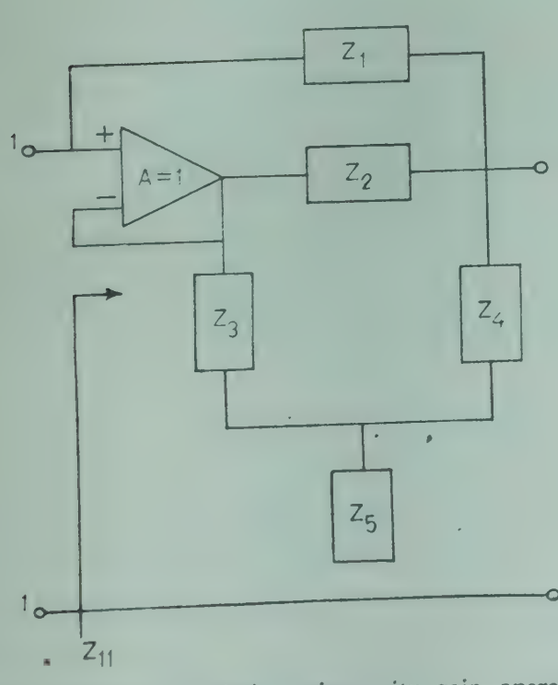

Fig. 8—Inductance simulation using unity gain operational amplifier (for circuit IV)

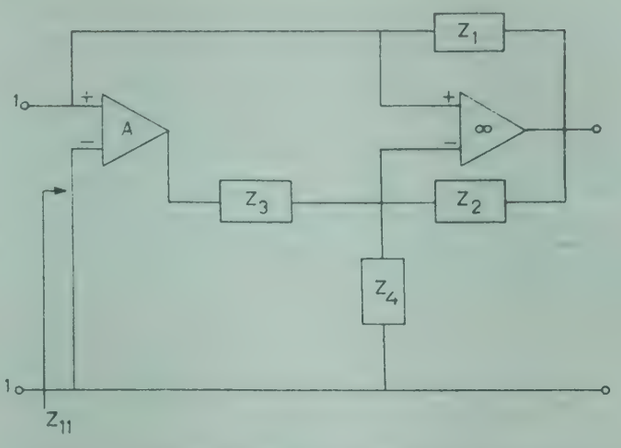

Fig. 9—Inductance simulation using two operational amplifiers

This circuit (Fig. 8) also results in the simulation of a grounded inductance and the results obtained from the circuit of Fig. 7 hold good for this circuit if Z_4 and Z_5 are interchanged with Z_2 and Z_3 respectively. Although the circuit of Fig. 8 is basically different from that of Fig. 7 in configuration, it is an equivalent of the first circuit.

6. Circuit V

The circuit of Fig. 9 utilizes two operational amplifiers, one of finite gain A and the other of infinite gain. Assuming ideal operational amplifiers of infinite input impedance, one can write the input impedance of the circuit as

$$Z_{11} = \frac{Z_1 Z_3 Z_4}{Z_2 [Z_4 (A-1) - Z_3]} \quad \ldots(43)$$

Let us choose $Z_1 = R_1$; $Z_2 = X_c = 1/j\omega C$, $Z_3 = R_3$ and $Z_4 = R_4$, then the input impedance of the circuit is given by

$$Z_{11} = j\omega C \frac{R_1 R_3 R_4}{R_4 (A-1) - R_3} \quad \ldots(44)$$

The apparent inductance of this circuit is $\frac{C R_1 R_3 R_4}{R_4 (A-1) - R_3}$ with infinite Q. If $R_3 = R_4 (A-1)$, then the apparent inductance is infinite with infinite Q. A high value of grounded inductance with zero series resistance can thus be realized by using a low gain operational amplifier along with an infinite gain amplifier.

7. Conclusions

Both the circuits reported can be used for realizing grounded inductance for low frequency applications. At higher frequencies, the input reactances

of these circuits decrease with increasing frequencies. In such cases, it is necessary to specify the optimum frequency of the active inductor which is defined here as the frequency over which the operation of the active inductor is compatible with that of a passive inductor. The active circuits using operational amplifiers for realizing frequency independent grounded inductors of high quality factor, are functional.

References

1. Berndt D & Dutta Roy S C, *IEEE J. Solid St. Circ.*, SC-4 (1969), 161.
2. Dutta Roy S C & Nagarajan V, *IEEE J. Solid St. Circ.*, SC-5 (1970), 95.
3. Ryder J D, *Electronic fundamentals and applications* (Prentice Hall, New Jersy), 1976, 247.
4. Patranabis D, *Int. J. Electron*, 28 (1970), 481.
5. Keen A W & Peters J L, *Electronics Lett.*, 3 (1967), 136.
6. Orchard H J & Wilson A N, *Electronics Lett.*, 10 (1974), 261.
7. Prestcott A J, *Electronics Lett.*, 2 (1966), 283.

Communications

Low Angle X-Ray Diffraction Study of Liquid Crystal : Cholesteryl Methyl Carbonate

J Shashidhara Prasad & L Siddarame Gowda

Department of Physics, University of Mysore
Mysore 570 006

Received 13 *September* 1979

A low angle X-ray diffraction study of cholesteryl methyl carbonate reveals scattering curve features which closely resemble the curves of ordered semi-crystalline polymers, a characteristic feature of which is the existence of long periods. The compound in the solid crystalline state consists of amorphous and crystalline components, the number and size of which are approximately equal.

The study of materials which are capable of forming liquid crystals has gained immense importance in recent years due to their wide variety of applications. The variety of properties exhibited by liquid crystals are associated not only with the chemical constitution of the molecular chains but also to a great extent with their structural characteristics. A systematic study of the molecular structure in the crystalline state for the mesogenic materials provides us with a deeper understanding of the nature of transitions into the liquid crystalline state, as well as about the physical properties[1,2] which in turn will enable us to select or modify the molecular structure to suit our requirements. In view of this, a project has been undertaken to determine the crystal structures of a series of mesogenic materials. As a part of the project, low-angle-X-ray diffraction study of liquid crystals has been undertaken. Presently we have studied cholesteryl methyl carbonate (CMC), a compound of cholesterol-forming liquid crystals of the cholesteric type, in the solid crystalline phase. Investigations of this type are

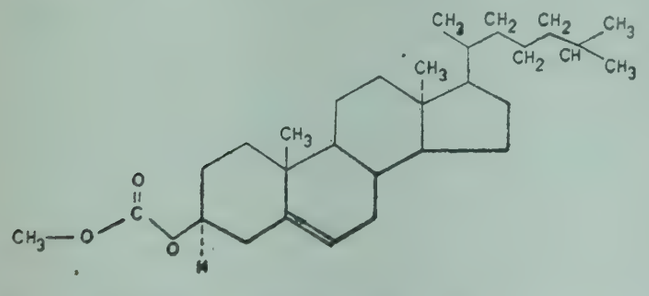

Fig. 1—Structure of Cholesteryl methyl carbonate molecule

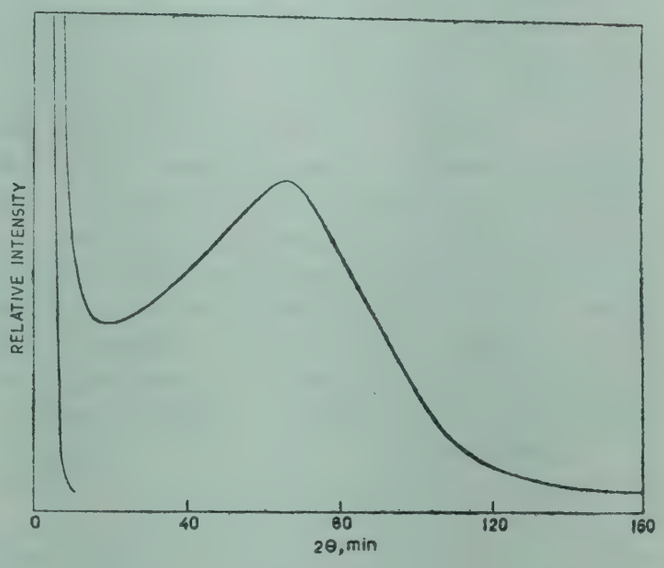

Fig. 2—Low angle scattering curve of cholesteryl methyl carbonate

quite useful for they enable us to determine and describe the nature of submicroscopic inhomogeneities of the substance.

The mesogenic CMC melts into the liquid crystalline state at 110°C and into an isotropic liquid at 114°C. The structural formula of the material is shown in Fig. 1. The powdered solid crystalline material was melted and the isotropic melt was poured into a metallic annular ring on either side of which were mica windows. After crystallization, these were placed in the low angle scattering camera. The low angle scattering photographs were obtained using X-ray films (Indu) in a Rigaku Denki LASG6 installation with point collimation using Cu-K_α radiation with nickel filter. The angular characteristics of the diffraction patterns were evaluated using the Carl-Zeiss-Jena GII and GIII microdensitometer and potentiometric recorder.

Results—Fig. 2 illustrates the intensity distribution of low angle scattering evaluated from the photographs. The diffraction data of the molecules represent a superposition of continuous curve due to an amorphous phase and a peak corresponding to the molecules aligned in a crystalline array. This suggests that certain proportion of the crystallites occur in the oriented state. The shape of the scattering for the solid crystalline state is very nearly

similar to those obtained for ordered semi-crystalline polymers in major features. The characteristics of such a system is the existence of long periods. The long period may be expected to be due to the density heterogeneity that occurs due to the alterations of amorphous and crystalline regions.[3-6] It will not be unreasonable to assume that the appearance of the long periods on the low angle scattering patterns of solid crystalline material is also due to the alteration of less ordered amorphous regions with more ordered crystalline regions. The crystalline intensities sample a continuous molecular transform of the substituent molecules, where as the amorphous scattering gives a spherically average continuous transform. As such, it is possible to evaluate the fractional composition of amorphous and crystalline regions. The order of the long period was estimated from the angular positions of the reflections, by interpolating a smooth curve to separate the sharp reflection from diffuse scattering. The sharpness of the maximum may be due to the existence of domains in the unoriented solid crystal in which the long axes of the molecules are all pointed along a single axis. The long period was estimated to be 119·2 Å. By using the methods of Tsvankin,[7] the corrected period turned out to be 143·2 Å, the length of the crystalline part was found to be nearly equal to that of the amorphous part, each being equal to 71·6 Å. By altering the conditions of preparation of the samples, it was verified that the amorphous regions did not show any appreciable dependence on the rate of cooling or surface effects.

The results are almost identical to those obtained for the case of cholesteryl acetate[8] which has a molecular formula not very much different from that of CMC, except for a slight change in the end group, viz. cholesteryl acetate $-CH_3-\overset{\overset{O}{\|}}{C}-O-R$. and

cholesteryl methyl carbonate $CH_3-O-\overset{\overset{O}{\|}}{C}-O-R$.

The investigation shows that the mesogenic material under investigation, in the solid crystalline state consists of amorphous and crystalline regions, the number and size of which are approximately equal.

References

1. Shashidhara Prasad J, *Acta Crystallogr.*, **35B** (1979), 1404.
2. Shashidhara Prasad J, *Acta Crystallogr.*, **35B** (1979), 1407.
3. Hess K & Kissig N, *Kolloid Z.*, **130** (1953), 10.
4. Nizamidinov S A & Slutsker A I, *Vysokomol Soed*, **A10** (1968), 1148.
5. Hoseman R, *Polymer*, **3** (1962), 349.
6. Tsvankin D YA, *Vysokomol Soed*, **6** (1964), 2078.
7. Tsvankin D YA, *Vysokomol Soed*, **6** (1964), 2087.
8. Dutchak YA L, Mikityuk Z M & Fedyshin M I, *Soviet Phys. Crystallogr.*, **21** (1976), 705.

Notes

Lattice Vibration Modes in CdS

HITOSHI KANAMORI, MASAO MATSUMOTO*, KEI URABE** & NOBUYUKI NAKAMORI

Department of Electrical Engineering, Kyoto Technical University, Matsugasaki, Sakyo-ku, Kyoto 606, Japan

Received 1 *May* 1979; *revised received* 24 *September* 1979

For long-wavelength lattice vibrations in CdS, the normal coordinates of all the vibration modes are derived and briefly schematized. The force constants are derived. The frequencies of the optically inactive B_1-modes are predicted.

Frequencies of long-wavelength lattice vibrations in CdS have been determined using the infrared measurments[1-4] and the Raman spectroscopy.[5-7]

In this note, we have presented the force constants and the normal coordinates of vibration modes in CdS by the use of the *GF*-matrix method, and the predicted frequencies of inactive $2B_1$ modes.

CdS crystallizes to the wurtzite-type crystals with space group C_{6v}^4 ($P6_3mc$). The factor group analysis of the unit cell containing two formulae units yields $2A_1 + 2B_1 + 2E_1 + 2E_2$, where $A_1 + E_1$ species correspond to the acoustic vibration modes, $A_1 + E_1 + 2E_2$ species to Raman-active modes and $A_1 + E_1$ to infrared active modes. The $2B_1$ modes are optically inactive.

Fig. 1 shows the unit cell of the wurtzite-type crystal, containing two formulae units. The cartesian coordinates (x_n, y_n, z_n) $(n = 1$ to $4)$ are set to denote the displacements of nth atom, parallel to the crystallographic (x, y, z)-axes.

The symmetry coordinates are given as follows:

$$(2A_1)\ s_1 = (z_1 + z_2)/\sqrt{2}, \qquad s_2 = (z_3 + z_4)/\sqrt{2} \quad \ldots(1)$$

$$(2B_1)\ s_3 = (z_1 - z_2)/\sqrt{2}, \qquad s_4 = (z_3 - z_4)/\sqrt{2} \quad \ldots(2)$$

$$(2E_1)\ \left.\begin{aligned} s_{5a} &= (x_1 + x_2)/\sqrt{2}, & s_{5b} &= (y_1 + y_2)/\sqrt{2} \\ s_{6a} &= (x_3 + x_4)/\sqrt{2}, & s_{6b} &= (y_3 + y_4)/\sqrt{2} \end{aligned}\right\} \quad \ldots(3)$$

$$(2E_2)\ \left.\begin{aligned} s_{7a} &= (x_1 - x_2)/\sqrt{2}, & s_{7b} &= (y_1 - y_2)/\sqrt{2} \\ s_{8a} &= (x_3 - x_4)/\sqrt{2}, & s_{8b} &= (y_3 - y_4)/\sqrt{2} \end{aligned}\right\} \quad \ldots(4)$$

where s_{ia} and s_{ib} respectively transform according to the first and second rows of the doubly degenerate E-representations. From the symmetry coordinates, we can construct a U-matrix as the example shown in Ref. 8 [Eq. (9)].

For the calculation due to the *GF*-matrix method, we put two kinds of bond stretching coordinates, two kinds of valence angle bending coordinates, and their relevant force constants, which are shown in Table 1. In Table 1, the labels of atoms in Fig. 1 are used to specify the bonds and angles. By inserting the four observed frequencies of the $A_1 + E_1 + 2E_2$ modes into the eigen values of the secular determinant shown in Ref. 8 [Eqs. (10)-(12)], we have solved the four force constants. From the force constants we have predicted the two frequencies of the inactive B_1 modes.

The observed and predicted frequencies are listed in Table 2. The values of force constants are shown in the fourth column in Table 1.

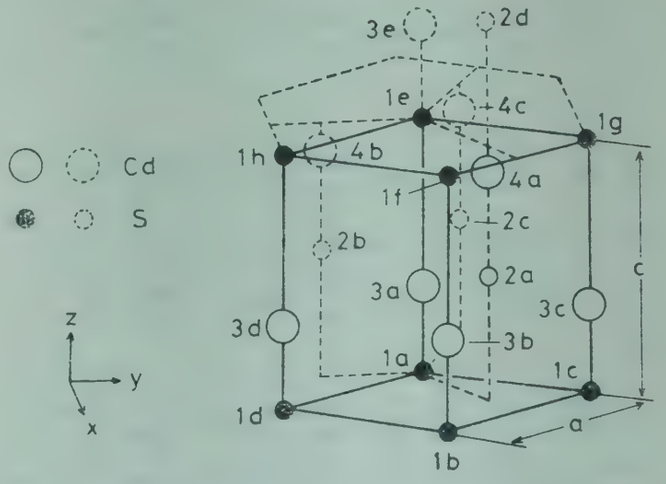

Fig. 1—The crystal structure of CdS [The unit cell is drawn by the bold full lines.]

Table 1—Bond Stretching Coordinates (Δr), Their Relevant Force Constants (K), Valence Angle Bending Coordinates ($\Delta\alpha$) and Their Relevant Angle Bending Force Constants (H)

End atoms of bonds Δr and angle-forming atoms of $\Delta\alpha$	Number of coordinates	Force constants	Estimated value (mdyne/Å)
$1a-3a$, $2a-4a$	2	K_1	0·490
$3a-1e$, $4a-2d$	2	K_2	0·539
$3a-2a-3b$, $3b-2a-3c$, etc.	12	H_1	0·167
$1a-3a-2a$, $1a-3a-2b$, etc.	12	H_2	−0·114

*Present address: Naka Works, Hitachi Ltd, Katsuta-shi, Ibaraki 312, Japan

**Present address: Industrial Products Research Institute, Yatabe-machi, Iabaraki 305, Japan

We express the normal coordinates as the linear combination of the symmetry coordinates as

$$\left.\begin{aligned} Q_1 &= \sqrt{2}\,(-a_1 s_1 + a_2 s_2) \\ Q_2 &= \sqrt{2}\,(a_2 s_1 + a_1 s_2) \end{aligned}\right\} \text{for } A_1 \text{ modes} \quad \ldots(5)$$

$$\left.\begin{aligned} Q_3 &= \sqrt{2}\,(-a_3 s_3 + a_4 s_4) \\ Q_4 &= \sqrt{2}\,(a_4 s_3 + a_3 s_4) \end{aligned}\right\} \text{for } B_2 \text{ modes} \quad \ldots(6)$$

$$\left.\begin{aligned} Q_{5a} &= \sqrt{2}\,(-a_1 s_5 + a_2 s_7) \\ Q_{5b} &= \sqrt{2}\,(-a_1 s_6 + a_2 s_8) \\ Q_{6a} &= \sqrt{2}\,(a_2 s_5 + a_1 s_7) \\ Q_{6b} &= \sqrt{2}\,(a_2 s_6 + a_1 s_8) \end{aligned}\right\} \text{for } E_1 \text{ modes} \quad \ldots(7)$$

$$\left.\begin{aligned} Q_{7a} &= \sqrt{2}\,(a_5 s_9 + a_6 s_{11}) \\ Q_{7b} &= \sqrt{2}\,(a_5 s_{10} + a_6 s_{12}) \\ Q_{8a} &= \sqrt{2}\,(a_6 s_9 - a_5 s_{11}) \\ Q_{8b} &= \sqrt{2}\,(a_6 s_{10} - a_5 s_{12}) \end{aligned}\right\} \text{for } E_2 \text{ modes} \quad \ldots(8)$$

Table 2—Observed and Predicted Frequencies of Lattice Vibration Modes (cm^{-1})

Mode	Obs. (Ref. 7)	Predict
ν_1 (A_1)	234	
ν_2 (A_1)	acoustic	
ν_3 (B_1)	——	208
ν_4 (B_1)	——	107
ν_5 (E_1)	243	
ν_6 (E_1)	acoustic	
ν_7 (E_2)	252	
ν_8 (E_2)	44	

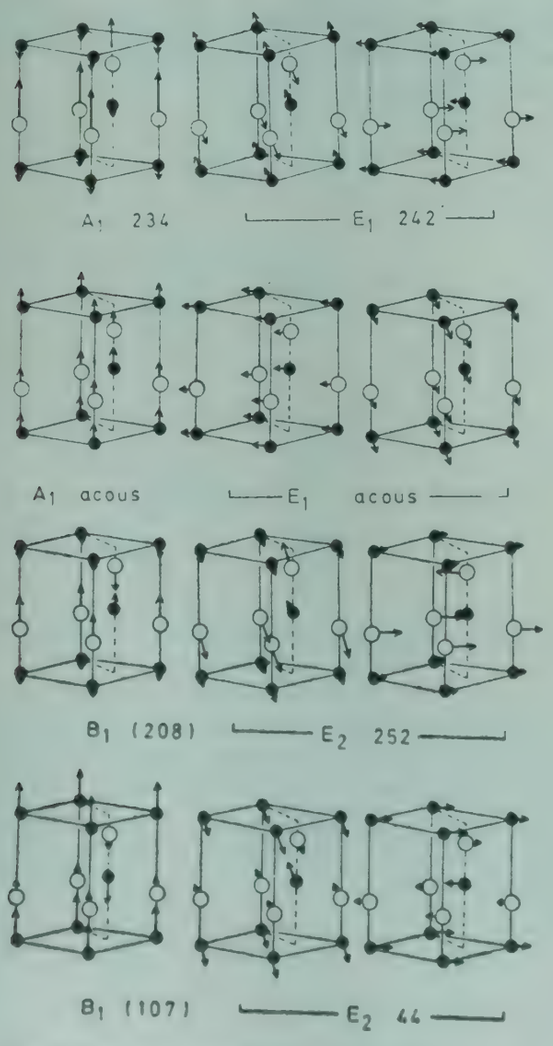

Fig. 2—Brief schemes of the normal modes in CdS

Table 3—Coefficients in Normal Coordinates in Eqs. [(5)-(8)]

a_1	0·471	a_4	0·988
a_2	0·882	a_5	0·316
a_3	0·156	a_6	0·949

The coefficients a's which indicate the relative amplitudes of atomic motion in each mode, can be derived from the eigen vectors of the secular determinants [Eq. (13) in Ref. 8]. The values of a's are listed in Table 3.

For example, the normal coordinate of 234 cm^{-1} A_1 mode is

$$Q_1 = -0{\cdot}471\,(z_1 + z_2) + 0{\cdot}882\,(z_3 + z_4)$$

The brief schemes of all the normal coordinates in CdS are depicted in Fig. 2, the predicted frequencies of B_1 modes being within parentheses.

References

1. Collins R J, *J. appl. Phys.*, 30 (1959), 1135.
2. Balkanski M & Besson J M, *J. appl. Phys.*, 32 (1961), 2293.
3. Marshall R & Mitra S S, *Phys. Rev.*, 134 (1964), A1019.
4. Balkanski M, Besson J M & Letoullec R, *Int. Conf. on Semiconductors*, Paris (Academic Press, New York), 1964, 1091.
5. Poulet H & Mathieu J P, *Annls Phys. (Paris)*, 9 (1964), 549.
6. Tell B, Damen T C & Porto S P S, *Phys. Rev.*, 144 (1966), 771.
7. Arguello C A, Rousseau D L & Porto S P S, *Phys. Rev.*, 181 (1969), 1351.
8. Matsumoto M, Urabe K & Kanamori H, *Indian J. pure appl. Phys.*, 16 (1978), 263.

Estimation of Sodium Content of Cotton for Use in Neutron Activation Dosimetry

P K Marathe, H K Kundu & G Venkataraman

Division of Radiological Protection, Bhabha Atomic Research Centre, Trombay, Bombay 400 085

Received 13 *November* 1978; *revised received* 22 *March* 1979

Sodium activation by neutrons can be used to estimate neutron fluences. It has been shown that clothing of an exposed individual can serve as an activation detector in case of reactor and criticality accidents. For this purpose, pieces of different types of clothing were exposed to thermal neutrons from the CIRUS reactor and the gamma ray spectrum after irradiation was studied. The results showed that clothing contains sodium to an extent of 10^{-2} % by weight at a thermal neutron flux level of $4{\cdot}1 \times 10^9$ n/cm²/sec.

There is always a likelihood that a person working in a nuclear reactor or fuel reprocessing plant may receive a high neutron dose (flux) in an accident. Persons exposed to high fluxes of neutrons may suffer the ill effects of radiation exposure and unless prompt medical attention is given they may even lose their lives. Therefore, several detector systems have been developed which are either carried on the body of the person or kept near the workspot. Most of the detectors are based on the activation principle so that in the event of an accident one measures the induced activity in the detector—thereby getting an idea of the dose — and initiates appropriate medical follow-up. But it has been the sad experience in many cases that when an accident had really taken place, persons exposed to radiation were not having their personal monitors and other systems were not available in the vicinity. Therefore, investigators had to resort to counting the induced radioactivity of hair, nails, gold fillings of teeth of the people or activation of the blood or induced activity in the coins or pens carried by people, etc. This note extends the field of measurements to include the induced activity of the clothing of the exposed individual.

For this purpose pieces of clothing like coloured cloth, boiler suits, socks were exposed to thermal neutrons from the CIRUS reactor which is operated at 40 MW. The gamma ray spectrum was studied using a 3 in. diam. × 3 in. thick NaI (Tl) crystal and a 400-channel analyzer. The spectrum is shown in Fig. 1. The gamma ray spectrum shows the two lines at 1·36 and 2·76 MeV indicating the presence of ^{24}Na. This was also confirmed by half-life measurements. The ^{24}Na activity arises through ^{23}Na (n, γ) ^{24}Na capture reaction.

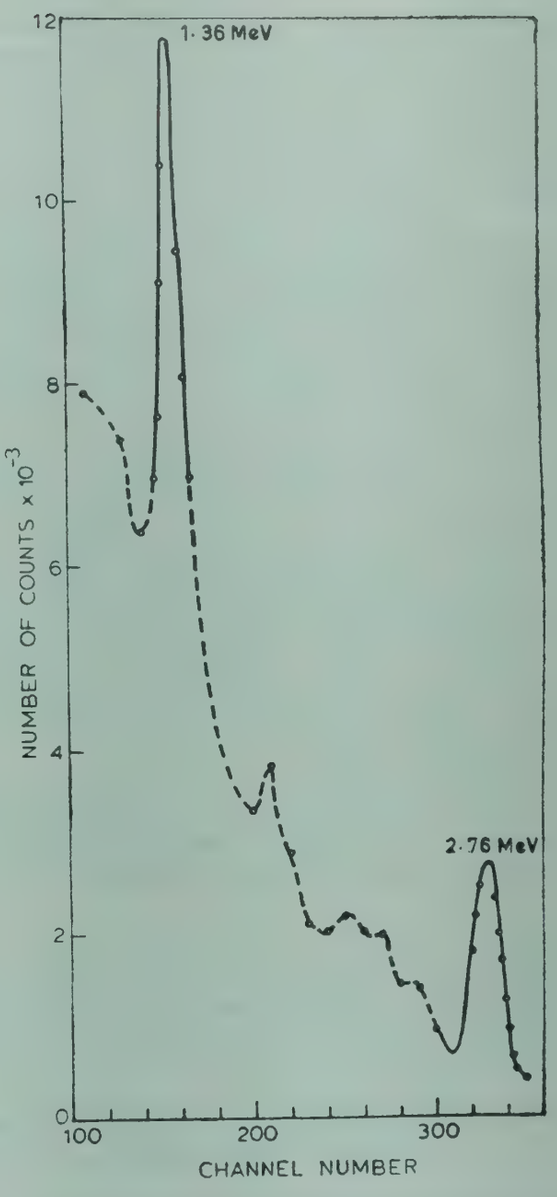

Fig. 1—Gamma-spectrum of neutron-activated cotton sample

The number of ^{23}Na atoms present in the sample is given by

$$N_{Na} = \frac{C}{\epsilon} \times \frac{1}{\sigma \phi t (1-e^{-\lambda\tau}) e^{-\lambda t_1}}$$

and the percentage, by weight, of sodium per gramme of cloth is

$$\text{Na } \% = \frac{N_{Na}}{W} \times \frac{23}{6{\cdot}02 \times 10^{23}} \times 100$$

where τ is the period of irradiation in seconds in the reactor, λ the decay constant of ^{24}Na in sec^{-1}, t_1 the period (in seconds) elapsed after irradiation before the start of counting, t the time interval of counting in seconds, C the number of counts observed under the photopeak (2·76 MeV) per unit time, ϵ the photopeak efficiency for the NaI (Tl) crystal for this energy, σ the thermal neutron cross-section for the ^{23}Na(n, γ) ^{24}Na reaction, ϕ the thermal neutron flux used and W the weight of the cloth used, $6{\cdot}02 \times 10^{23}$ the Avogadro number and 23 the atomic weight of sodium. The photopeak efficiency used was taken from Ref. 1.

Samples were irradiated for periods ranging from 20 to 50 hr. Values of 0·054 and 0·54 barns were used for ϵ and σ respectively. The thermal neutron flux was measured with the help of gold foils and found to be $4{\cdot}1 \times 10^9$n/cm^2/sec. All samples used in the experiment had weight around 1 g.

The various pieces of clothing showed an average sodium content of $(1 \pm 0{\cdot}2) \times 10^{-2}$ %. The cloth samples were mostly used ones. Before the experiment, the samples were washed in distilled water and heat dried. The sodium content, therefore, must be due to the intrinsic sodium content of the cotton

Table 1—Sodium Content of Cotton and Cloth Samples

	Variety	Sodium Content, wt % × 10^2
Cotton	Hybrid - 4	0·73
	Sanjay	0·90
	Sankar Palej	0·71
	Jaydhar	0·90
Cloth	White socks	0·85
	Yellow duster	1·07
	Blue boiler suit	1·34

or dye used and not due to any detergent or human sweat.

For the sake of completeness, samples of raw cotton were also irradiated. These samples were obtained from various parts of India. Most of the seven samples studied showed the same order of sodium content as that of clothing, whereas other varieties showed a much lower content. The results are presented in Table 1.

Therefore, the clothing worn by personnel working in reactors and critical assemblies can serve as an activation neutron monitoring detector.

References

1. Rangarajan C, Mishra U C, Smt Gopalakrishnan S & Sadasivan S, *Analysis of complex* NaI (Tl) *gamma-spectra from mixtures of nuclides*, BARC Rep., 686, 1973.

Effect of High Pressures on the Hydrogen Bond Systems of Some Alcohols

A Srinivasa Rao

Department of Physics, Jawaharlal Institute
Pondicherry 605 006

Received 17 *February* 1979

A formula expressing the dependence of the fraction of intact hydrogen bonds (α_p) on the external pressure is derived for hydrogen-bonded liquids using the Ising model. The parameter α_p is found to increase with increase of pressure for methyl, ethyl and *n*-propyl alcohols. The agreement between the theoretical values of α_p and the values obtained from the experimental data on viscosity at high pressures in these alcohols appears to be reasonably good till α_p attains a value of 0·95. Further increase of pressure seems to result in compression of the hydrogen bonds in these alcohols instead of increasing the hydrogen bond association parameter α_p.

In an earlier communication,[1] we obtained an expression for the fraction of intact hydrogen bonds (α) in hydrogen-bonded liquids using the Ising model at ordinary pressures assuming that the thermal energy breaks hydrogen bonds without altering the hydrogen-bond energy. The viscosity of hydrogen-bonded liquids such as ethyl alcohol increases with increase of pressure and this has been qualitatively attributed[2] to the increase of α with increase of pressure. In this note, an attempt has been made to obtain a theoretical expression for the parameter (α_p) as a function of pressure and temperature using the Ising model.

In our earlier paper,[1] the Helmholtz's free-energy F for the hydrogen bond system of a liquid was calculated using the Ising model and the parameter α was obtained minimizing F. To obtain the dependence of α on external pressure P, it would become necessary to calculate the Helmholtz free-energy H and minimize the same to obtain thermal equilibrium condition.

The Gibb's H can be written as

$$H = E - TS + PV \qquad ...(1)$$

where the symbols have their usual meaning. The first two terms in Eq. (1) were already calculated in our earlier paper[1] and hence it becomes necessary only to calculate the PV term to obtain the Helmholtz's H. To obtain the PV term, we shall assume that the volume V is given by

$$V = V_0 [1 - (n - n_0) C'] \qquad ...(2)$$

where V_0 is the molar at zero pressure, n_0 the number of intact hydrogen bonds at zero pressure, n the number at any pressure P and C' a constant. As the pressure P is increased, n will increase resulting in a decrease of volume. The PV term of Eq. (1) can be rewritten as

$$PV = PV_0 - PV_0 C' n + PV_0 n_0 C'$$
$$= PV_0 - PCn + Pn_0 C \qquad ...(3)$$

where, $V_0 C' = C$, a new constant, which has the dimensions of volume. Following our earlier procedure[1] and using the condition that $\partial H/\partial n = 0$ for thermal equilibrium, we can obtain that

$$\alpha_p = \tanh\left[\frac{E_H + CP}{4 k_B T}\right] \qquad (4)$$

where α_p is the fraction of intact hydrogen bonds at P, E_H is the hydrogen-bond energy, k_B the Boltzmann's constant and T the absolute temperature. It should be mentioned that in this theoretical model, it is tacitly assumed that the effect of temperature and pressure is to alter the number of intact hydrogen bonds and the hydrogen-bond energy E_H essentially remains the same at all temperatures and pressures and this assumption is reasonable as it is known that hydrogen bonds in liquids resist compression.[3]

To test the validity of the formula given by Eq. (4), it is necessary to obtain the value of C. Bridgman[4] measured the viscosity η of methyl and ethyl alcohols and found that the viscosity increases with pressure for both these alcohols. It has already been shown[5] that the vicosity η of a hydrogen bonded liquid is given by the equation

$$\eta = A \exp(\alpha E_H/RT) \quad ...(5)$$

where, E_H is the hydrogen bond energy, R the gas constant and T the absolute temperature. Eq. (5) can be modified for higher external pressures as

$$\eta_p = A \exp(\alpha_p E_H/RT) \quad ...(6)$$

where η_p is the viscosity at a pressure P. This idea was already used to calculate the phonon mean free-paths[2] in methyl and ethyl alcohols at high pressures. For zero applied pressure, Eq. (6) becomes

$$\eta_0 = A \exp(\alpha_0 E_H/RT) \quad ...(7)$$

where η_0 and α_0 are the values of viscosity and the parameter α at zero applied pressure. From Eqs. (6) and (7), it follows that

$$\alpha_p = \alpha_0 + RT/E_H \log_e \eta_p/\eta_0 \quad ...(8)$$

From the value of α_p obtained from Eq. (8), it is possible to obtain the value of C in Eq. (4), which indicates the variation of the parameter α with pressure.

Methyl alcohol—The term ($\log_e \eta_p/\eta_0$) from the data of Bridgman[4] for P = 1000 kg/cm^2 is 0·167 at 30°C. The hydrogen-bond energy for methyl alcohol[6] is about 2·33 kcal/mole. Using these values in Eqs. (4) and (8), the value of C for methyl alcohol is calculated to be 11·11. With this value of C in Eq. (5), α_p is calculated at several other values of external pressure at 30°C and these values are shown in Table 1 along with the values obtained from the experimental data of Bridgman[4] on the viscosity of methyl alcohol at high pressures. Table 1 shows an excellent agreement between the values of α_p calculated using Ising model and those from the experimental data on viscosity, upto a pressure of 8000 kg/cm^2. The disagreement at a pressure of 12000 kg/cm^2 may be due to the fact that compression of hydrogen bonds in methyl alcohol becomes important at very high pressures. The compression of hydrogen bonds results in an increase of hydrogen-bond energy E_H and the present model is only valid for a state in which E_H is not significantly altered.

Ethyl alcohol—For an applied pressure of 1000 kg/cm^2, the value of $\log_e \eta_p/\eta_0$ at 30°C for ethyl alcohol[4] is 0·2. Using these values in Eqs. (4) and (8), the values of C and E_H are calculated to be 15·80 and 2·83 kcal/mol for C_2H_5OH. With these values of C and E_H, the values of α_p are calculated for several pressures from Eq. (4) at 30°C and are shown in Table 1 along with the values calculated using the experimental data of Bridgman[4] on the viscosity at pressures above 1000 kg/cm^2. Table 1 shows that both theoretical and experimental values agree reasonably for 4000 kg/cm^2 pressure. The disagreement at 8000 kg/cm^2 may be due to the fact that the compression of hydrogen bonds becomes important as in the case of CH_3OH. It is interesting to note that the agreement between theoretical and experimental values is reasonable upto a pressure of 8000 kg/cm^2 for CH_3COOH whereas it is reasonable up to a pressure of 4000 kg/cm^2 for C_2H_5OH. This indicates that the compression of hydrogen bonds becomes significant at a much lower pressure for ethyl alcohol as compared to methyl alcohol. This can be understood by noting that 94% of the hydrogen bonds are already intact at a pressure of 4000 kg/cm^2 for C_2H_5OH and hence the further association may become increasingly difficult due to repulsive forces, resulting in the compression of hydrogen bonds. For CH_3OH, the fraction of intact hydrogen bonds becomes about 95% at a pressure of 8000 kg/cm^2. From this data, it appears that the association effect due to the application of external pressure predominates till α_p is approximately 0·95. Further increase of pressure on the hydrogen-bonded alcohols results in the compression of hydrogen bonds.

Table 1—Calculated Values of α_p from the Present Theory and the Values Obtained Using the Experimental Data on Viscosity for Methyl, Ethyl and *n*-Propyl Alcohols at 30°C

Pressure kg/cm^2	Fraction of intact hydrogen bonds (α_p)					
	methyl alcohol		ethyl alcohol		*n*-propyl alcohol	
	theo.	exptl.	theo.	exptl.	theo	exptl.
1000	—	—	—	—	0·930	0·945
4000	0·885	0·869	0·946	0·957	0·978	1·039
8000	0·949	0·942	0·983	1·043	—	—
12000	0·979	1·006	—	—	—	—

The molar volume V_0 of the liquid is built into the constant C and hence one would expect that C should be proportional to the molecular weight M of the alcohol. The value of C/M for methyl and ethyl alcohols comes out to be 0·347 and 0·344 respectively indicating C is proportional to molecular weight M of the alcohol. Using this fact, C is estimated as 20·73 for *n*-propyl alcohol and the values of α_p are calculated at several pressures.

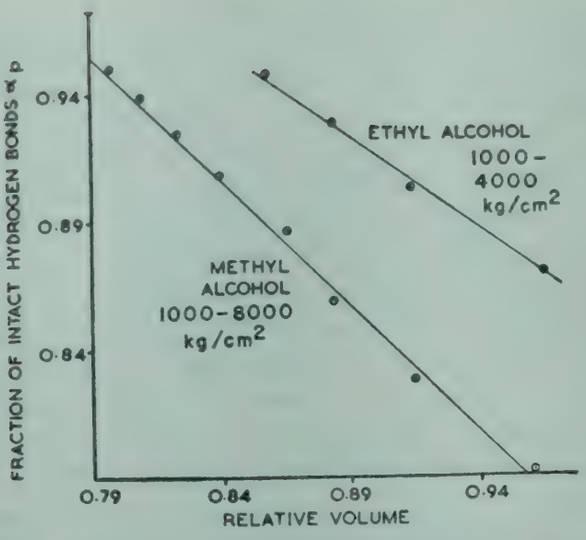

Fig. 1—Variation of α_p [calculated from Eq. (4)] with relative volumes of methyl and ethyl alcohols [from Bridgman[4]] at 30°C

These values are shown in Table 1 along with the values obtained from the experimental data of viscosity[4] at high pressures. Table 1 shows that the agreement between these values is good only upto an applied pressure 1000 kg/cm². This can be understood by noting that 94% of hydrogen bonds are already intact in *n*-propyl alcohol at a pressure of 1000 kg/cm². This clearly illustrates that the compression of hydrogen bonds becomes important in these alcohols after the fraction of intact hydrogen bonds attains the value of 0·95.

The relative volumes of methyl and ethyl alcohols at several pressures may be calculated using Eq. (2) which can be modified as

$$V = V_0 \left[1 - \left(\frac{n - n_0}{N} \right) C'N \right] \qquad \ldots (9)$$

where N is the total number of hydrogen bonds. Eq. (9) can be rewritten as

$$V = V_0 - (\alpha_p - \alpha_0) B \qquad \ldots (10)$$

where B is a new constant.

The correctness of the assumptions made in the derivation of Eq. (10) can be verified by plotting the relative volumes of methyl and ethyl alcohols against α_p at several pressures (Fig. 1). Fig. 1 shows that the variation of relative volume with α_p is a straight line suggesting Eq (10) is reasonably correct. Eq. (10) can be used independently to calculate the relative values of α_p with a knowledge of the volumes at several pressures. To obtain the absolute values, at least one value of α_p at an elevated pressure must be known.

In conclusion, it should be mentioned that the present model based on the broken hydrogen bonds in these alcohols appears to work fairly well at high pressures till the parameter α_p attains the value of 0·95. Further increase of external pressure results in the compression of the hydrogen bonds rather than increasing the association parameter α_p.

The author wishes to express his thanks to the Director, Jawaharlal Institute, Pondicherry-6, for providing facilities to carry out this work.

References

1. Srinivasa Rao A, Srinivasa Manja K & Krishnan B, *Indian J. Chem.*, 13 (1975), 410.
2. Srinivasa Rao A, *Indian J. pure appl. Phys.*, 15 (1977), 78.
3. Reynolds J & Sternstein S S, *J. chem. Phys.*, 41 (1964), 47.
4. Bridgman P W, *The physics of high pressure*, (G Bell, London), 1952.
5. Srinivasa Rao A, *Indian J. pure appl. Phys.*, 14 (1976), 322.
6. Srinivasa Manja K, Krishnan B, Nambinarayanan T K & Srinivasa Rao A, *Bull. Soc. Chim. Belg.*, 83 (1974), 197.

Molecular Constants of Acetylenes : Part II—Centrifugal Distortion Constants & Thermodynamic Functions of Silylacetylene

K Sabapathy, R Ramasamy & K Venkateswarlu

Department of Physics, P S G College of Arts & Science (Autonomous) Coimbatore 641 014

Received 28 *February* 1979

The centrifugal distortion constants of silylacetylene have been calculated for the first time using the potential energy constants and following the methods suggested by D Kivelson and E B Wilson [*J. chem. Phys.*, **20** (1952), 1575; **21** (1953), 1220] and Cyvin *et al.* [*Z. Naturf.*, **23a** (1968), 1649]. The thermodynamic functions of the molecule have also been evaluated.

A microwave study of silylacetylene[1] has shown that this molecule is a symmetric top with point group C_{3v} consisting of $5a_1 + 5e$ species. All the 10 fundamentals are infrared active. Duncan[2] has determined the hybrid orbital force field for silylacetylene following the vibrational assignments of Reeves *et al.*[3] Later, Venkateswarlu and Rudra warrier[4] have calculated the force constants following the assignments of Ebsworth *et al.*[5] In the present investigation, the centrifugal distortion constants and the thermodynamic functions of this molecule have been evaluated for the first time using the available spectroscopic data.[4] The centrifugal distortion constants may be useful to the investigators of the microwave spectra of this molecule. The thermodynamic functions have been evaluated for the ideal gaseous state at one atmospheric pressure

assuming harmonic oscillator and rigid rotor model of the molecule.

The non-vanishing elements of the t matrix and the centrifugal distortion constants[6,7] are presented in Table 1. The molecule being a symmetric top rotor, the elements τ_{xxxx}, τ_{xxyy} and τ_{yyyy} are equal. Also, $\tau_{yyzz}=\tau_{xxzz}$ and $\tau_{yzyz}=\tau_{zxzx}$. The choice of coordinates for this analysis is such that, in the rotation about the Z axis, only the lighter atoms, viz. the hydrogen atoms are involved. Hence, the moments of inertia being very small, the τ elements corresponding to the Z rotation are comparatively large when compared to the values of the elements corresponding to the rotations about X and Y axes where the rotation of the heavier atoms, viz. the silicon and carbon atoms are involved. As no experimental data are available, it has not been possible to compare the calculated values with the observed ones. The centrifugal stretching coefficients are also given in Table 1. These are the linear combinations of the τ elements. Since the molecule is a symmetric top rotor, D_J is positive and the coefficients R_5, R_6 and δ_J vanish. The thermodynamic functions are given in Table 2.

Table 1—Values of Non-vanishing Elements of t Matrix $t_{\alpha\beta\gamma\delta}$ (in amu^2 Å^3/mdyne) Centrifugal Distortion Constants (τ'_s) Centrifugal Stretching Coefficients (in kHz) of Silylacetylene (SiH_3CCH)

$t_{\alpha\beta\gamma\delta}$	Value	$\tau_{\alpha\beta\gamma\delta}$	Value	Centrifugal stretching coefficients	Value
t_{xxxx}	1361·34	τ_{xxxx}	−1·0708	D_J	0·2688
t_{xxyy}	1361·34	τ_{xxyy}	−1·0708		
t_{yyyy}	1361·34	τ_{yyyy}	−1·0708	D_K	48054·745
t_{xxzz}	712·14	τ_{xxzz}	−432·645	D_{JK}	263·174
t_{yyzz}	712·14	τ_{yyzz}	−432·645		
t_{xxzx}	2·15	τ_{xxzx}	−0·0471	R_5	0
t_{yyzx}	8·28	τ_{yyzx}	−0·181	R_6	0·0005
t_{zzzz}	411·88	τ_{zzzz}	−193272·75	δ_J	0
t_{zzzx}	2·44	τ_{zzzx}	−41·1976		
t_{xyxy}	11·10	τ_{xyxy}	−0·0087		
t_{xyyz}	3·63	τ_{xyyz}	−0·0793		
t_{yzyz}	78·02	τ_{yzyz}	−47·3993		
t_{zxzx}	78·02	τ_{zxzx}	−47·3993		

Table 2—Thermodynamic Functions of SiH_3CCH (in cal deg^{-1} mole^{-1})

Temp. K	Heat content, H	Free-energy, F	Entropy, S	Heat capacity, C_p
100	8·2270	42·8794	51·1064	8·8988
200	9·0275	48·8107	57·8382	10·9085
273·2	9·7711	51·7279	61·4991	12·7410
298·15	10·0464	52·5970	62·6434	13·3277
300	10·0718	52·6668	62·7386	13·3732
400	11·1585	55·7098	66·8683	15·3956
500	12·1712	58·3076	70·4788	17·0010
600	13·0892	60·5973	73·6866	18·3373
700	13·9292	62·6982	76·6274	19 4850
800	14·6862	64·6048	79·2910	20·4828
900	15·3881	66·4322	81·8203	21·3459
1000	16·0076	68·0178	84·0254	22·0894

References

1. Muenter J S & Laurie V V, *J. chem. Phys.*, **39** (1963), 1181.
2. Duncan J L, *Spectrochim. Acta*, **20** (1964), 1807.
3. Reeves R W, Wilde R E & Robinson D W, *J. chem. Phys.*, **40** (1964), 125.
4. Venkateswarlu K & Rudra Warrier M K, *Curr. Sci.*, **38** (1969), 211.
5. Ebsworth E A V, Frankiss S G & Jones W J, *J. Molec. Spectrosc.*, **13** (1964), 9.
6. Kivelson D & Wilson (Jr) E B, *J. chem. Phys.*, **20** (1952) 1575; **21** (1953), 1220.
7. Cyvin S J, Cyvin B N & Hagen G, *Z. Naturf.*, **23a** (1968), 1649.

Dielectric Behaviour of Ferroelectric Ammonium Bisulphate Powders

K Sambasiva Rao & A Bhanumathi

Microwave & Magnetic Resonance Laboratories
Physics Department, Andhra University, Waltair

Received 18 *July* 1977; *revised received* 30 *January* 1978

Dielectric constant is determined for powders of NH_4HSO_4 of different particle sizes (ranging from 105 to 710 μm) over a wide range of temperatures to cover para and ferroelectric phases. A dielectric anomaly was observed for all the particle sizes at −3°C denoting the ferroelectric behaviour of ammonium bisulphate. It is found that the dielectric constant decreases with decreasing particle size. The experimental dielectric constant even for the biggest particle size is lower than the theoretically predicted values for a polycrystalline sample. The results are explained by postulating a defective surface layer of dielectric constant 10 and thickness 40 μm.

A recent survey of the literature[1-10] indicates the numerous experimental studies on ammonium bisulphate (NH_4HSO_4) single crystal, which include the dielectric studies. However, no information is available on the compressed powders of different

ranges of particle sizes, which can yield interesting information concerning the discontinuities in the lattice periodicity and effects of the surface layer.

In this note, we report the dielectric measurements of NH_4HSO_4 powder of varying particle sizes (105μm-710μm) in the temperature range -163 to 50°C, at 1 MHz. The experimental values are compared with those for polycrystalline powders and the values of surface layer thickness and dielectric constant are calculated.

Ammonium bisulphate was prepared as reported by Mellor.[11] The crystals obtained were powdered, separated into different particle sizes (105μm to 710μm) by using screen meshes and were pressed into discs (with the help of a thrice silver-coated brass die and using a hydrostatic pressure of $1{\cdot}6\times10^8$ Nm^{-2}). A density of 86% compared to that of a single crystal is achieved at this pressure for all the samples. Measurements of density and dielectric parameters were made at least 3 days after the preparation of the above sample.

Air-drying silver-conducting-paint was used to form electrodes on the two sides of the sample. No significant change in the dielectric parameters was observed for samples of equal densities. The experimental set-up consists of a Franklin oscillator in combination with a variable GR precession condensers of values 110-1100 pF and 11 to 110 pF. The change in capacitance was measured to an accuracy of $\pm$ 0·002 pF.

The temperature variation of dielectric constant for different particle sizes of NH_4HSO_4 is shown in Fig. 1. The ferroelectric transition for all the particle sizes is observed at -3°C as in the case of a single crystal.[1] An abrupt change of dielectric constant was reported at -119°C for single crystal of NH_4HSO_4. However, this behaviour is not found in the case of the powdered sample. From Fig. 1 it is evident that the dielectric constant decreases with decreasing particle size as observed for barium titanate[12] and ammonium tetra-fluoberyllate.[13] The broad peaks for powders and the increase in broadening with the decrease in particle size have also been noted for Rochelle salt[14] powders and may be caused by the difference in the properties of the surface and the bulk.

The temperature variation of the experimental values of dielectric constant, porosity-corrected values using Bottchers formula[15] and the theoretical values obtained by modified Bruggeman's formula[16] are shown in Fig. 2. For the calculation of the theoretical values, Pepinsky's[1] values of the dielectric constant along the three axes of a single crystal were used. It can be noticed from Fig. 2, that the theoretically predicted values are greater than those obtained either experimentally or the porosity-corrected values. But in the vicinity of a transition temperature, the porosity-corrected values are slightly higher than the theoretically predicted values which may be due to the invalidity of Bottchers equation for materials with high dielectric constant. This behaviour of particle size dependence and lowering of experimental values can be qualitatively explained by postulating the formation of a defective

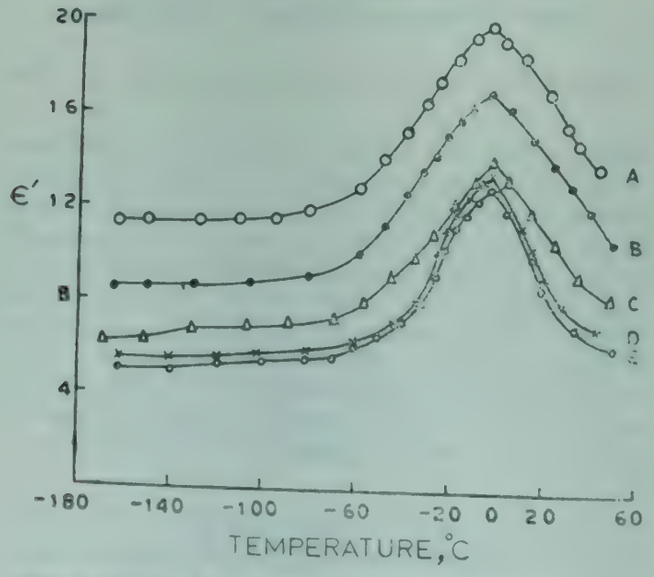

Fig. 1—Dielectric constant as a function of temperature for 5 compressed powders of NH_4HSO_4 [particle sizes A. 500-710 μm; B. 350-500 μm; C. 210-350 μm; D. 177-210 μm; E. 105-177 μm]

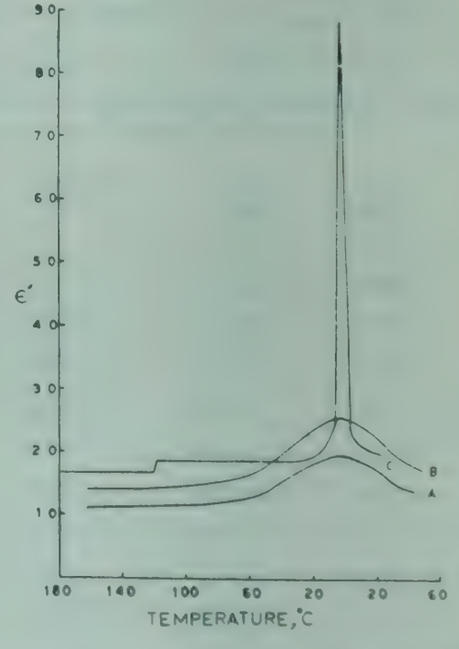

Fig. 2—Dielectric constant as a function of temperature for a polycrystalline sample [A. Exptl. curve (particle size 500-710 μm, δ=0·8346); B. Corrected exptl. curve for porosity using Bottche's formula; C. Theoretically predicted curve]

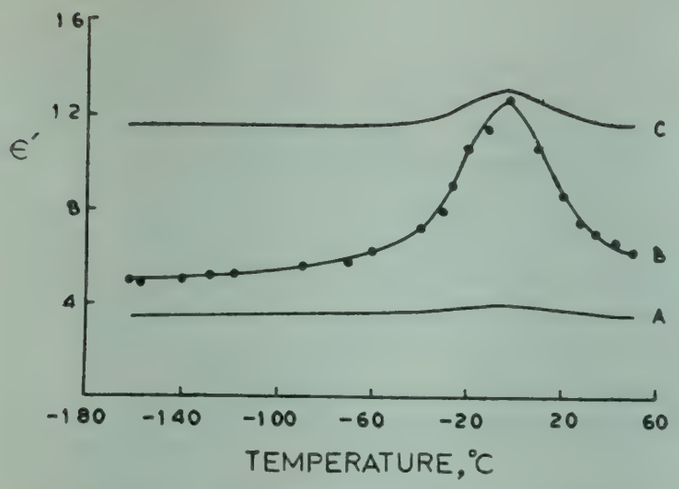

Fig. 3—Expected bounds for the dielectric constant of 3 phase hetrogeneous mixture [B. Exptl curve (particle size 105-177 μm, δ=0·8121); A and C are curves for lower and upper bounds respectively]

surface layer which is due to the mechanical discontinuity in the periodic lattice.[12] Such a surface layer is known to exhibit a low value of dielectric constant as compared to that for the bulk.[17] The surface layer dielectric constant and its thickness have been calculated from the porosity-corrected value and the dielectric constant of the non-defective polycrystalline sample. Assuming the particle to be of spherical shape, Bottchers equation for the surface layer can be expressed as :

$$\delta = \left\{ \frac{a-2d}{a} \right\}^3 ;$$

$$\epsilon_L = \frac{\epsilon_s \{\epsilon^* (3\delta - 1) - 2\epsilon_s\}}{\{3\epsilon_s (3\delta - 2) - \epsilon^*\}}$$

where, ϵ_s is the dielectric constant for the solid of normal density, ϵ_L the dielectric constant of the surface layer, ϵ^* the theoretically predicted value, a the size of the crystallite and d the surface layer thickness.

The periodicity of the lattice attains more and more a regular form as one goes inside the bulk of the sample. The irregularity in the periodic lattice in a defective surface layer increases with decreasing particle size in powders as the ratio of surface area to volume increases. So to estimate the surface layer parameters two samples of narrow particle size range, 177-210μm and 105-177μm, have been chosen. The experimental values of dielectric constant for these ranges are corrected for porosity and the corrected values are taken as the values of dielectric constant for the non-porous sample. The thickness of the surface layer was varied in steps of 0·1μm. From the values of ϵ^* and ϵ_s, the surface layer thickness and its dielectric constant have been calculated using the above equations. In the sample of ammonium bisulphate (NH_4HSO_4) studied, the surface layer thickness which gives the value of the surface layer dielectric constant as 10, was found to be 40μm.

To confirm the surface layer parameter obtained by the above procedure, calculations were carried out by estimating the lower and upper bounds of the three-phase heterogeneous mixture.[18] The calculated bounds are shown in Fig. 3 for a sample of particle size range 105-177μm, along with experimental curve. It is found from Fig. 3 that the experimental values fall within the calculated bounds. Hence it can be assumed that the values of surface layer thickness (40μm) and dielectric constant (10) are of the right order of magnitude. However, the evaluation of the surface layer parameters was made by making certain simplifying assumptions as mentioned above. Hence the parameters obtained are of qualitative nature. It is difficult to determine the percentage error of surface layer parameters as done by other workers.[19]

One of the authors (KSR) is grateful to the University Grants Commission, New Delhi, for financial assistance.

References

1. Pepinsky R, Vedam K, Okaya Y & Hoshino S, *Phys. Rev.*, 111 (1958), 1508.
2. Aizu K, *J. phys. Soc. Japan*, 36 (1974), 937.
3. Bhazhuin P A, Myaznikona T P & Rokov A V, *Fiz. Tverdogo Tela*, 5 (1963), 1780.
4. Strukov B A, Minaeva K A & Rodicheva E N, *Fiz. Tverdogo Tela*, 6 (1964), 76.
5. Myasnikova T P & Yatsenko A F, *Fiz. Tverdogo Tela*, 4 (1962), 653.
6. Strukov B A, Koptsik V A & Ligasova V B, *Fiz. Tverdogo Tela*, 4 (1962), 1334.
7. Nelmes R J, *Ferroelectrics*, 4 (1972), 133.
8. Nelmes R J, *Acta Crystallogr., B*, 27 (1971), 272.
9. Oganga K, Yamada Y, Taguchi I, Osak K, Watanask T, *Nitta, I, Sci. Rep. Osaka Univ.*, 19 (1970), 1.
10. Barbar I, *Phys. Status Solidi*, 45 (1971), 129.
11. Mellor J W, *A comprehensive treatise on inorganic and theoretical chemistry*, Vol. III, pp. 703.
12. Goswami A K, *J. appl. Phys.*, 40 (1969), 619.
13. Sambasiva Rao K & Bhanumathi A, *J. phys. Soc. Japan*, (1980), In Press.
14. Mansingh A & Bawa S S, *Phys. Status Solidi (a)*, 21 (1974), 725.
15. Bottcher C J F, *Theory of electric polarization* (Elsevier Amsterdam), 1952, 417.
16. Mansingh A & Bawa S S, *J. phys. Soc. Japan*, 35 (1973), 1136.
17. Mansingh A & Bawa S S, *J. Phys.*, 7C (1974), 2097.
18. Hashin Z & Shtrikman S, *J. appl. Phys.*, 33 (1962), 3125.
19. Mansingh A & Bawa S S, *Indian J. pure appl. Phys.*, 12 (1974), 483.

Light Absorption & Photoemission of Ag-O-Cs Photocathode

R L VERMA

Optoelectronics Section, E & I Group, Bhabha Atomic Research Centre, Trombay, Bombay 400 085

Received 20 *December* 1978; *revised received* 26 *March* 1979

Light absorption of Ag-O-Cs photocathode has been determined by measuring transmission and reflection over the wavelength range 360-1200 nm. The absorption is minimum at 360 nm, but rises steeply with increasing wavelength and saturates at about 600 nm. It does not show any correlation with the spectral photoresponse of the photocathode. Such a correlation is usually observed in the case of most of the other practical photocathodes. The experimental results are explained on the basis of the energy model proposed by Makhov and Malamid [*Izv. Akad. Nauk., SSSR*, 35 (1971), 370] which envisages donors in Cs_2O as the centres of photoemission.

Complete understanding of the mechanism of photoemission from the Ag-O-Cs photocathode has not been achieved so far, though it was the first to be developed.[1] There seems to be a lack of experimental data on the optical properties of the photocathode. Asao[2] studied the variation in the optical properties of the cathode resulting from evaporation of additional silver with a view to elucidating the role of additional silver in enhancing the sensitivity of the cathode. Later, Sommer[3] measured the transmission only of the photocathode. This note presents the data of our measurements of optical and photoemissive properties of the photocathode in the visible and near infrared regions of the spectrum and explains the results on the basis of an energy model proposed for explaining the photoemission from the Ag-O-Cs photocathode.

The photocathode was formed on one of the end windows of an experimental photo-tube. The construction of the tube as well as the procedure for preparation of the photocathode are described elsewhere.[4] Though the integral sensitivity varied from cathode to cathode, a typical value was found to be about 30 μ A/lm. The typical spectral response curve of the experimental photocathode is shown in Fig. 1. The response curve follows the general pattern characterizing Ag-O-Cs photocathodes.[5]

To determine light absorption in the photocathode layer as a function of the wavelength of the incident light, its optical transmission and reflection were measured over the wavelength range 360-1200 nm. The variations of the light transmission and reflection of the experimental photocathode

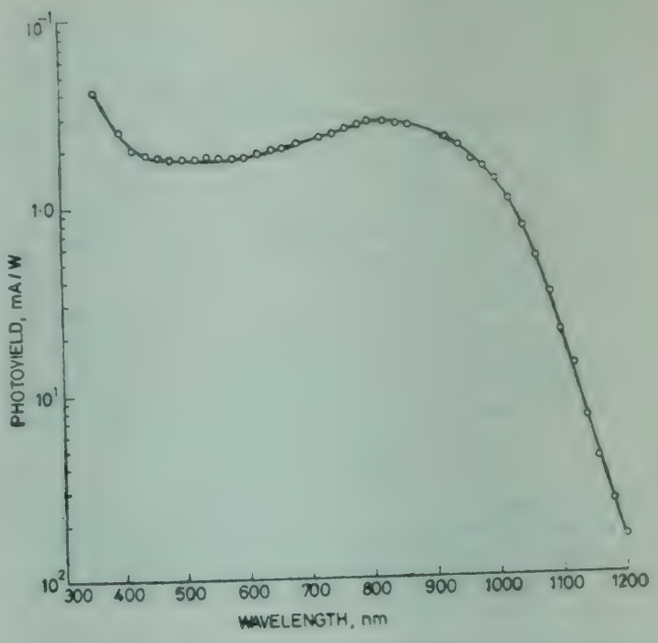

Fig. 1—Spectral response of Ag-O-Cs Photocathode

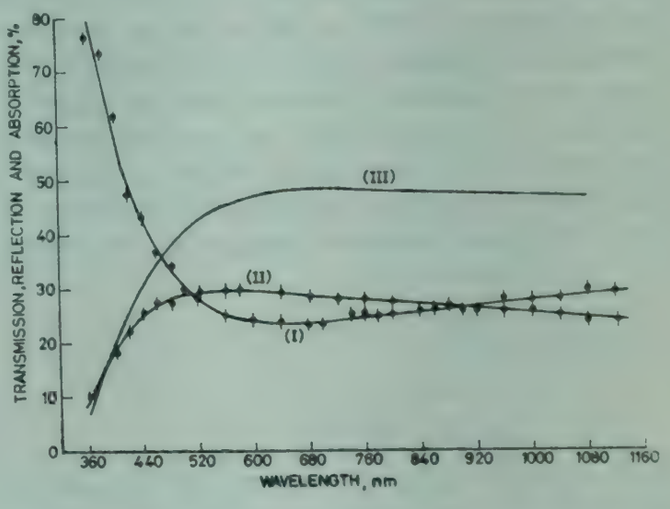

Fig. 2—Variation with wavelength of light transmission (I), reflection (II) and absorption (III) of Ag-O-Cs photocathode

with wavelength of incident light are shown by curves I and II respectively in Fig. 2. The variation in optical absorption as calculated from the formula

$$\text{Absorption (\%)} = 100 - (\text{Transmission \%} + \text{Reflection \%}) \quad \ldots (1)$$

is depicted by curve III in Fig. 2. It is seen from Fig. 2 that the absorption is only 7·5% at 360 nm and rises steeply with increasing wavelength and saturates to a value of about 47% at about 600 nm. In the near infrared region the absorption tends to decrease slightly as the wavelength increases further.

For most of the practical photocathodes, the spectral absorption curve and the spectral photoresponse curve show identical features. Starting at

long wavelength threshold both the curves rise steeply with decreasing wavelength and saturate above a certain photon energy. But this is not so for Ag-O-Cs photocathode as is evident from Figs. 1 and 2. It is seen that in the threshold region, whereas the photoyield decreases rapidly with increasing wavelength, the optical absorption remains practically constant. These peculiar characteristics of this photocathode may be explained as follows:

Ag-O-Cs photocathode is produced by the reduction of Ag_2O with Cs, according to the chemical equation[6,7]

$$Ag_2O + Cs = Cs_2O + Ag \qquad ...(2)$$

Eq. (2) shows that the main constituents of the photocathode are cesium oxide and elementary silver. Cs_2O is a semiconductor with an energy band gap of 2eV (Ref. 8), and hence does not contribute to absorption of light at wavelengths beyond 600 nm. Moreover since the threshold energy for photoemission from Cs_2O is 3 eV (Ref. 8), the compound does not intrinsically contribute to photoemission in the visible or infrared region of the spectrum.

Let us now consider the role of silver. Although the reflection coefficient of bulk silver exceeds 90%, yet thin silver films having island-like structure show relatively lower reflectivity and higher optical absorption.[9,10] Asao[2] measured the optical characteristics of thin silver films having thicknesses comparable to those of Ag-O-Cs photocathodes, and found that light absorption of a typical film is minimum at a wavelength of 320 nm and increases with increasing wavelength and saturates at wavelengths around 600 nm. The good agreement between his results for silver films and the results depicted by curve III in Fig. 2 for the photocathode film suggests that most of the light absorption in the cathode is caused by elementary silver present in the photocathode. But the light absorbed by the silver aggregates does not lead to photoemission since the work function of Ag ($\phi \simeq 4{\cdot}5$ eV)[11] is much larger than the quantum energy of the absorbed photons.

To explain the photoemission mechanism of Ag-O-Cs photocathode, Pakhomov and Malamid[12] proposed a model according to which a part of silver produced by reduction of Ag_2O is dispersed in atomic state in Cs_2O matrix to give rise to donor levels besides Cs donor levels in the forbidden energy zone of Cs_2O. These donors are the main source of photoemission in the visible and near infrared region of the spectrum.[12] Obviously, the numerical density of the donor levels is much smaller than that of the host Cs_2O molecules or of silver atoms present in the silver aggregates. This incidentally accounts for the lower quantum efficiency (0·1%) of Ag-O-Cs photocathodes compared with value of 10% of other practical photocathodes. Thus, even though a direct correlation between the light absorption and the photoemission of the donor centres may be expected, such a relationship is not observed for the whole photocathode because of the much greater optical absorption by the non-emitting silver aggregates which remains practically constant over the spectral region considered.

It is a pleasure to thank Shri C Ambasankaran, Director, E & I Group, for his interest in the work. Helpful discussions with Shri G K Bhide are gratefully acknowledged. Thanks are also due to Shri U S Singh for his technical assistance.

References

1. Koller L R, *Gen. Elect. Rev.*, 31 (1928), 476.
2. Asao S, *Proc. phys-math. Soc. Japan*, 22 (1940), 448.
3. Sommer A H, *RCA Rev.*, 28 (1967), 543.
4. Verma R L & Varma B P, *Indian J. pure appl. Phys.*, 11 (1973), 681.
5. *Spectral response wall chart*, RCA No. PIT-701B, Harrison, N J, 1972.
6. Prescott C H & Kelly M J, *Bell Syst. tech. J.*, 11 (1932), 334.
7. Campbell N R, *Phil. Mag.*, 12 (1931), 173.
8. Borzyak P G, Bibik V F & Kramerenko G S, *Bull. Acad. Sci. USSR, Phys. Ser.*, 20 (1956), 939.
9. Ghosh C & Varma B P, *J. Phys. D.*, 7 (1974), 1773.
10. Sennet R S & Scott G D, *J. opt. Soc. Am.*, 40 (1950), 203.
11. Blackmev L L & Farnsworth H E, *Phys. Rev.*, 77 (1950), 826.
12. Pakhmov M T & Malamid A E, *Izv. Akad. Nauk., SSSR*, 35 (1971), 307.

Dielectric Transient Response of Some Biomolecules Following Ultraviolet Radiation

S B Supekar*

Department of Electronics, G S Institute of Technology & Science, Indore 452 003

&

T K Bandopadhyaya

Department of Electronics, Maulana Azad College of Technology, Bhopal 462 007

Received 2 *April* 1978; *accepted on* 20 *April* 1979

Measurements at different temperatures have been recorded for the decay of dielectric polarization following UV radiation in acetylcholine, cholesterol, cholic acid, haemoglobin and testosterone taken in the powder form. All the samples exhibit the usual exponential decay behaviour. The decay seems to be connected with the traps in the forbidden region.

* Present address : Department of Physics, H P T Arts & B Y K Science College, Nasik 422 005

The objective of the present note is to report on the attempts to study the decay of dielectric polarization of some biomolecules, namely acetylcholine, cholesterol, cholic acid, haemoglobin and testosterone at different temperatures ranging from 300 to 363 K subsequent to ultraviolet irradiation. Experiments were carried out using powders of analytical grade chemicals obtained from Sigma Chemical Co., USA.

The experimental arrangement consists of two parallel plates, one of them made up of copper printed circuit board with a central area of 1 cm × 1 cm and the other of quartz whose inner side is turned conducting by spraying transparent materials through which the sample has been excited by UV radiation. The two plates are separated by suitable insulating spacers. Surfaces of the packed powder sample are made perfectly smooth by putting a conducting paint on the surface of the sample in contact with the electrodes. This avoids the possibility of interfacial polarization. Capacitance and loss factor of this imperfect condenser have been measured by EIO-2 type Schering bridge. The accuracy in the determination of ϵ' and ϵ'' is $\pm$ 5% and $\pm$ 2% respectively. The temperature of specimen in the cell has been controlled by keeping the dielectric cell in a bath whose temperature is controlled with the help of tungeston coil and auto-transformer. The bridge oscillator was set up to a particular frequency of 8·0 MHz and the sample was illuminated by UV radiation of wavelength 365 nm using a 300 W mercury lamp and the interference filter. The whole powdered mass has been irradiated uniformly by spreading in a monolayer. Equilibrium excitation is obtained within 30 min and the impedance variables no longer vary with time under constant illumination. The light is then switched off and the variation of capacitance and tan δ values during the decay has been recorded at intervals of one minute. The measurements were repeated at different temperatures. The actual values of ϵ' and ϵ'' for different samples are determined by the formulae[1]:

$$\epsilon' = \frac{1}{C_0}\left[\frac{C_1}{1 + (\tan\delta)^2}\right]$$

and

$$\epsilon'' = \frac{1}{C_0}\left[\frac{C_1}{1 + (\tan\delta)^2}\right]\tan\delta$$

where C_1 and C_0 are the capacitances of the cell with and without sample and tan δ is the loss tangent. Proper precautions were taken to avoid the possibilities of daylight absorption and moisture adsorption as a slight trace of water content is likely to permit an abrupt change in the dielectric properties.

Polarization values measured with unexposed samples (dark polarization) were subtracted from photo-polarization values and the log ϵ'' values were plotted against time. All the samples showed linear variation with temperature indicating that the dielectric polarization decays exponentially immediately after cutting-off of the ultraviolet excitation. As an example, the decay of polarization for acetylcholine following ultraviolet irradiation is shown in Fig. 1.

The characteristic decay rates for the different samples were obtained at different temperatures from the slopes of these straight lines (Table 1).

It is observed that the time-constants are inversely related to the temperature for all the samples. This means that the absorption decreases with the increase in temperature. These results are in accordance with those of Kallamann *et al.*[2]

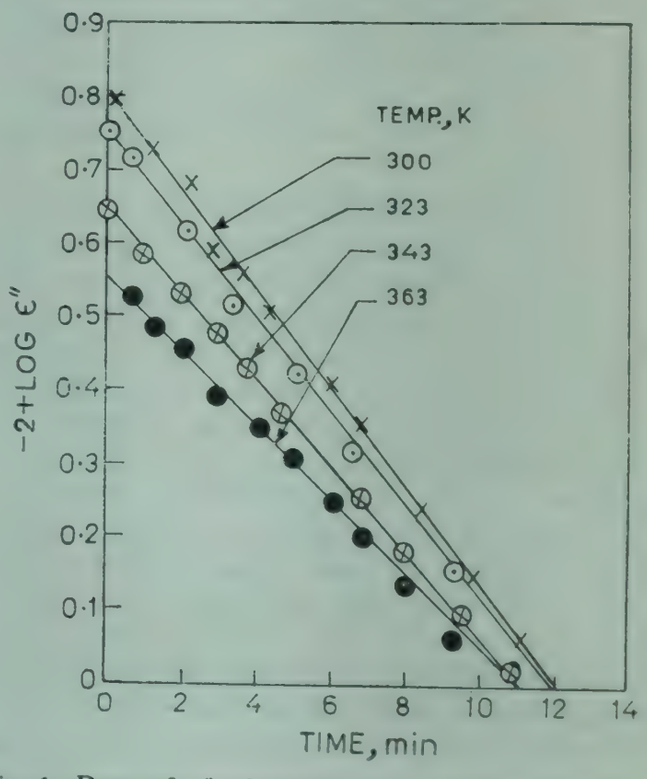

Fig. 1—Decay of ϵ'' of acetylcholine following ultraviolet radiation with time [Frequency of radio wave used for capacitance measurement = 8·0 MHz]

Table 1—Decay Rates (in sec) at Different Temperatures for Different Samples at 8·0 MHz

Temp. K	Acetylcholine	Cholesterol	Cholic acid	Haemoglobin	Testosterone
300	9·66	6·90	9·66	8.28	9·66
323	8·28	5·52	6·90	6·90	8·28
343	6·90	4·83	4·34	5·52	6·90
363	6·10	4·34	4·34	4·83	6·90

who have reported a sharp decrease in the capacitance value following cessation of ultraviolet excitation corresponding to a fast decay of conductivity. Mark *et al.*[3] observed that the conductivity decay in activated Zn-cu-cds in the time range of 4-16 min obeys approximately the exponential relation. The decrease of capacitance after excitation is much slower. They assumed that the capacitance change can be ascribed to trapped electrons and contribute to the changes in capacitance only when they are raised out of their bound level into the conduction band. ESR signal for these samples has been recorded in the *X*-band at 300 K under UV excitation[4] and it has been observed that height of the absorption signal decreases with time, following UV radiation. It seems that some of the molecules come down to the ground state directly whereas some of the molecules may come down to the some intermediate state which may be metastable.

The above behaviour of these biomolecules could be explained along the lines of a model similar to the one proposed by Tatake *et al.*[5] for explanation of the thermo-luminescence in biomolecules. In this model, the electron traps are considered to be normally forbidden metastable states of biomolecules themselves. The electrons excited during irradiation get trapped in these metastable trap (non-radiative) states. Subsequent to irradiation, the population density of the trap states decreases exponentially if the temperature is appropriate and not too low to prevent the detrapping altogether. This would be the situation if the activation energy for the trap state is higher than that denoted by the *KT* factor. The decrease in the time-constant of the dielectric decay with increase in the temperature is thus a natural consequence of the increase of the *KT* factor at higher temperatures. The decay of dielectric loss and luminescence in single calcite crystal following X-ray irradiation has been attributed by Rao and Roy[6] to the depletion of the shallow traps in the forbidden energy region. We believe that this depletion at a given temperature is also due to the supply of the activation energy through the *KT* factor. The present authors[4] have also tried to study the decay of dielectric loss and polarization in these samples following exposure to X-ray and γ-rays. However, no such results were observed. It is found that these ionizing radiations bring about permanent changes in biomolecules through ionization and bond deformations and it is, therefore, not at all surprising that these radiations gave negative results.

The authors thank Prof. D G Dhavalikar, Director and Prof. N Sarkar, Head of Electronics and Telecommunication Engineering Department, G S Institute of Technology and Science, Indore, for extending the necessary facilities to carry out the experimental work. Thanks are also due to Dr V G Tatake, Biology and Agriculture Division, Bhabha Atomic Research Centre, Bombay, for stimulating discussions.

References

1. Montagner Le, Thesis, *Etude experimentale des variation dela constante di ēlectrique liee a unchangement phase*, University of Paris, Paris, 1957.
2. Kallamann H, Kramer B & Perlmutter A, *Phys. Rev.*, 89 (1953), 700-707.
3. Mark P & Kallamann H, *J. Phys. Chem. Solids*, 23 (1962), 1067-1078.
4. Supekar S B, Ph D Thesis, *Dielectric investigation of bioelectric materials*, University of Indore, Indore, 1978.
5. Tatake V G, Desai T S & Sane P V, *Photochem & Photobiol.*, 24 (1976), 463-472.
6. Rao K V & Sujata Roy, *Solid St. Commun.*, 20 (1976), 941-42.

Circuit Parameters for a Complex Helical SWS Combining Results for Simpler Configurations

A K Sinha & B N Basu
Department of Physics, Regional Institute of Technology
Jamshedpur 831 014

Received 11 *January* 1979

Several combinations of equivalent circuit parameters for simpler helical configurations have been tried out to find the dielectric loading factor of a relatively complex practical slow-wave structure (SWS) consisting of a helix supported by wedge bars in a metal shell. The combinations yield results which compare well with those obtained from an actual field analysis.

Dispersion characteristics of a helical slow-wave structure (SWS) can be obtained from its equivalent circuit parameters.[1,2] Paik[2] predicted these parameters for a very commonly used SWS for travelling wave tubes (TWTs) that consists of a helix supported by longitudinal dielectric wedge bars in a metal shell [Fig. 1; configuration (vi)] by treating the structure as equivalent to a helix surrounded by a continuous dielectric tube in a metal shell [Fig. 1 : configuration (v)], the dielectric being of an effective relative permittivity determined by the support parameters.[8] Paik's approach was to combine the individual results for two simpler configurations (combination I in Table 1) : a helix surrounded by an infinite dielectric [configuration (i)] and a helix in a metal shell without any dielectric surrounding [configuration (iv) to obtain the results for configura

tion (v) (Fig. 1)]. The circuit parameters, inductance per unit length (L) and capacitance per unit length (C), obtained by this procedure are given in Table 1. Results in respect of two more combinations II and III are also included in Table 1. These parameters can be easily derived by inspecting the individual dispersion relations for the configurations shown in Fig. 1.

The dispersion relation for configuration (v) can be obtained from the relation

$$\beta^2 = \omega^2 LC$$

and then comparing the resulting dispersion relation with that for a helix in free space, one can find the dielectric loading factor (D) of the structure.[4] Fig. 2 shows the plot of D versus the normalized shield radius (γb) for configuration (vi), treating the latter as equivalent to configuration (v) and interpreting ϵ_r as an effective relative permittivity ϵ_r' given by[3]

$$\epsilon_r' = 1 + \frac{\phi N}{2\pi}(\epsilon_r - 1)$$

Table 1—Equivalent Circuit Parameters for Configuration (vi) obtained by Combining Results for Simpler Configurations [(i)-(iv) of Fig. 1]

Combination	Configurations combined	Equivalent circuit parameters L	C
I (Ref. 2)	(i) and (iv)	$L_0(1-\chi_L)$	$C_0(1-\chi_C)^{-1}[1+(\epsilon_r-1)\,Gf_I]$
II	(ii) and (iv)	$L_0(1-\chi_L)$	$C_0(1-\chi_C)^{-1}[1+(\epsilon_r-1)\,Gf_{II}]$
III	(i), (iii) and (iv)	$L_0(1-\chi_L)$	$C_0(1-\chi_C)^{-1}[1+(\epsilon_r-1)\,Gf_{III}]$

$L_0 = \frac{\mu_0}{2\pi} I_1(\gamma a) K_1(\gamma a)\left(\frac{\beta}{\gamma}\right)^2 \cot^2\frac{\phi}{2}$, inductance per unit length for a helix in free space

$C_0 = \frac{2\pi\epsilon_0}{I_0(\gamma a) K_0(\gamma a)}$, capacitance per unit length for a helix in free space

$\chi_C = \frac{I_0(\gamma a) K_0(\gamma b)}{K_0(\gamma a) I_0(\gamma b)}$, capacitive coupling coefficient

$\chi_L = \frac{I_1(\gamma a) K_1(\gamma b)}{K_1(\gamma a) I_1(\gamma b)}$, inductive coupling coefficient

$f_I = 1$ (Combination I)

$f_{II} = 1 - \frac{\epsilon_r \xi_{ab}}{\{G\epsilon_r + \xi_{ab} + \xi_{ab}(\epsilon_r - 1)\}}$ (Combination II)

$f_{III} = \frac{\xi_{ab}}{\{G\,1 + \epsilon_r \xi_{bb} - \xi_{ab}(\epsilon_r - 1)\}}$ (Combination III)

$G = \gamma a I_0(\gamma a) K_1(\gamma a)$

$\xi_{js} = \frac{I_0(\gamma j) K_1(\gamma s)}{K_0(\gamma j) I_1(\gamma s)}$

where I_0, K_1, etc. represent the modified Bessel functions; γ is the radial propagation constant; a and b are respectively the radii of the helix and the shield (see Fig. 1).

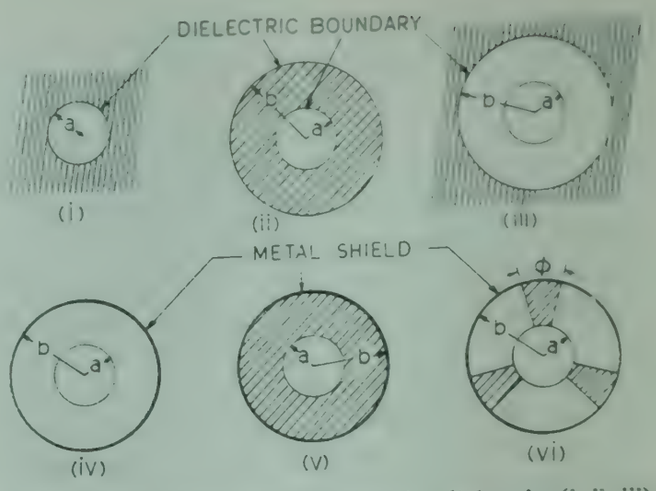

Fig. 1—Various helical configurations in dielectric (i, ii, iii), in metal shield (iv), and in dielectric and metal shield (v, vi)

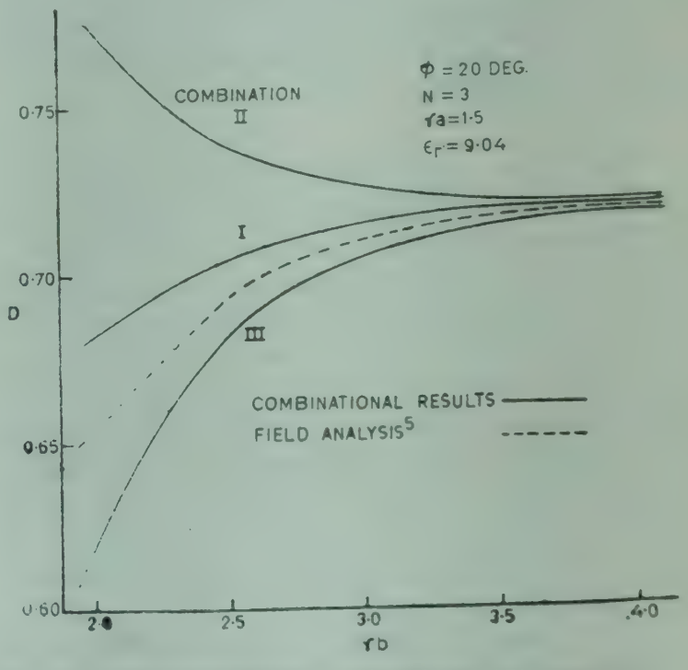

Fig. 2—Variation of dielectric loading factor (D) versus normalized shield radius (γb) for configuration (vi) of Fig. 1

where N is the number of longitudinal dielectric wedge supports arranged symmetrically around the helix, ϕ the angle of wedge, and ϵ_r the relative permittivity of the dielectric. We have taken $N = 3$, $\phi = 20°$, $\epsilon_r = 9{\cdot}04$ (which makes $\epsilon_r' = 2{\cdot}34$) and $\gamma a = 1{\cdot}5$. It is found that combination I, proposed by Paik,[2] gives much more accurate results than are predicted by another immediately striking configuration II; the results are compared with respect to those obtained by an actual field analysis.[5] It is seen from Fig. 2 that combination III also gives fairly accurate results. We, however, note that compared with the value of D obtained by the actual field analysis, the value predicted by combination I lies above, and that by combination III lies below.

For large shield radii, all the combinations lead to the same result. The method presented in this note is useful in designing a complex helical SWS by inspecting known results for relatively simple helical configurations.

References

1. Kino G S & Paik S F, *J. appl. Phys.*, 33 (1962), 3002.
2. Paik S F, *IEEE Trans. Electron Devices*, 16 (1969), 1010.
3. Loshakov L N & Ol'derogge E B, *Radio Engng Electron Phys.*, 13 (1958), 45.
4. Basu B N & Joshi S N, *CEERI Internal Report* No. IR-01-VT/78 (Central Electronics Engineering Research Institute, Pilani), 1978.
5. Basu B N, *Proceedings of symposium on Digest on Electron Devices* (Central Electronics Engineening Research Institute, Pilani, 1978, 3·17.

Laser Raman Spectrum of 3,4-Dichlorobromobenzene

S R Tripathi* & G N R Tripathi**

Department of Physics, University of Gorakhpur
Gorakhpur 273 001

Received 6 *February* 1979

Laser Raman spectrum of 3,4-dichlorobromobenzene has been recorded in the region 3500-100 cm^{-1} in the liquid phase and interpreted on the basis of infrared and ultraviolet spectra of this molecule. Assignments of some low frequency bands are discussed.

The vapour phase ultraviolet and liquid phase infrared spectra of several trisubstituted halogen derivatives of benzene have been studied in our laboratory[1-4] in recent years. The Raman data on only a few of these molecules are available in literature[5,6] and, therefore, our assignments of the infrared spectra in some cases, were based on comparison with the vibrational spectra of several similar molecules and the conclusions drawn from the analysis of the vapour phase ultraviolet spectrum. 3,4-Dichlorobromobenzene (DCBB) is one such molecule which was studied by us in ultraviolet[2] and infrared[1] spectral regions without any published Raman work. The present note reports an analysis of the Raman spectrum of DCBB molecule and its implications on our previous assignment of this molecule.

The compound was supplied by M/s Koch Light, England (98% pure) and used as such. The laser Raman spectrum of this compound was recorded in the region 100-3500 cm^{-1} on a Carry 81 Raman spectrometer. This material is liquid at room temperature; therefore, the sample cell was a glass capillary of $\approx$ 2 mm in diameter. The 488 mm laser line, obtained from coherent radiation model CR-3 argon ion laser source, was used for exciting the Raman emission. The spectrum between 300-3500 cm^{-1} was recorded using slit width of 6 and 8 cm^{-1}, sensitivity 4×10^2 and 10^3 with time constant 5 and 10 sec respectively at a scan speed of 1 cm^{-1}/sec using a double slit. The spectrum in the region 100-250 cm^{-1} was recorded using single slit in the same conditions.

Results and discussion—The molecular structure of DCBB molecule has not been studied so far either by crystallographic or spectroscopic techniques, but a planar structure with C_s symmetry is quite reasonable to consider for the vibrational analysis of the spectrum. The 30 normal modes of the molecule will be distributed in irreducible representation as

$$\tau = 21\ a' + 9a''$$

The a'' symmetry type vibrations in this molecule involve out-of-plane vibrations which are expected to occur below 1000 cm^{-1}. Although no Raman depolarization data are available, it has been possible to distinguish between the two types of vibrations on the basis of the intensity of the Raman bands. The fundamental frequencies above 1000 cm^{-1} in benzene derivatives involve the planar vibration of the phenyl and substituent groups which are symmetric with respect to the molecular plane (a'). Table 1 reports Raman, infrared and ultraviolet fundamental frequencies of DCBB molecule and it is clearly seen that the laser Raman data in this region support the assignments proposed earlier by Tripathi *et al.*[1,2] The assignment of the frequencies below 1000 cm^{-1} is difficult because the phenyl and substituent group characteristic vibrations sometimes exhibit frequencies in the same range, and the vibrations of same symmetry and with small frequency difference strongly intermix to give rise to mixed modes. The lack of data on the lower frequency region in the benzene derivatives and occurrence of several phenyl and substituent group frequencies in this region also add to the complexity of the spectrum. We will limit ourselves in this note to the discussion of low frequency modes.

Group vibrations—The a'' type of vibrations have major contribution from C—C (3), C—H (3), C—Cl (2) and C—Br (1) vibrations. The C—H and C—C out-of-plane deformations are expected to have comparatively higher frequencies than the C—Cl or C—Br out-of-plane vibrations. In the low frequency region, a band around 100 cm^{-1} has been measured

*Permanent address: Department of Physics, National Degree College, Barhalganj, Gorakhpur 273 001

**Present address: Radiation Laboratory, University of Notre Dame, Notre Dame, Indiana, 46556 USA

Table 1—Correlation of Fundamental Frequencies (in cm^{-1}) of 3, 4-, 2, 5- & 2, 4-Dichlorobromobenzenes

Species C_s	3, 4-Dichlorobromobenzene			2, 5-Dichlorobromobenzene				2, 4-Dichlorobromobenzene			Assignment
		Ultraviolet				Ultraviolet			Ultraviolet		
	Infrared	GS	ES	Raman	Infrared	GS	ES	Infrared	GS	ES	
a''	—	111	90	108	—	115	—	—	123	—	γ(C—Br)
a''	—	179	—	176	—	179	—	—	—	—	
a''	—	—	185	206	—	—	—	—	—	206	γ(C—Cl)
a'	—	262	—	266	275	—	—	290	—	—	β(C—Br)
a''	310	312	—	305	—	—	—	—	—	—	γ(C—C)
a'	360	376	342	377	360	—	295	—	370	340	β(C—Cl)
a'	435	—	—	458	435	396	—	440	—	—	ν(C—Br)
a''	540	—	506	533	540	—	—	560	—	494	β(C—C)
a'	675	—	621	678	670	—	610	680	—	616	ν(C—Cl)
a''	690	—	—	698	690	—	—	690	—	—	γ(C—C)
a'	790	—	—	790	795	—	777	815	—	—	ν(C—C)
a'	1035	—	989	1038	1030	—	989	1030	—	930	β(C—C)
a''	1090	—	—	1088	1100	—	—	1045	—	—	β(C—H)
a'	1135	—	1096	1138	1145	—	1087	1140	—	1097	β(C—H)
a'	1250	—	1113	1256	1250	—	1116	1280	—	—	ν(C—C)
a'	1450	—	—	1491	1455	—	—	1470	—	—	ν(C—C)
a'	1568	—	—	1568	—	—	—	1585	—	—	ν(C—C)
a'	1660	—	—	1638	—	—	—	—	—	—	ν(C—C)
a'	3005	—	—	3057	—	—	—	3040	—	—	ν(C—H)
a'	3070	—	—	3076	3075	—	—	—	—	—	ν(C—H)
a'	3090	—	—	3086	3090	—	—	3120	—	—	ν(C—H)

*ν, β and γ Represent the stretching, in-plane and out-of-plane bending vibrations

in isomeric dichlorobromobenzenes. An emission peak at 108 cm^{-1} which is not very prominent in the Raman spectrum of DCBB is measured. We assign it as out-of-plane vibration associated with the substituent group. In dichlorofluorobenzene (DCFB) no band of this magnitude could be detected. One may, therefore, easily conclude this to be an out-of-plane vibration characteristic to C—Br bond in agreement with the assignments made by Shurvell[7] and Green.[5,6] The band measured at 206 cm^{-1} is very strong. Nearly in all the chlorinated benzenes, a depolarized Raman frequency $\sim$ 200 cm^{-1} has been reported and can be assigned to have major contribution from the C—Cl out-of-plane bending mode.

There will be two C—Cl and one C—Br stretching vibrations. Out of the two C—Cl stretching vibrations only one could be identified at 678 cm^{-1}. The corresponding infrared and excited state (ultraviolet) frequencies have been reported at 675 and 621 cm^{-1}. The fundamental involving the stretching of C—Br bond is assigned around 450 cm^{-1} in bromobenzenes.[5-7] A band at 458 cm^{-1} appears prominently in Raman spectrum of DCBB. The 6*a* vibration of benzene is also likely to have a frequency in this neighbourhood, but on comparison with the spectral data of DCFB it has been assigned to arise due to the stretching of C—Br bond. The frequency 266 cm^{-1} appearing strongly has been correlated to C—Br in-plane mode on the same grounds. It has been detected at 262 cm^{-1} in ultraviolet spectrum. The C—Cl in-plane bending mode is reported at 377 cm^{-1} which agrees well with the assignment made by Bellamy.[8]

Ring vibrations—The 6*a* and 6*b* phenyl vibrations being degenerate are considerably influenced by substitution in benzene depending upon the position of the substituents. In *para* 1, 4-di-derivatives, the substituent groups do not effectively participate in the 6*b* vibration; therefore, it is observed around 620 cm^{-1}. However, the 6*a* vibration in which the displacement of the substituent groups occurs, is reduced to 520 (13%). If a further substitution is made at position 3 in a di-substituted benzene, as in DCBB both these vibrations are expected to reduce substantially and may lie in the region 350-550 cm^{-1}.

This is also the region where the C—Cl and C—Br stretching frequencies appear. As such, it is somewhat difficult to make assignments in an unambiguous way. However, on the basis of comparison with the vibrational spectra of similar molecules as proposed by Tripathi *et al.*[1] the Raman frequencies 533 and 357 cm^{-1} can be correlated respectively to 6*a* and 6*b* phenyl modes.

The two symmetrical ring vibrations of benzene, namely a_{1g} (992 cm^{-1}) and b_{1u} (1010 cm^{-1}) are close enough to each other to interact under reduced symmetry in benzene derivatives. On interaction, two composite modes arise lying between 750-1050 cm^{-1} in infrared, Raman and ultraviolet spectra. In halobenzenes, the first component lies around 1000 cm^{-1} and the second component falls towards the lower frequency region at a separation of nearly 200 cm^{-1} (Table 1). A comparison of infrared and ultraviolet spectra of 3, 4- , 2, 4- and 2,5-dichlorobromobenzenes shows that the above two components are at 1038 and 790 cm^{-1} in the Raman spectrum. The excited state value at 989 cm^{-1} can be correlated to Raman frequency 1038 cm^{-1}.

One of the authors (GNRT) wishes to thank Prof. J E Katon, Miami University, Oxford, OH, USA, for making available his Raman spectrometer to record the spectrum of DCBB.

References

1. Tripathi G N R & Pandey V M, *Indian J. pure appl. Phys.*, 15 (1977), 432.
2. Tripathi G N R & Pandey V M, *Spectrosc. Lett.*, 10 (1977), 533.
3. Tripathi G N R, Sita Ram & Pandey V M, *Indian J. pure appl. Phys.*, 11 (1973), 374.
4. Singh S J, *Spectroscopic studies of some substituted benzenes*, Ph D thesis, Gorakhpur University, Gorakhpur, 1975.
5. Green J H S, *Spectrochim. Acta*, 26A (1970), 1503, 1523, 1913.
6. Green J H S, Harrison D J & Kynaston W, *Spectrochim. Acta*, 27A (1971), 793, 807.
7. Shurvell H F, Dulaurens B & Pesteil P, *Spectrochim. Acta*, 22 (1966), 333.
8. Bellamy L J, *The infrared spectra of complex molecules* (Chapman and Hall, London), 1975.

Automatic Trigger Pulse Logic for the Pulse Programmer for Use in Pulsed NMR

R K Shenoy & J Ramakrishna
Department of Physics, Indian Institute of Science
Bangalore 560 012
and
R Srinivasan
Electronics Division, National Aeronautical Laboratory
Bangalore 560 017

Received 23 *March* 1979

Automatic regeneration of any desired sequence is suggested by an extension of the time base of the pulse programmer. The time interval available for repetition of a sequence is variable from 1-10,000 sec, which can be easily extended.

Magnetic relaxation times T_1 or T_2 are measured using standard pulse sequences like, π-τ-$\pi/2$, $\pi/2$-τ-$\pi/2$, π-τ-$\pi/2$-τ_1-π, etc. For example, in a two-pulse sequence (π-τ-$\pi/2$) the π-pulse may be called the initial pulse and the ($\pi/2$)-pulse the sampling pulse. In a relaxation time measurement, the response for the sampling pulse is measured using a signal averaging instrument, like a boxcar integrator. For the purpose of signal averaging the pulse sequence has to be repetitive. The accuracy of relaxation time measurement is dependent, apart from other factors, on the restoration of the thermal equilibrium magnetization, before the next pulse sequence is applied. In other words, the initial pulse should always monitor the thermal equilibrium magnetization. This is ensured by waiting for at least five times T_1 between the repetitive pulse sequences.[1] Therefore, the pulse sequence has to be repeated as follows: (π-τ-$\pi/2$)-5 T_1-(π-τ-$\pi/2$)-5T_1. In our earlier design of the pulse programmer[2] the instrument requires an external trigger for repetitive operation. The repetition rate of the external pulse input decides the time interval between the first pulse of a sequence and the first pulse of the following sequence (i.e. the time between two π-pulses) and not the time between the second pulse of a sequence and the first pulse of the following sequence [i.e. the time between the ($\pi/2$)- and the π-pulses]. This is of little consequence when τ is very small. But τ must go as high as about 3-4 times T_1 and hence for large values of τ the spin system is not allowed to return to equilibrium completely between sequences. This difficulty is overcome in the present design by an extension of the time-base of the pulse programmer

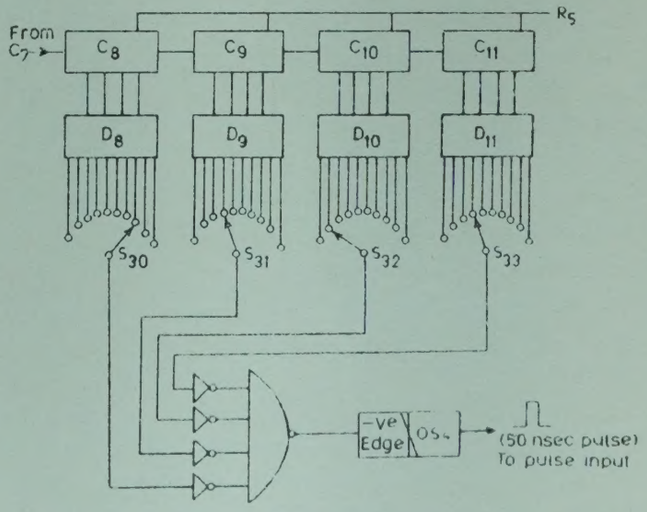

Fig. 1—Schematic diagram illustrating the automatic trigger pulse logic

and inclusion of a simple logic circuit which allows maintaining the time gap $5T_1$ independent of the variation in τ.

Description of the circuit—Counters C_8 and C_9 and decoders D_8 and D_9 of the pulse programmer are reproduced in Fig. 1 for the sake of ready reference. C_{10} and C_{11} along with decoders D_{10} and D_{11} extend the time-base up to 10,000 sec. Four extra thumb wheel switches S_{30}-S_{33} provide 1-10,000 sec variation for the repetition of the sequence which can be easily extended on both higher as well as lower time scales. In the repetitive mode of operation, the clock pulses advance the counters even after the completion of the programmed sequence. On coincidence between the set values in S_{30}-S_{33} and the counter states C_8-C_{11}, the input to the AND gate formed by four inverters and a 4-input NAND gate go 'high' producing 'low' at the negative edge triggered monostable OS4, which gives a 50 nsec pulse. This 50 nsec pulse is used as the trigger pulse at the 'pulse input' of the programmer. Generally, when the instrument is switched on, the counters are advanced and the first sequence is generated automatically by the spurious spike input to the monostable OS4, after which the programmer continues to produce the sequence in a repetitive manner till it is switched off.

The advantages of this circuit are (i) it uses the same time-base, except for one or two extra counters and decoders and the user is at liberty to include any number of extra timing counters; (ii) higher time intervals can easily be obtained by extending the time-base which is otherwise tedious and expensive to get by using a high value capacitor for the usual monostable timing element, when an external pulse input is used.

The project is supported by a grant from the Department of Atomic Energy (DAE), Government of India and one of the authors (RKS) acknowledges with thanks the grant of a fellowship given by DAE.

References

1. Farrar T C & Becker E D, *Pulse and Fourier transform NMR* (Academic Press, New York), 1971.
2. Shenoy R K, Ramakrishna J & Srinivasan R, *J. Phys.:E*, 9 (1976), 779.

INSTRUCTIONS TO CONTRIBUTORS

Manuscripts should be typewritten in double space and on *only one side* of good quality paper; the original and *one carbon copy are to be submitted.*

Papers must be written in clear and concise English. Good attention to spelling and grammar should be given. Long introductions should be avoided. Standard international nomenclature should be followed in giving names of chemical compounds. Standard abbreviations for units of measurement should be used in the text, tables and illustrations. The abbreviations should be used without fullstops.

Title—The title should be neither too brief/general nor unnecessarily long. It should reflect the content of the paper so as to derive the maximum advantage in indexing and information retrieval. A short title for use as running title should also be supplied. If a paper forms part of a series, a subtitle indicating the aspects of the work covered in the paper should be provided.

Abstract—The abstract should indicate the scope of the work and the principal findings of the paper. It should not exceed 3% of the length of the paper and, barring exceptional cases, it should not exceed 200 words. The abstract should be prepared in such a form that abstracting periodicals can use it without modification.

Data—Only such primary data as are essential for understanding the discussion and the main conclusions emerging from the study should be included. All such secondary data as are of interest to a specific category of readership may, if necessary, be deposited in the editorial office (or retained by the authors) for supply on demand. A footnote to this effect may be inserted at a suitable place in the paper.

Mathematical portions—Special attention should be given to the mathematical portions of the paper. Equations must be well separated from the text and written clearly with good separation between the successive lines. The usual norms of breaking long mathematical expressions may be adhered to. Equations should be numbered consecutively in Arabic numerals with the number in parenthesis near the right hand margin. Superscripts and subscripts should be clearly indicated in pencil by V and Λ sign respectively. Capital and small letters, particularly of the same letter when both occur, as well as letters or symbols likely to be confused one for the other, should be clearly distinguished. Special characters (e.g. Greek, script, vector, tensor, matrix, etc.) required must be indicated by marginal notes. Letters and symbols which should appear in bold face must be clearly indicated. To simplify typesetting: (i) long and complicated mathematical expressions which are frequently repeated should be replaced with single letter/symbol, without clashing with the others used in the paper; (ii) the "exp" form of complex exponential functions should be used: and (iii) to simplify fractions, the solidus (/) is to be used and fractional exponents are to be used instead of root signs, e.g.

write $\left(4\omega_{pl} K_{3\lambda}^2 \Big/ \tilde{\omega}\ K_D^2\right)^{1/2}$ and *not* $\sqrt{4\,\omega_{pl} K_{3\lambda}^2 / \tilde{\omega}\, K_D^2}$

write $\exp\{-i\omega_0 (t_1 - t_2)/2\}$ and *not* $e^{-i\omega_0 (t_1 - t_2)/2}$

Tables—Tables should be typed *on separate sheets* of paper without any text matter on the page. They should be numbered consecutively in Arabic numerals and should bear brief titles. *Column headings should be brief.* Units of measurements should be abbreviated and placed below the headings. Nil results should be indicated and distinguished clearly from absence of data. Graphs as well as tables, both representing the same set of data, must be strictly avoided. Inclusion of structural formulae inside the tables should be avoided as far as possible. Tables should be referred to in the text by numbers and not by terms like 'above', 'below', 'preceding' or 'following'.

Illustrations—All illustrations should be numbered consecutively in Arabic numerals. Captions and legends to the figures should be self-explanatory and should be typed on a separate sheet of paper and attached at the end of the manuscript. Line drawings should be made with Indian ink on white drawing paper (perferably Bristol board), cellophane sheet or tracing cloth. In addition to the originals, a set of blue-prints or photostat copies should be sent. For satisfactory reproduction, the graphs and line drawings should be drawn to approximately twice the printed size.

The lettering should be uniform, perferably in stencil, so as to be *not less than 2 mm after reduction* widthwise to 3" or 6" as required. The size of geometrical shapes (used to distinguish different graphs), dot, lines, etc. should be sufficiently large to permit the necessary reduction without loss of detail. In the case of *photographs*, prints *must be on glossy paper and contrasty*. If an illustration is taken from another publication, reference to the source should be given and prior permission secured. Illustrations should be protected by thick cardboard packing against creases, folds and broken corners during transit. Illustrations should be referred to in the text by numbers and not by terms like 'above', 'below', 'preceding' or 'following'.

Infrared, ultraviolet, NMR and other spectra, DTA curves, etc. should be included only if they pertain to new compounds and/or are essential to the discussion; otherwise only significant numerical data should be included in the text.

References—The list of references should be prepared strictly in accordance with the style followed

in the Journal. In the text, references to literatures should be numbered consecutively, in the order of their first occurence, and should be indicated by superscripts at the relevant places; as far as possible the placement of references on numerals of other symbols should be avoided; in such cases the reference may be given in parentheses in running text, e.g. "this yielded for n a value of 2·3 (Ref. 5)". Full bibliographic details for all the references mentioned in the text should be listed in serial order at the end of the paper.

In citing references to research papers, names and initials of authors should be followed, in order, by the title of the periodical in the abbreviated form (underlined), the volume number (two lines underneath), the year within circular brackets and the page reference [e.g. Venkatesh, H G & Guha Sarkar, G, *Indian J. pure appl. Phys.*, **12** (1974), 502]. For names of periodicals, the standard abbreviations listed in the *World list of scientific periodicals* edited by P Brown & G B Stratton (Butterworths & Co. Ltd, London), 4th Edition, 1963-65, should be used. If the reference is to an article published without any authorship in a periodical, the title of the article takes the place of the author in the citation [e.g. The content, influence and value of scientific conference papers and proceedings. *Unesco Bull. Libr.*, **16** (1952), 113-26.]. If a paper has been accepted for publication, the names of the authors and the journals should be given followed by the words "in press" within circular brackets [e.g. Sastry, B. A. & Sastry, G. S., *Physica*, (in press).].

In the list of references, unpublished work, accepted papers in press and personal communications should be clearly distinguished.

Even if a reference contains more than two authors, the names of all the authors with their respective initials should be given. The abbreviations *et al.*, *idem* and *ibid* should be avoided.

Reference to a book should include details in the following order: names and initials of authors, the title of the book (underlined), name of publisher and place of publication within circular brackets and year [e.g. Herzberg, G, *Spectra of diatomic molecules* (D Van Nostand & Co. Inc., New Jersey), 2nd Edn, 1950), 31.]. If the reference is to the work of an author published in a book by a different author or edited by a different person, the fact that it is cited from the source book should be clearly indicated [e.g. Garlick, G F J, cited in *Encyclopedia of Physics*, Vol. 26—*Light and matter* II, edited by S Flugge (Springer Verlag, Berlin), 1958, 1.].

Proceedings of conferences and symposia should be treated in the same manner as books. Reference to a paper presented at a conference, the proceedings of which are not published, should include, in the following order, names and initials of authors, title of the paper (underlined), name of the conference, place where the conference was held and date (Deekshitulu, B L, *Design and fabrication of drum scanner for picture processing*, paper presented in the Symposuim on Applied Optics, Indian Institute of Science, Bangalore, 28-30 Nov. 1974).

Reference to a thesis should include the name of the author, title of the thesis (underlined), university or institution to which it was submitted and year of submission (e.g. Chandrasekaran, K S, *Studies on crystal structure and absolute configuration of crystals*, Ph. D. thesis, Madras University, 1956).

Reference to a patent should include names of patentees, country of origin (underlined) and patent number, the organization to which the patent has been assigned within circular brackets, data of acceptance of the patent and reference to an abstracting periodical where available [Trepagnier, J H, *US Pat.* 2,463,219 (to E I du Pont de Nemours & Co.), 1 March 1949, *Chem. Abstr.*, 43 (1949), 7258.].

Abbreviations and symbols—Abbreviations used should conform to the style of the journals. The following prefixes to units of measurements may be used for expressing submultiples and multiples.

Submultiples	*Abbreviation*	*Multiples*	*Abbreviation*
Deci- ($=10^{-1}$)	deci	deca- ($=10^{1}$)	deca-
centi- ($=10^{-2}$)	c	hecto- (10^{2})	hecto
milli- (10^{-3})	m	kilo- ($=10^{3}$)	k
micro- ($=10^{-6}$)	μ	mega- ($=10^{6}$)	M
nano- ($=10^{-9}$)	n	giga- ($=10^{9}$)	G
pico- ($=10^{-12}$)	p	tera- ($=10^{12}$)	T
femto- ($=10^{-15}$)	f		
atto- ($=10^{-18}$)	at		

Frequently repeating combinations of words, e.g. electric field gradient (EFG), junction field effect transistor (JFET), stimulated Raman emission (SRE), should be abbreviated subsequently, indicating the abbreviated form in parentheses, as shown, at the place of their first occurrence,

Nomenclature—Where too many symbols are used in the text, a section entitled "Nomenclature", explaining the significance of the various symbols, may be given and placed just above the Acknowledgement section.

Acknowledgement—Acknowledgements should not be exuberant and must be made only to real assistance rendered in connection with the work reported in the paper.

Appendixes—Appendixes, typed on separate sheets, should be numbered consecutively, in Arabic numerals, in the order of their occurence in the text, and should be placed at the very end of the paper.

Printed and Published by Shri D S Sastry, Publications & Information Directorate, Council of Scientific & Industrial Research, New Delhi at the Leipzig Press, D-62 South Extension Part I, New Delhi-110 048, India

Regd. D-(C)-540